



NATIONAL TECHNICAL UNIVERSITY OF ATHENS  
SCHOOL OF MECHANICAL ENGINEERING

***Konstantinos Chouzouris***

COMPARATIVE STUDY BETWEEN CONVENTIONAL METHODS  
AND ADDITIVE MANUFACTURING OF METALLIC SCAFFOLDS FOR  
RECONSTRUCTING AND HEALING DISTAL FEMUR BONE DEFECTS  
WITH MAJOR BONE LOSS

Department of Mechanical Design & Automatic Control  
Machine Elements Laboratory

Supervisor: Associate Professor Vasilios Spitas

Athens 2023



ΕΘΝΙΚΟ ΜΕΤΣΟΒΙΟ ΠΟΛΥΤΕΧΝΕΙΟ  
ΣΧΟΛΗ ΜΗΧΑΝΟΛΟΓΩΝ ΜΗΧΑΝΙΚΩΝ

*Κωνσταντίνος Χουζούρης*

ΣΥΓΚΡΙΤΙΚΗ ΜΕΛΕΤΗ ΜΕΤΑΞΥ ΣΥΜΒΑΤΙΚΩΝ ΜΕΘΟΔΩΝ ΚΑΙ  
ΠΡΟΣΘΕΤΙΚΗΣ ΚΑΤΑΣΚΕΥΗΣ ΜΕΤΑΛΛΙΚΩΝ ΙΚΡΙΩΜΑΤΩΝ ΓΙΑ ΤΗΝ  
ΑΝΑΠΛΑΣΗ ΚΑΙ ΕΠΟΥΛΩΣΗ ΚΑΤΑΓΜΑΤΩΝ ΣΤΟ ΠΕΡΙΦΕΡΙΚΟ  
ΤΜΗΜΑ ΤΟΥ ΜΗΡΙΑΙΟΥ ΟΣΤΟΥ ΜΕ ΜΕΙΖΟΝΑ ΟΣΤΙΚΗ ΑΠΩΛΕΙΑ

Τομέας Μηχανολογικών Κατασκευών και Αυτομάτου Ελέγχου  
Εργαστήριο Στοιχείων Μηχανών

Επιβλέπων: Αναπληρωτής Καθηγητής Βασίλειος Σπιτάς

Αθήνα 2023



## Acknowledgments

I would like to express my deepest gratitude to my supervisor, Associate Professor Vasilios Spitas. His guidance and support throughout this project have been invaluable. He provided me with the opportunity to work on a thesis topic that combines the fields of mechanical design and biomechanics, and his advice at every stage of the project has been instrumental to its success.

My thanks also go to my project coordinator, Christos Kalligeros. His eagerness to provide advice every day, answer my questions, and handle any problems that arose during the course of the project was greatly appreciated.

I am also deeply grateful to Dr. Athanasios Foukas. His crucial help, his input on the medical aspects of the project, and his constant counsel whenever needed were crucial to the completion of this thesis.

Lastly, I would like to thank my colleague, Panos Ntakos. His contribution and assistance were vital to the completion of the project. His support and collaboration made this project not only possible but also an enjoyable learning experience.

## Table of Contents

Acknowledgments.....	2
Table of Contents .....	3
Table of Figures .....	5
List of Tables.....	7
Abstract.....	9
Περίληψη .....	10
1. Introduction .....	11
2. Literature Review .....	13
2.1 Bone Defect.....	13
2.2 Bone Fracture Healing Process.....	16
2.3 Treatment of Distal Femur Fractures with Conventional Methods.....	17
2.4 3D Printed Bone Implants .....	22
2.5 Metallic Porous Scaffolds .....	24
2.6 Optimal Mechanical Environment for Osteogenesis in Bone Loss Defect .....	28
3. CAD Design and Finite Element Analysis of Bone Defect Repair .....	30
3.1 CT Scan to Bone CAD Model .....	30
3.2 Distal Femur Plates.....	34
3.3 Retrograde Intramedullary Nailing System .....	37
3.4 Porous Scaffold.....	39
3.5 Gait Analysis.....	41
3.6 Preparation and Boundary Conditions for Finite Element Analysis .....	43
3.6.1 Material Assignment .....	43
3.6.2 Contact Definition .....	47
3.6.3 Geometry Meshing .....	50
3.6.4 Simulation Analysis Settings.....	52
3.6.5 Application and Analysis of Forces and Supports .....	53
4. Exploring Non-Scaffold Approaches to Bone Defect Healing.....	55
4.1 Non-Scaffold Specifications.....	55
4.2 Initial Stage - Cartilage Bone .....	56
4.3 Later Stage – Immature Bone .....	60
4.4 An Alternative Approach.....	63
4.5 Non-Scaffold Fixating Techniques - Conclusion.....	65

5.	Design and Finite Element Analysis of Porous Scaffold Implant for Bone Defect Management .....	66
5.1	Unit Cell to Scaffold.....	66
5.2	Homogenization .....	73
5.2.1	ANSYS Homogenization.....	73
5.2.2	nTop Homogenization .....	75
5.3	Strain Analysis Based on Scaffold Design Variations .....	80
5.3.1	Single Plating Technique .....	80
5.3.2	Single Nailing Technique .....	86
5.3.3	Plate and Nail Technique.....	88
5.4	Testing Method on C3 Fractures .....	93
5.5	Post-Regeneration Simulations .....	95
5.6	Conclusions and Final Scaffold Design Selection .....	99
6.	Exploring Topology Optimization .....	104
6.1	Scaffold Design Optimization .....	105
7.	Conclusion.....	113
	List of References .....	115

## Table of Figures

Figure 2.1 Bone defect of the tibia [5] .....	13
Figure 2.2 Femur Bone and Parts [7] .....	14
Figure 2.3 Classification of Distal Femoral Fractures [8] .....	15
Figure 2.4 X-Ray of C3 Fracture with Bone Defect Loss [6] .....	16
Figure 2.5 Fracture Healing Process [9] .....	17
Figure 2.6 Stryker - AxSOS 3 Ti Distal Lateral Femur [11].....	18
Figure 2.7 Post Operation X-Ray of Distal Femur Locking Plate [4].....	18
Figure 2.8 Articulated Tension Device For Compression [10] .....	19
Figure 2.9 X-Ray of Retrograde Nailing Fixation.....	19
Figure 2.10 T2 Alpha Femur Retrograde Nailing System [11] .....	20
Figure 2.11 T2 Alpha Femur Antegrade Nailing System [11] .....	20
Figure 2.12 Combination of Nailing System and Locking Plate [12] .....	21
Figure 2.13 Post Operative Nail Plate Fixation [13].....	21
Figure 2.14 X-Ray Double Plating Approach [14] .....	22
Figure 2.15 3D Printed CT-Bone Implant.....	24
Figure 2.16 Metallic 3D Printed Implant on Distal Femur.....	25
Figure 2.17 Basic structural unit: p: aperture, t: pillar thickness [15].....	26
Figure 2.18 Diamond Unit Cell .....	26
Figure 2.19 Design Method of Voronoi Scaffold [17].....	27
Figure 2.20 Unit cell of TPMS-based scaffolds [18].....	27
Figure 2.21 Various Unit Cell Designs [16] .....	28
Figure 2.22 Essential Strain for Every Phase of Bone Formation [20].....	29
Figure 3.1 Slicer Interface .....	30
Figure 3.2 After Grayscale Threshold.....	31
Figure 3.3 Post Slicer Operation.....	31
Figure 3.4 Pre Meshmixer Process .....	32
Figure 3.5 Post Meshmixer Process .....	32
Figure 3.6 Spaceclaim: Bone Marrow .....	33
Figure 3.7 Solidworks: Compact Bone (green) – Marrow (blue).....	33
Figure 3.8 Compact and Spongy Bone .....	34
Figure 3.9 Assembly of Femur Bone with Spongy Bone .....	34
Figure 3.10 Main Distal Plate Final Design.....	35
Figure 3.11 Secondary Distal Plate.....	35
Figure 3.12 Single Plate Fixation Assembly .....	36
Figure 3.13 Double Plating Fixation Assembly .....	37
Figure 3.14 Double Plate Fixation Assembly – Inner Side.....	37
Figure 3.15 Retrograde Intramedullary Nailing System .....	38
Figure 3.16 Retrograde Nailing System Assembly - Section.....	38
Figure 3.17 Combination of Plate and Retrograde Nail Assembly-Section.....	39
Figure 3.18 Porous Scaffold Implant with Brackets.....	40
Figure 3.19 Porous Implant and Plate Assembly.....	40

Figure 3.20 Gait Cycle [21] .....	41
Figure 3.21 Anatomical Planes of Human Body [23].....	42
Figure 3.22 Forces Applied on Femur Bone [22].....	42
Figure 3.23 ANSYS Bonded Contact [27] .....	48
Figure 3.24 ANSYS Frictional Contact [27] .....	48
Figure 3.25 ANSYS Frictionless Contact [27] .....	49
Figure 3.26 Contact between models .....	50
Figure 3.27 ANSYS: Mesh Example.....	51
Figure 3.28 Scaffold, Screws and Plate Mesh.....	51
Figure 3.29 Forces Applied on Femur Head .....	54
Figure 3.30 Support and Forces on Femur Bone.....	54
Figure 4.1 Tissue Model in Defect Gap .....	56
Figure 4.2 Plate Cartilage - Full Load - Unrealistic Deformation .....	57
Figure 4.3 Double Plate Cartilage - Full Load - Realistic Deformation .....	58
Figure 4.4 Strains for Plate Cartilage - Full Load - Unrealistic Deformation.....	58
Figure 4.5 Strains for Double Plate Cartilage - Full Load - Realistic Deformation .....	59
Figure 4.6 Plate Immature - Full Load – Deformation.....	60
Figure 4.7 Double Plate Immature - Full Load – Deformation .....	61
Figure 4.8 Strains for Plate Immature - Full Load – Deformation .....	61
Figure 4.9 Strains for Double Plate Immature - Full Load – Deformation.....	62
Figure 4.10 Alternative Approach of Cartilage Bone .....	63
Figure 4.11 Cartilage Bone Strains – Swollen Model .....	64
Figure 4.12 Immature Bone Strains – Swollen Model.....	64
Figure 5.1 Honeycomb Unit Cell .....	67
Figure 5.2 Diamond Unit Cell .....	67
Figure 5.3 Voronoi Unit Cell .....	68
Figure 5.4 Voronoi Unit Cell - 0.9 mm Point Spacing .....	69
Figure 5.5 Voronoi Unit Cell – 1.2 mm Point Spacing .....	69
Figure 5.6 Honeycomb Final Scaffold.....	70
Figure 5.7 Diamond Scaffold - 0.35 .....	71
Figure 5.8 Diamond Scaffold - 0.25 .....	71
Figure 5.9 Voronoi Scaffold - 0.2 Thickness - 1 Point Spacing.....	72
Figure 5.10 Voronoi Scaffold - 0.15 Thickness – 1.2 Point Spacing .....	72
Figure 5.11 Material Designer Interface: Body and Material Assigning.....	74
Figure 5.12 Meshing the Unit Cell.....	74
Figure 5.13 Creating FE Mesh of Unit Cell .....	76
Figure 5.14 Diamond Unit Cell X-Axis Displacement.....	77
Figure 5.15 Directional Young's Modulus of Honeycomb Unit Cell .....	78
Figure 5.16 Directional Young's Modulus of Diamond Unit Cell .....	78
Figure 5.17 Directional Young's Modulus of Diamond Unit Cell .....	79
Figure 5.18 Plate Honeycomb - Strains Developed Upper Side .....	80
Figure 5.19 Plate Honeycomb - Strains Developed Lower Side .....	81
Figure 5.20 Plate Diamond 0.35 – Upper Side .....	82
Figure 5.21 Plate Diamond 0.35 - Lower Side .....	82



Figure 5.22 Plate Diamond 0.25 – Upper Side .....	83
Figure 5.23 Plate Diamond 0.25 - Lower Side .....	83
Figure 5.24 Plate Voronoi 0.2 – Upper Side .....	84
Figure 5.25 Plate Voronoi 0.2 – Lower Side .....	84
Figure 5.26 Plate Voronoi 0.15 – Upper Side .....	85
Figure 5.27 Plate Voronoi 0.15 – Lower Side .....	85
Figure 5.28 Nail Diamond 0.35 – Upper Side .....	86
Figure 5.29 Nail Diamond 0.35 – Lower Side .....	86
Figure 5.30 Nail Voronoi 0.2 – Upper Side .....	87
Figure 5.31 Nail Voronoi 0.2 – Lower Side .....	87
Figure 5.32 Plate&Nail Diamond 0.35 – Upper Side .....	88
Figure 5.33 Plate&Nail Diamond 0.35 – Lower Side .....	89
Figure 5.34 Plate&Nail Diamond 0.25 – Upper Side .....	90
Figure 5.35 Plate&Nail Diamond 0.25 – Lower Side .....	90
Figure 5.36 Plate&Nail Voronoi 0.2 – Upper Side .....	91
Figure 5.37 Plate&Nail Voronoi 0.2 – Lower Side .....	91
Figure 5.38 Plate&Nail Voronoi 0.15 – Upper Side .....	92
Figure 5.39 Plate&Nail Voronoi 0.15 – Lower Side .....	92
Figure 5.40 C3 Fracture Model – Plating Technique on Solidworks Interface.....	93
Figure 5.41 Regenerated Diamond Unit Cell.....	96
Figure 5.42 Deformation of Healthy Bone .....	97
Figure 5.43 Deformation of Healed Bone with Diamond Scaffold .....	97
Figure 5.44 Strains Developed on Healthy Bone.....	98
Figure 5.45 Strains Developed on Healed Bone with Diamond Scaffold .....	98
Figure 5.46 Voronoi Ideal Scaffold on nTop .....	101
Figure 5.47 Voronoi Ideal Scaffold - Upper Side .....	102
Figure 5.48 Voronoi Ideal Scaffold - Zoomed .....	102
Figure 6.1 Topology Optimization of Hip Implant [32].....	105
Figure 6.2 Forces Extraction Approach on Ansys .....	106
Figure 6.3 nTop: Setting Boundary Conditions.....	107
Figure 6.4 Scaffold Displacement.....	107
Figure 6.5 Diamond Initial Component.....	109
Figure 6.6 Voronoi Initial Component.....	109
Figure 6.7 nTop Interface: Optimal Voronoi Scaffold Result .....	110
Figure 6.8 nTop Interface: Optimal Voronoi Scaffold Result .....	111
Figure 6.9 nTop Optimization Imperfections.....	112

## List of Tables

Table 1 Forces of Gait Cycle on Femoral Head .....	43
Table 2 Material Properties of Various Bone Types [24] .....	44
Table 3 Material Properties of <b>Cortical Bone</b> .....	45
Table 4 Material Properties of <b>Spongy Bone</b> .....	45
Table 5 Material Properties of <b>Immature Bone</b> .....	45

Table 6 Material Properties of <b>Cancellous Bone</b> .....	46
Table 7 Material Properties of <b>Granulation Tissue</b> .....	46
Table 8 Material Assignment and References .....	47
Table 9 Meshing Method and Element Size for Every Model .....	52
Table 10 Simulation Analysis Settings .....	53
Table 11 Approaches without Porous Scaffold.....	55
Table 12 Table of Strains and Deformations for Initial Stage .....	59
Table 13 Table of Strains and Deformations for Later Stage .....	62
Table 14 Non-Scaffold Viable Fixating .....	65
Table 15 Final Unit Cells .....	68
Table 16 Final Homogenization Results.....	75
Table 17 ANSYS Interface: Anisotropic Elasticity Matrix of Diamond Unit Cell.....	79
Table 18 Table of Strains Developed .....	100
Table 19 Optimal Scaffold Choice for Every Fixating Technique.....	100
Table 20 Parametric Components Parameters.....	108

## Abstract

Bone defects pose a significant challenge for orthopedic surgeons, and the use of 3D printed scaffold implants represents a revolutionary and continuously evolving technique for their treatment. This study focuses on bone defects on the distal side of the femur and aims to identify the optimal approach for managing such defects, whether through conventional fixation methods or the use of 3D printed porous scaffolds. To this end, we constructed a finite element model of the fractured bone to determine the strains developed at the interface of the porous scaffold (or the cartilage bone if no scaffold is used) and the healthy bone. Based on a literature review and consultation with Dr. Anastasios Foukas, we considered a strain range of 2% - 8% as ideal for bone regeneration in the case of bone defects. With this assumption, we conducted simulations for various fixation methods, both with and without a scaffold. Our findings suggest that single plating or single nailing techniques are not viable without a scaffold implant. On the other hand, the double plating fixation approach is found to be fully recommended and could ensure the natural mobility of the patient. In terms of scaffold design, our results indicate that the best approach consists of a Voronoi scaffold design with increased structural compliance in order to develop the desired strain. This approach was found to be most effective in promoting bone regeneration. Towards the end, we briefly delve into the concept of topology optimization for optimal scaffold design, which holds significant potential for future research. This study thus provides valuable insights into the treatment of bone defects and paves the way for further advancements in the field of orthopedic surgery.

## Περίληψη

Τα τραύματα με οστική απώλεια αποτελούν σημαντική πρόκληση για τους ορθοπεδικούς χειρουργούς, και η χρήση μεταλλικών ικριωμάτων που έχουν κατασκευαστεί μέσω προσθετικής κατασκευής αντιπροσωπεύει μια επαναστατική και συνεχώς εξελισσόμενη τεχνική για τη θεραπεία τους. Αυτή η μελέτη επικεντρώνεται σε κάταγμα διαφύσεως στο περιφερικό τμήμα του μηριαίου οστού με οστική απώλεια και στοχεύει στον εντοπισμό της βέλτιστης προσέγγισης για τη διαχείριση τέτοιων ατελειών, είτε μέσω συμβατικών μεθόδων στήριξης είτε μέσω της χρήσης πορώδους ικριώματος. Για τον σκοπό αυτό, κατασκευάσαμε ένα μοντέλο πεπερασμένων στοιχείων του τραυματισμένου οστού για να εντοπίσουμε τις παραμορφώσεις που αναπτύσσονται στη διεπαφή του πορώδους σκελετού (ή του χόνδρινου οστού εάν δεν χρησιμοποιείται σκελετός) και του υγιούς οστού. Βασιζόμενοι στην βιβλιογραφία και με την συμβουλή του Δρ. Αναστάσιο Φούκα, θεωρήσαμε ότι ένα εύρος παραμορφώσεων 2% - 8% είναι ιδανικό για την αναγέννηση του οστού στην περίπτωση οστικής απώλειας. Με αυτήν την υπόθεση, διεξήγαμε προσομοιώσεις για διάφορες μεθόδους στήριξης, με ή χωρίς την χρήση του ικριώματος. Τα ευρήματά μας υποδεικνύουν ότι οι τεχνικές μονής πλάκας ή μονού ήλου δεν είναι βιώσιμες χωρίς την χρήση ικριώματος. Από την άλλη πλευρά, η προσέγγιση στήριξης με διπλή πλάκα συνίσταται πλήρως και θα μπορούσε να διασφαλίσει τη φυσική κινητικότητα του ασθενούς. Όσον αφορά τον σχεδιασμό του ικριώματος, τα αποτελέσματά μας υποδεικνύουν ότι η καλύτερη προσέγγιση αποτελεί τον σχεδιασμό σκελετού Voronoi με αυξημένη ενδοτικότητα για να επιτευχθούν οι επιθυμητές παραμορφώσεις, άρα και η αναγέννηση του οστού. Προς το τέλος, εισάγουμε σύντομα την έννοια της τοπολογικής βελτιστοποίησης για τον βέλτιστο σχεδιασμό του ικριώματος, η οποία ενέχει σημαντικές προοπτικές για μελλοντική έρευνα. Συνοψίζοντας, αυτή η μελέτη παρέχει πολύτιμες πληροφορίες για τη θεραπεία των οστικών απωλειών και ανοίγει δρόμο για περαιτέρω πρόοδο στον τομέα της ορθοπεδικής χειρουργικής.

## 1. Introduction

Bone defects, particularly those occurring in the distal femur, pose a significant challenge in the field of orthopedics. These defects, which can result from trauma, disease, or surgical intervention, often lead to a loss of bone that is not easily replaced or regenerated. The body's natural healing processes may be insufficient to fully restore the structural integrity and function of the affected bone, leading to long-term complications such as instability, pain, and reduced mobility. Furthermore, the complexity of the bone's structure, its load-bearing role, and the need for precise alignment and fit with surrounding tissues make the treatment of bone defects particularly challenging. The development of effective treatment strategies for bone defects is therefore a critical area of research in orthopedic surgery.

There are two primary strategies for addressing bone defects. The first involves the use of conventional fixation methods, such as plates and nails, which rely on the body's natural wound healing process to regenerate bone. These methods aim to stabilize the fracture, align the bone fragments, and create the optimal conditions for the body to heal itself. However, in cases of significant bone loss, this approach may not be sufficient. This has led to the development of a second strategy, which involves the use of 3D printed metallic scaffolds. These scaffolds are implanted into the bone defect and, in combination with conventional fixation techniques, provide a structure that promotes bone regeneration. The scaffold serves as a temporary framework that supports new bone growth, ultimately leading to the restoration of the bone's structure and function. This innovative approach represents a significant advancement in the treatment of bone defects.

The regeneration of bone in a defect area is a complex process that requires specific mechanical conditions to be met, particularly in terms of strain. Strain, or the deformation of a material in response to stress, plays a critical role in bone healing. In the case of a bone defect, the required strains are significantly higher than those needed for the healing of a simple bone fracture. This suggests that the patient's mobility and ability to walk, which can generate the necessary strain, are crucial for successful bone healing. However, this also introduces additional considerations when selecting the ideal fixation technique. The chosen method must not only stabilize the bone and support the scaffold, but also allow for the appropriate level of mobility to stimulate bone regeneration. Balancing these requirements presents a significant challenge in the treatment of bone defects.

The primary objective of this study is to identify the most effective fixation method and the optimal scaffold design for treating bone defects. To achieve this, we will conduct simulations using ANSYS Software, a powerful tool for engineering simulation. These simulations will test various fixation approaches, both with and without the use of a scaffold implant. This process will provide valuable insights into the most effective methods for stabilizing a bone defect, taking into account factors such as the patient's mobility, the strain required for bone regeneration, and the practicality of the fixation method in a clinical setting.

In terms of scaffold design, we will examine a variety of unit cells and their structures to determine the most effective porous structure for bone regeneration. Porous scaffolds play a crucial role in bone healing, providing a framework for new bone to grow and facilitating the delivery of nutrients. However,

modeling these porous structures in simulations presents a significant challenge due to their complex geometry and the need to accurately represent their mechanical properties. To overcome this, we will use a process known as homogenization, which simplifies the representation of the scaffold while preserving its overall mechanical behavior. This process, along with the criteria for selecting the optimal scaffold design, will be discussed in more detail in the following sections.

Lastly, this study will also delve into the concept of topology optimization as a potential tool for designing the ideal porous scaffold for bone regeneration, which would help to determine the optimal distribution of material within the scaffold to achieve the ideal strain for bone regeneration. This approach has the potential to revolutionize the design of porous scaffolds, allowing for the creation of structures that are not only mechanically optimal, but also tailored to the specific needs of the patient. Despite being in its early stages of application in this field, topology optimization holds significant promise for the future of bone defect treatment.

## 2. Literature Review

### 2.1 Bone Defect

A bone defect is a type of damage or discontinuity in the normal structure of a bone. This can occur as a result of various conditions such as trauma, infection, tumor growth, or certain diseases that cause bone loss like osteoporosis. Bone defects can vary in size and location, and they can significantly impact the structural integrity and function of the bone. Depending on the size and location of the defect, it may impair the affected individual's ability to move or bear weight, causing pain and reducing quality of life. The body has a natural ability to repair bone defects, but this process may not be sufficient for larger defects or in individuals with compromised health. As such, bone defects often require medical intervention to promote healing and restore function [1].

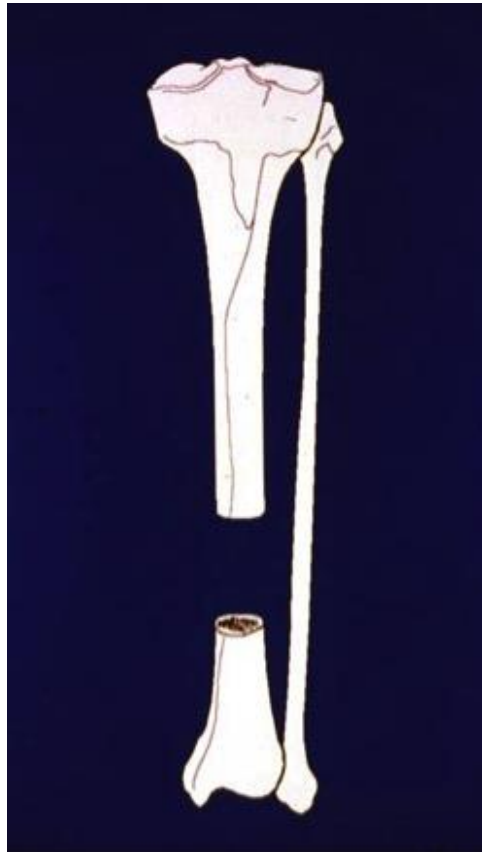


Figure 2.1 Bone defect of the tibia [5]

The femur, also known as the thigh bone, is the longest and strongest bone in the human body. It is located in the upper leg and extends from the hip to the knee. The femur is divided into three main parts:

1. **Proximal End:** This is the uppermost part of the femur, closest to the hip. It consists of the head, neck, and the greater and lesser trochanters. The head of the femur articulates with the acetabulum of the pelvis to form the hip joint. The neck connects the head with the shaft of the femur. The greater and lesser trochanters are prominent bony protrusions where several powerful muscles of the hip attach.
2. **Shaft:** This is the long, straight section of the femur. It is cylindrical in shape and slightly curved, being convex anteriorly and concave posteriorly. The shaft is surrounded by a thick layer of compact bone, which provides strength and rigidity, and a central medullary cavity, which contains bone marrow.
3. **Distal End:** This is the lower end of the femur, closest to the knee. It is wider than the shaft and ends in two large, rounded processes known as the medial and lateral condyles. These condyles articulate with the tibia in the lower leg to form the knee joint. Between the condyles on the anterior side is the patellar surface, where the patella, or kneecap, articulates with the femur.



*Figure 2.2 Femur Bone and Parts [7]*



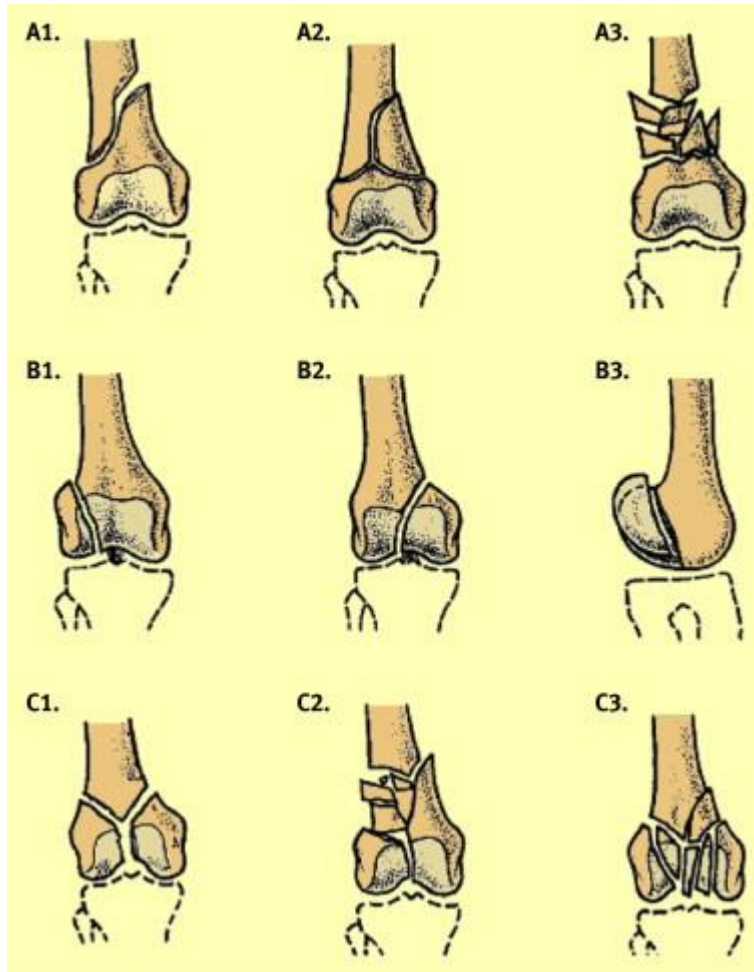


Figure 2.3 Classification of Distal Femoral Fractures [8]

A bone defect, particularly in the distal femur, is a significant medical challenge. This type of defect can lead to substantial functional impairment and reduced quality of life for the affected individuals. The distal femur, the lower part of the thigh bone that connects to the knee, is a critical area for weight-bearing and movement. Defects in this area can significantly impact a person's ability to walk or even stand. The healing of these defects is often complicated due to the complex anatomy of the area, the weight-bearing nature of the femur, and the proximity to the knee joint, which is one of the most complex joints in the human body.

In addition to the physical challenges, there are also biological challenges in healing bone defects. The body's natural bone healing process may not be sufficient to fill large bone defects. This is because the body's ability to regenerate bone decreases with the size of the defect. Furthermore, the healing process can be affected by various factors such as age, nutritional status, and the presence of other diseases or conditions [1].

The treatment of distal femur bone defects often requires a multidisciplinary approach involving orthopedic surgeons, physical therapists, and sometimes oncologists or infectious disease specialists,

depending on the cause of the defect. The goal of treatment is not only to fill the bone defect but also to restore function and prevent complications such as infection, non-union (failure of the bone to heal), and deformity.



Figure 2.4 X-Ray of C3 Fracture with Bone Defect Loss [6]

## 2.2 Bone Fracture Healing Process

The process of bone healing involves several stages, each with its unique characteristics and timeframes [2]. Here is a summary of these stages:

1. **Hematoma Formation:** This is the first stage of bone healing. After a fracture, blood vessels in the bone and surrounding tissue are damaged, leading to bleeding. This blood starts to clot, forming a hematoma around the fracture site. This hematoma provides the initial structural stability and cellular environment for healing to begin.
2. **Granulation Tissue Formation:** In this stage, new blood vessels start to form, and cells such as fibroblasts and osteoblasts begin to proliferate in the hematoma, converting it into granulation tissue. This tissue is soft and rich in collagen and blood vessels, providing a good environment for new bone formation.
3. **Soft Callus Formation:** The granulation tissue is gradually replaced by a callus, which is a bridge of new bone that connects the broken ends of the bone. This callus is initially soft (made of cartilage and fibrous tissue) but later becomes hard as more new bone is formed. (2-3 weeks)

4. **Hard Callus Formation:** During this stage, the callus continues to mature and solidify. The new bone starts to look and behave more like regular bone.
5. **Remodeling:** This is the final stage of bone healing. The new bone is remodeled to resemble the original bone structure more closely. This involves reshaping the bone and replacing the new bone with mature lamellar bone. This stage can take several years to complete.

Each of these stages is crucial for successful bone healing, and any disruption can lead to complications such as non-union or malunion of the fracture.

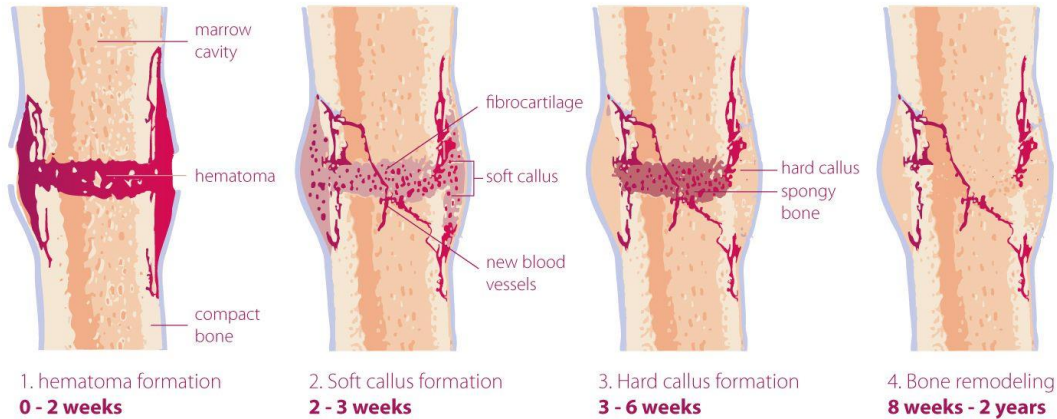


Figure 2.5 Fracture Healing Process [9]

### 2.3 Treatment of Distal Femur Fractures with Conventional Methods

A distal femur fracture is a break in the thigh bone just above the knee, which can extend into the knee joint itself or occur around total joint replacements. These fractures are usually the result of high-energy injuries in younger patients or falls in elderly patients. The distal femur forms the top half of the knee joint and the groove that the kneecap travels in, making it crucial for knee strength and stability.

Non-surgical treatment for distal femur fractures is rare, as the strength of the muscles that pull on the bones often necessitates surgery for the bone to heal. However, non-operative care may be recommended for adults with poor overall health, fragile or chronically infected skin, and less active patients. This treatment involves knee immobilizers, hinged knee braces, and casts, and requires regular follow-up care to ensure the fracture stays in good position and heals appropriately.

Surgical treatment is often recommended if the fracture pieces are displaced, if the bone sticks out of the skin, if the skin is at risk for dying, or if the bone is unstable due to the fracture type. The distal femur can be fixed with **metal plates and screws** or **intramedullary nails**. In severe cases, external fixation may be required prior to definitive surgical treatment. After surgery, patients are often placed in a knee immobilizer or hinged brace and cannot bear weight immediately [4].

**Distal femur plates** are designed with a locking mechanism that provides a secure and stable fit. The upper side of these plates bears a resemblance to a typical locking plate, characterized by its flat and

elongated structure. However, the lower part of the plate is uniquely designed with a specific geometry. This special design is not arbitrary but is meticulously crafted to accommodate the complex structure of the condylar part of the femur. The tailored fit ensures that the plate aligns accurately with the bone, providing optimal support and stability during the healing process. Furthermore, these plates are designed to work in conjunction with an articulated tension device, which allows for pretension to be applied to the plate, enhancing its stability and ensuring a more secure fit.



*Figure 2.6 Stryker - AxSOS 3 Ti Distal Lateral Femur [11]*



*Figure 2.7 Post Operation X-Ray of Distal Femur Locking Plate [4]*

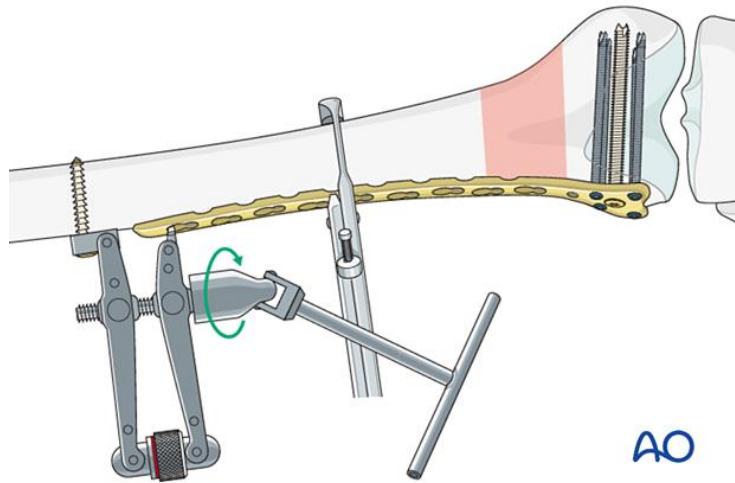


Figure 2.8 Articulated Tension Device For Compression [10]

Two primary methods of **intramedullary nailing** are commonly employed: antegrade and retrograde nailing. **Antegrade** femoral nailing, often considered the gold standard in the treatment of diaphyseal femur fractures, involves the insertion of the nail into the marrow cavity of the femur from the hip end. This method boasts a high union rate and is associated with decreased pulmonary complications, thromboembolic events, improved rehabilitation, and a reduction in the length of stay and cost of hospitalization. On the other hand, **retrograde** femoral nailing is performed by inserting the nail from the knee end. This method is typically indicated for certain conditions such as ipsilateral femoral neck fracture, floating knee (ipsilateral tibial shaft fracture), ipsilateral acetabular fracture, multiple system trauma, bilateral femur fractures, morbid obesity, and pregnancy. The results of retrograde nailing are comparable to those of antegrade nailing, offering a viable alternative when the latter is not suitable. Despite their differences in approach, both methods aim to provide stable fixation, promote fracture healing, and restore function.



Figure 2.9 X-Ray of Retrograde Nailing Fixation [33]



Figure 2.10 T2 Alpha Femur Retrograde Nailing System [11]



Figure 2.11 T2 Alpha Femur Antegrade Nailing System [11]

Having discussed the distinct characteristics and applications of both the distal femur plate and the nailing system, it is important to note that these methods are not mutually exclusive. In fact, in certain complex cases, a **combination** of these techniques may be employed to optimize the healing process and ensure the stability of the fracture site. For instance, the nailing system can be used in conjunction with a plate to provide enhanced support and alignment. This combined approach leverages the strength and stability of the nail, along with the precise fit and secure fixation of the plate. Similarly, the use of two plates together is another viable strategy, particularly for fractures that involve multiple fragments or require additional support. This approach allows for a more comprehensive coverage of the fracture site, ensuring a more robust and secure fixation.



*Figure 2.12 Combination of Nailing System and Locking Plate [12]*



*Figure 2.13 Post Operative Nail Plate Fixation [13]*

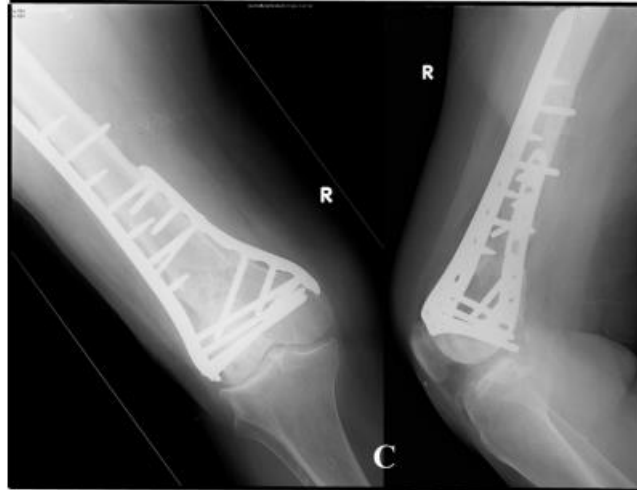


Figure 2.14 X-Ray Double Plating Approach [14]

## 2.4 3D Printed Bone Implants

Human bones have the ability to self-repair and regenerate, but this ability is limited. When bone damage exceeds its self-healing capacity, artificial repair is required. Traditional bone repair methods have limitations, such as the limited amount of transplantable bones at the donor site of patients and possible complications at the donor site after transplantation. To overcome these limitations, researchers have started to study the possibility of replacing human bones with grafts.

Three-dimensional (3D) printing technology plays a significant role in the biomedical field due to its unique advantages. It allows for the preparation of different organs and tissue structures, which can solve the problem of insufficient organ donors to a large extent. In particular, for applications in bones and bone scaffolds, 3D printing offers a solution for the treatment of patients with complex bone defects.

There are various materials used for 3d printing of bone scaffolds and they are presented below, based on information extracted from the paper by Zhaolong Li , Qinghai Wang and Guangdong Liu [3]:

1. **Inorganic Biomaterials:** These include metals and bio-ceramics, which are widely used to repair and regenerate diseased and damaged bones. They are particularly useful for bone transplantation and bone cement, orthopedic load-bearing coatings, and periodontal repair.
  - ***Non-Degradable Metal Material:*** Titanium and its alloys are widely used due to their low elastic modulus, low density, good corrosion resistance, and good biocompatibility. However, the elastic modulus of pure titanium is still higher than that of bone, which can lead to stress shielding effect. To overcome this, researchers have developed porous structures using titanium alloys, which can be adjusted to have an elastic modulus closer



to that of bone. Tantalum, known as the "biophilic metal", has excellent biological inertia and biocompatibility and has shown good clinical osteogenic activity, osteo induction, and osteo conductivity.

- *Degradable Metal Material:* These metals can be gradually degraded by body fluid corrosion in the body, and the released corrosion products can bring about an appropriate host reaction in the body. After assisting the body to complete the mission of tissue repair, they will all be absorbed or excreted by the body. The research on degradable metals is mainly focused on three types of metal materials with iron, magnesium, and zinc as the matrix. Iron-manganese alloy, for example, has shown similar tensile mechanical properties and good biocompatibility with natural bone.
- *Bioceramics:* Bioceramics rich in calcium and phosphorus salts, chemically and heat-treated metals such as titanium and tantalum, have certain osteo-inductive ability. For example, a composite scaffold containing magnetic ferro ferric oxide nanoparticles and bioactive glass/polycaprolactone has been prepared, which promotes osteoblast osteogenesis while achieving continuous drug delivery. The combination of bio-ceramic and organic material can improve osteogenic capability. All these have indicated that the use of **composite materials** is an important direction for the future development of bone implants.

## 2. Synthetic Polymer Materials:

- *Degradable Synthetic Polymer Materials:* These include polylactic acid (PLA), polycaprolactone (PCL), and polylactic acid-glycolic acid copolymer (PLGA). These materials are environmentally friendly and can be obtained by extracting materials from renewable resources in nature through polymerization. These materials have good biocompatibility and mechanical properties. However, a single material always has some defects, such as low surface osteogenic property and high brittleness, which can be overcome after being compounded with some materials to prepare bone implants.
- *Nondegradable Synthetic Polymer Materials:* These include poly-ether-ether-ketone (PEEK) and polyamide (PA). These materials have good biocompatibility and an elastic modulus comparable to that of the human cortical bone, which can reduce the stress shielding after implantation in the human body. They are widely used as bone graft materials. The disadvantages of PEEK are that it is not biologically active and its surface osteogenic efficiency is low. The combination with other materials can solve these problems.
- *Natural Polymer Material:* These include materials such as sodium alginate, collagen, and chitosan (CTS) that can be directly extracted from natural organisms. These materials possess good bio adhesion, biocompatibility, and excellent

biodegradability. However, they have certain defects in mechanical properties, which can be improved by compounding with other materials.

1. *Gelatin (GEL)*: A GEL/SA gel scaffold has been prepared using a three-dimensional biological printer, which had good biocompatibility and promoted the proliferation of human dental pulp cells and could be used as a dental regeneration scaffold.
2. *Silk Fibroin (SF)*: A composite scaffold made of SF and type II collagen (COL II) has been prepared, which meets the relevant requirements of cartilage tissue engineering.



*Figure 2.15 3D Printed CT-Bone Implant*

## 2.5 Metallic Porous Scaffolds

Metallic porous scaffolds are a significant area of research in the field of bone tissue engineering due to their potential to mimic the structure of natural bone. These scaffolds are characterized by their unique geometric properties, including unit cell structure, porosity, and thickness, which play a crucial role in their functionality. The unit cell, the smallest repeating unit in a scaffold, defines the overall architecture and mechanical properties of the scaffold. The porosity, or the void space within the scaffold, is another critical parameter as it facilitates cell migration, nutrient diffusion, and vascularization, which are essential for bone regeneration. The thickness of the scaffold, on the other hand, can influence the mechanical strength and degradation rate of the scaffold. The design and optimization of these parameters are vital to ensure the success of metallic porous scaffolds as bone implants. The most common materials used for these scaffolds include **titanium and its alloys** due to their excellent mechanical properties and biocompatibility. Recent advancements in manufacturing techniques, such as additive manufacturing, have allowed for the production of scaffolds with complex geometries and controlled porosity, paving the way for more effective bone implants.



Figure 2.16 Metallic 3D Printed Implant on Distal Femur

**Porosity** is a critical parameter in the design of bone scaffolds, as it directly influences the scaffold's mechanical properties, degradation rate, and biological performance. In the context of bone scaffolds, porosity refers to the presence of interconnected void spaces within the scaffold material. These spaces provide room for bone tissue ingrowth, vascularization, and nutrient diffusion, which are essential for successful bone regeneration.

The level of porosity and the size of the pores within a scaffold need to be carefully controlled. High porosity can promote cell migration and nutrient diffusion, but it may also compromise the mechanical strength of the scaffold. On the other hand, low porosity can enhance the scaffold's mechanical strength but may limit cell migration and nutrient diffusion, thereby hindering bone regeneration.

Typically, a balance must be struck between these factors, and the optimal porosity often depends on the specific application. For instance, scaffolds used for load-bearing applications may require lower porosity to ensure sufficient mechanical strength, while those used for non-load-bearing applications may benefit from higher porosity to promote tissue ingrowth and regeneration. The pore size also plays a role, with research suggesting that pore sizes between 100 and 500 micrometers are beneficial for bone ingrowth [15].

$$\text{Porosity} = (V_p/V_s) \times 100\%$$

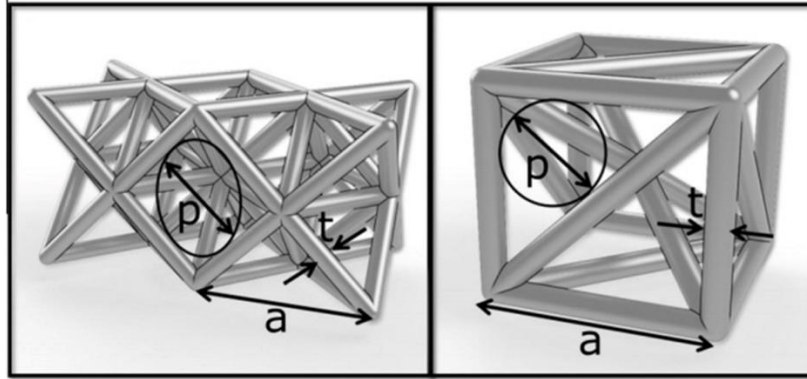


Figure 2.17 Basic structural unit:  $p$ : aperture,  $t$ : pillar thickness [15]

There are several types of **unit cells** commonly used in the design of porous scaffolds. These include body-centered cubic (BCC), modified BCC unit, pillar BCC, diamond, Voronoi, and triply periodic minimal surface (TPMS) units.

The BCC unit cell is a simple cubic lattice structure with an additional atom located at the center of the cube. The modified BCC unit cell and pillar BCC unit cell are variations of the BCC structure, designed to enhance the mechanical properties of the scaffold. The diamond unit cell, on the other hand, is characterized by a repeating pattern of eight atoms that form the shape of two interpenetrating tetrahedra.

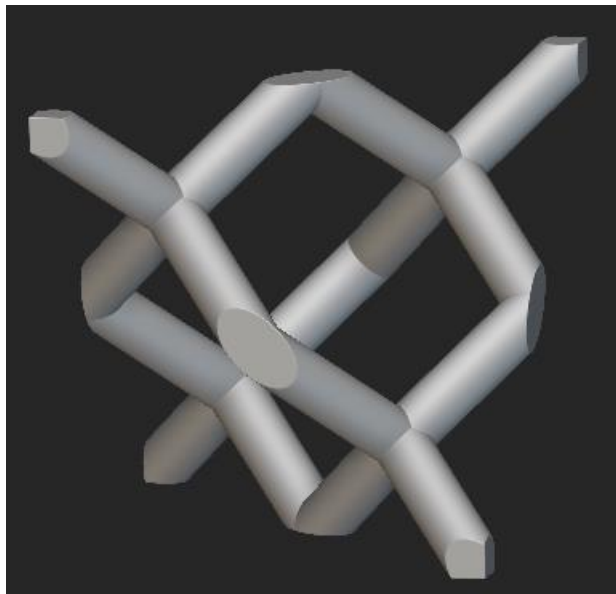


Figure 2.18 Diamond Unit Cell

A Voronoi unit cell is created by a process that involves the division of a space into a number of regions. Each region is defined by a seed point, and the boundaries of the region are determined by the points

that are closest to the seed point. The process begins by selecting a set of seed points in the space. Then, for each point in the space, the algorithm determines which seed point is closest. The space is then divided into regions, where each region contains all the points that are closest to a particular seed point. This results in a tessellation of the space, where each region is a Voronoi cell. The collection of all Voronoi cells forms the Voronoi diagram. In the context of materials science, the Voronoi unit cell is often used to represent the atomic structure of a material, with each Voronoi cell representing the space around an atom.

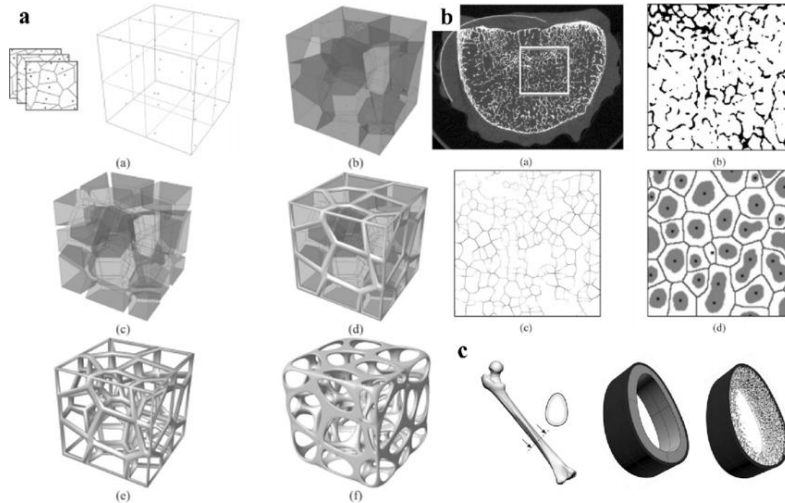


Figure 2.19 Design Method of Voronoi Scaffold [17]

Lastly, TPMS unit cells are based on minimal surfaces that repeat in three dimensions. These unit cells are often used in the design of scaffolds due to their unique combination of topological, mechanical, and mass transport properties.

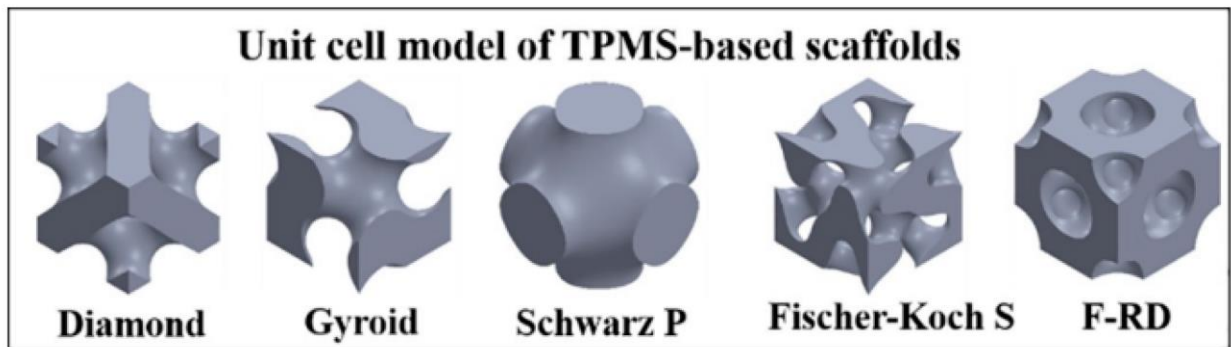


Figure 2.20 Unit cell of TPMS-based scaffolds [18]

Each of these unit cell types offers distinct advantages and can be selected based on the specific requirements of the scaffold, such as its mechanical properties, porosity, and the desired rate of bone ingrowth [16].

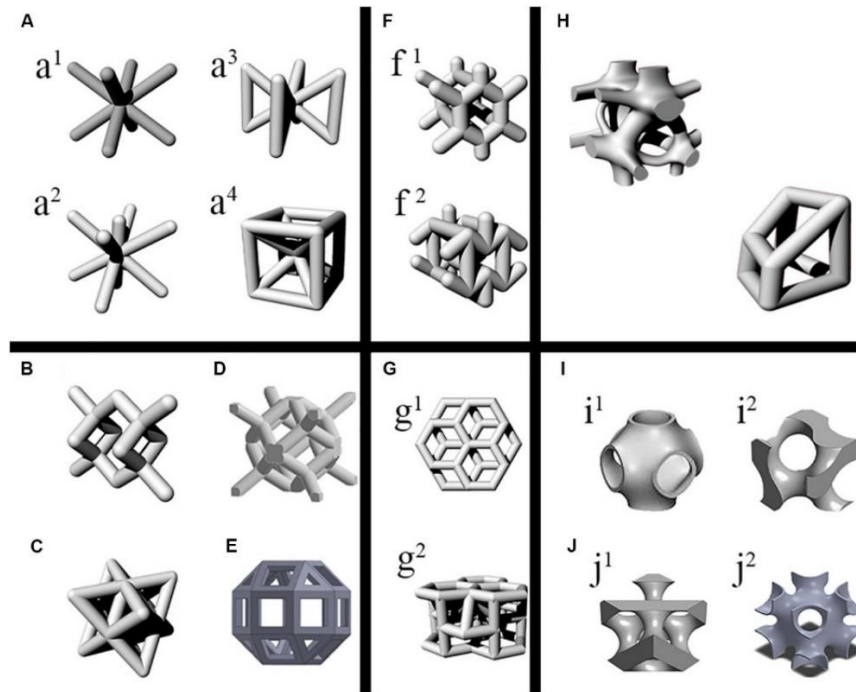


Figure 2.21 Various Unit Cell Designs [16]

## 2.6 Optimal Mechanical Environment for Osteogenesis in Bone Loss Defect

Strain is a fundamental concept in biomechanics that refers to the degree of deformation experienced by a material or tissue in response to an applied force. It is a dimensionless quantity, typically expressed as a percentage, that measures the relative change in shape or size of an object. In the context of biological tissues, such as those involved in bone repair, strain represents the change in shape or size of the cells or tissues due to mechanical stresses. For instance, when a force is applied to a bone, the bone material deforms - it changes shape and size - and this deformation is quantified as strain. Strain is calculated as the change in length (or deformation) divided by the original length. It is a crucial parameter in understanding how tissues respond to mechanical forces, and it plays a key role in processes such as bone remodeling and fracture healing. High levels of strain can lead to tissue damage or failure, while appropriate levels of strain can stimulate tissue growth and repair.

Achieving the ideal strain is a critical aspect of fracture healing. The concept of strain is central to understanding the biomechanics of fracture healing and improving treatment. Strain depends on mobility and, more importantly, the width of the fracture gap. The wider the gap, the less tissue deformation and vice versa. The treatment for a biologically active non-union that does not produce callus, which is characterized by a large gap and low strain without biomechanical induction, involves the application of axial compression. This results in the approximation and decrease of gap width, thereby

increasing strain and enabling induction. This understanding of strain is crucial in the clinical application of fracture healing, as it allows surgeons to adjust procedures to keep strain within the required bandwidth. The greater the expected mobility, the larger the required gap. Adjusting the gap size allows the installation of proper strain, which is a demanding option and gap width should only be varied within a small range. Therefore, achieving the ideal strain is a balance between mobility and gap width, and requires careful consideration and adjustment by the surgeon [19].

The ideal amount of strain required is not universally defined and can vary significantly depending on the specific circumstances. Literature reviews suggest that the strain for bone regeneration in a simple fracture typically ranges from 0.01% to 0.2%. However, the scenario changes when dealing with bone defects. In these cases, where the gap is filled with granulation tissue, the required strain is significantly higher. After extensive research and consultation with Dr. Athanasios Foukas Consultant Orthopedic Surgeon from KAT Attica General Hospital, it was determined that the desired strain for effective bone regeneration in the presence of a bone defect lies between 2% and 8%. This increased strain is necessary to stimulate the filling of the gap and promote bone regeneration [20].

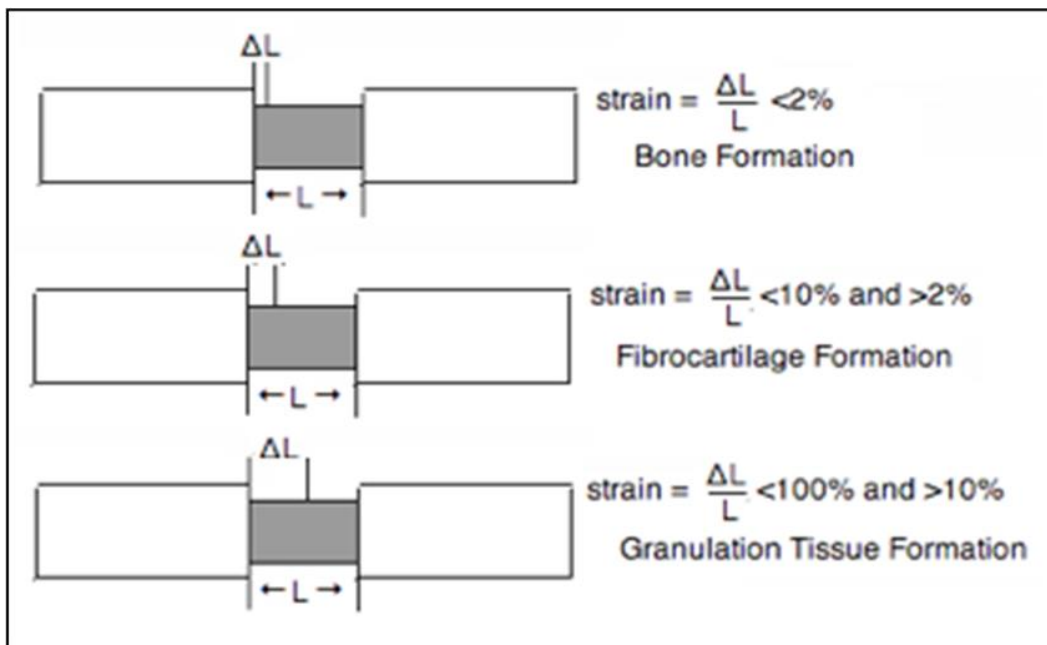


Figure 2.22 Essential Strain for Every Phase of Bone Formation [20]

### 3. CAD Design and Finite Element Analysis of Bone Defect Repair

#### 3.1 CT Scan to Bone CAD Model

The first chapter of designing the problem deals with the creation of the femur bone as a CAD model. This model was derived from CT scans using the software known as Slicer. Slicer is a software that facilitates the transformation of medical imaging data into 3D models, offering a comprehensive and precise depiction of the bone architecture. Furthermore, post-processing was executed using Meshmixer and SpaceClaim.

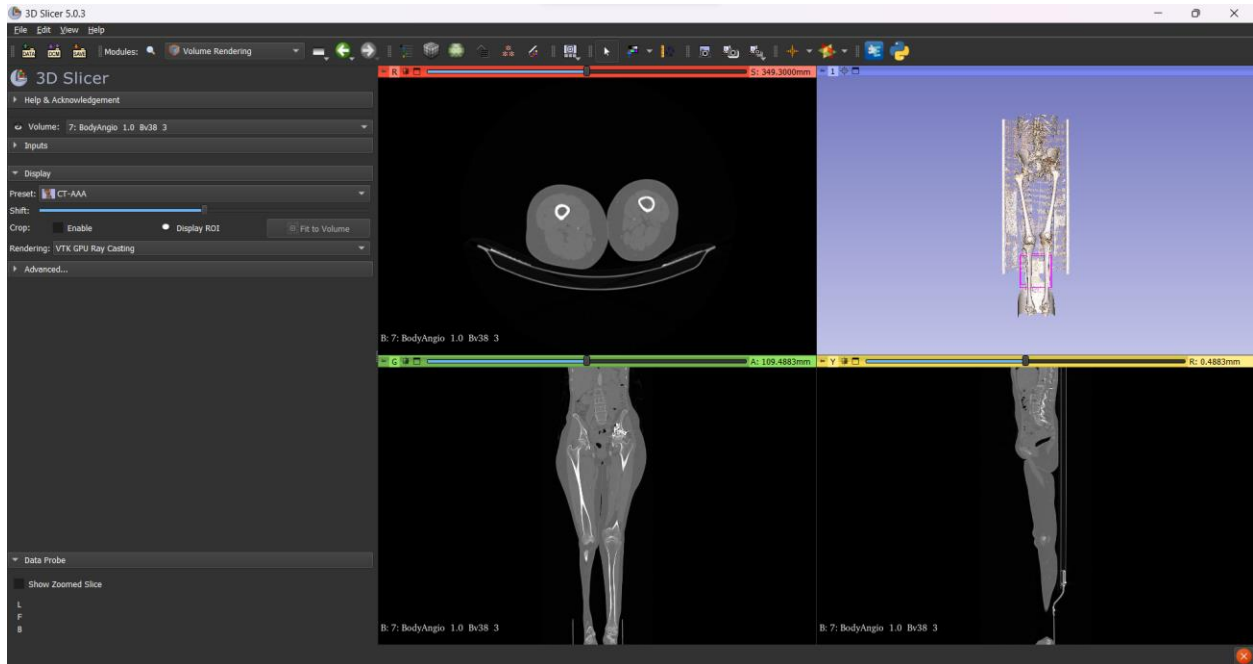


Figure 3.1 Slicer Interface

The transformation of a CT scan into a CAD model of a bone is a multi-step process. The focus is specifically concentrated on the left femur by minimizing the volume of the CT scan data. This step discards irrelevant parts of the body, allowing for a more focused analysis on the area of interest. Following this, a threshold filter is utilized to differentiate the compact bone from the surrounding tissues. This is made possible by the grayscale representation of the CT scan, where the compact bone appears white, enabling easier separation from other tissues. The selection of the threshold crucial to filter out as much of the non-target tissues as possible, while retaining valuable information of the femur. Despite the application of the threshold filter, some non-target tissues remain within the volume due to their grayscale values closely resembling that of the compact bone. To address this, tools such as the 'Island' and 'Cut' tools are employed to further isolate the compact bone of the femur, ensuring that the analysis is focused on the most relevant data.



In the final phase, the issue of numerous gaps present in the bone model, particularly in the distal region, is addressed. These gaps are a byproduct of the tools used earlier to isolate the femoral bone. To rectify this and achieve a solid, continuous model, the 'Paint' tool is employed. The 'Paint' tool is used to fill in the missing parts of the bone, referencing the outline geometry from the transverse plane as a guide. This slice-by-slice approach results in a compact and continuous model of the femoral bone.

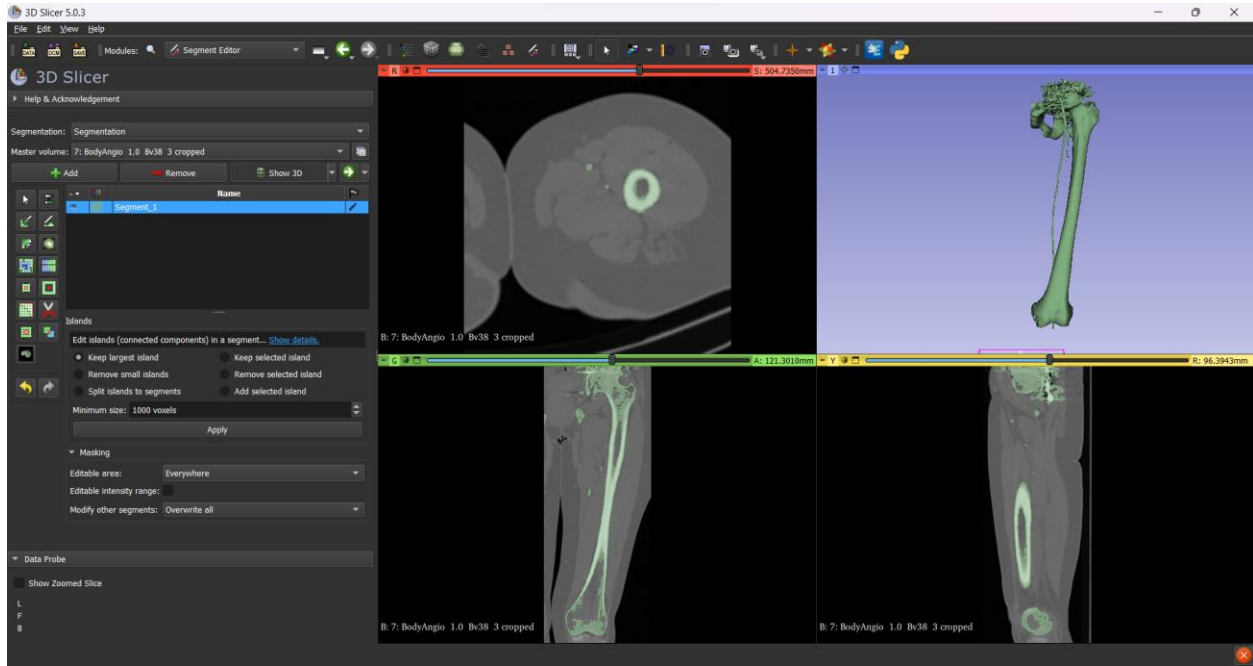


Figure 3.2 After Grayscale Threshold

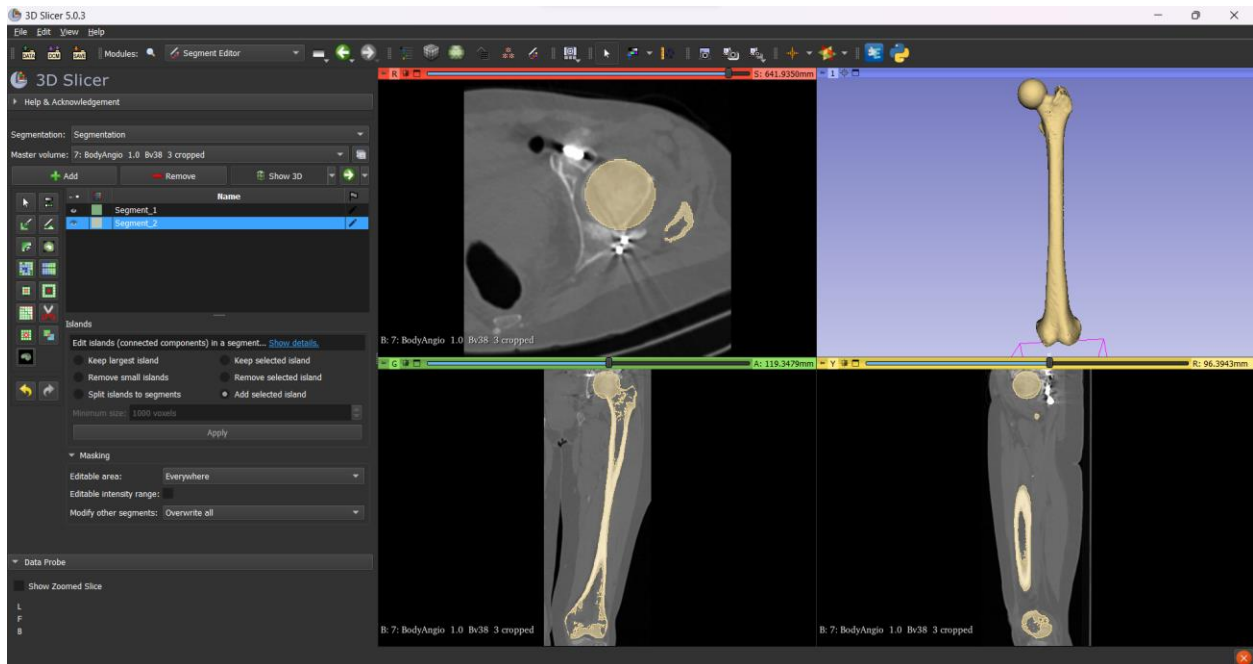


Figure 3.3 Post Slicer Operation

Subsequently, we tackle the geometric inconsistencies of the previous stage. To correct these geometric anomalies, we export the bone model in .stl format and import it into the Meshmixer software. Within Meshmixer, we use the 'BubbleSmooth', which is specifically designed to refine the surfaces of 3D models, with focus on the distal femur area.

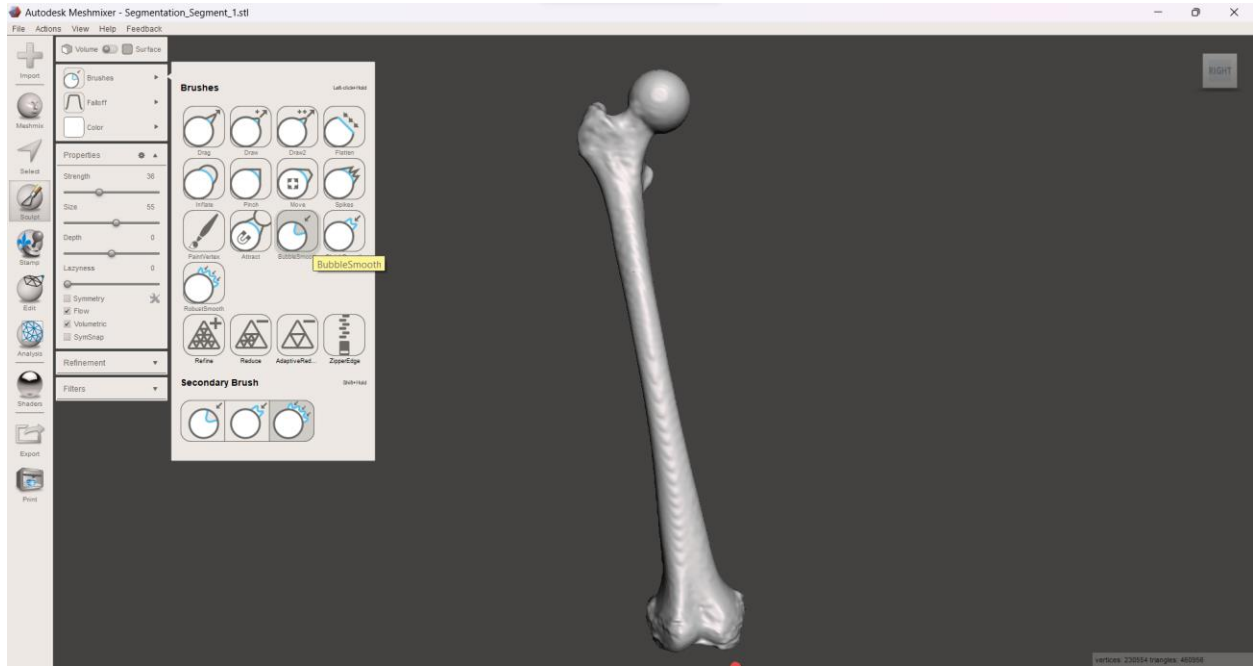


Figure 3.4 Pre Meshmixer Process



Figure 3.5 Post Meshmixer Process

The last objective is to distinguish the actual bone from the bone marrow. To accomplish this, we employ the use of SpaceClaim software. Upon importing the .stl file, we segregate the surfaces to create two distinct models using the 'Skin Surface' feature and generate the solid bodies using 'Auto Skin'. Lastly, we utilize Solidworks software to align the two bodies in an assembly and subtract the inner volume using the 'Cavity' feature. This process results in our final desired model of the femoral bone.

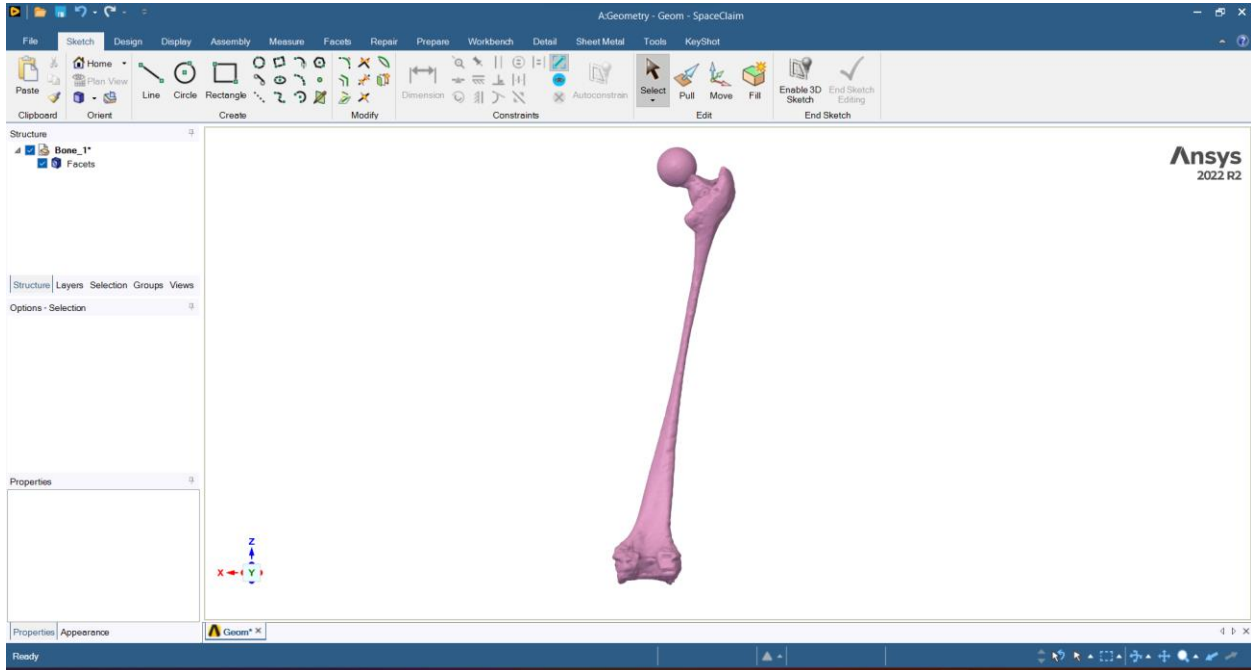


Figure 3.6 Spaceclaim: Bone Marrow

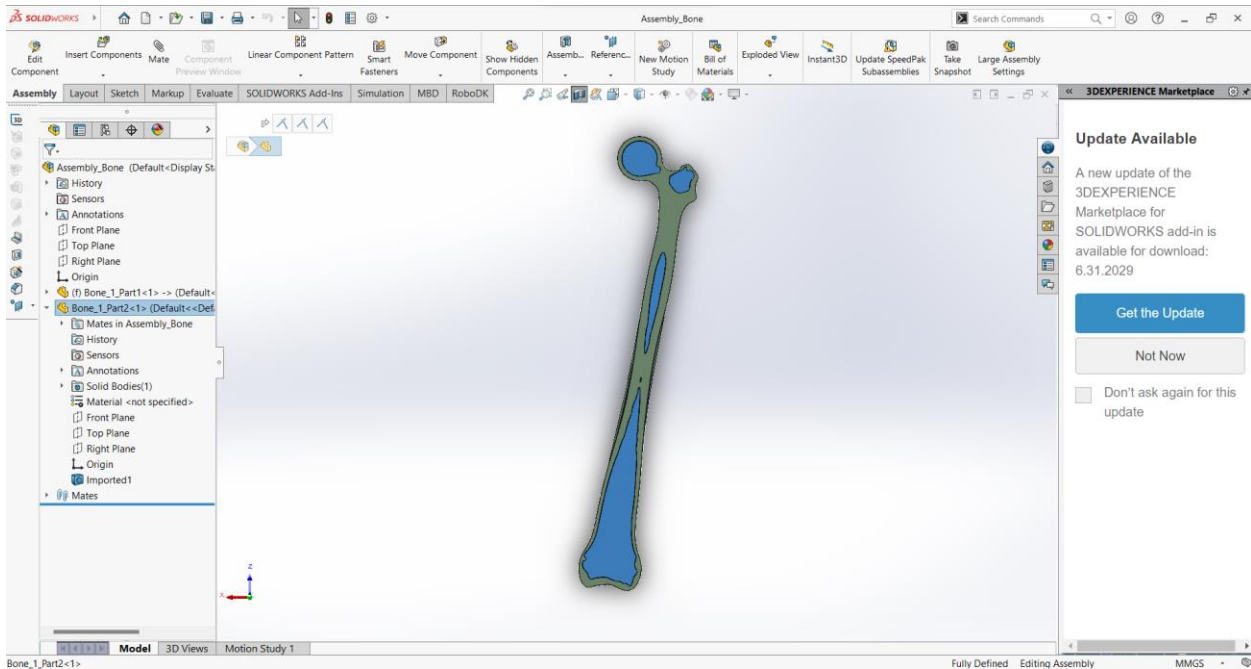
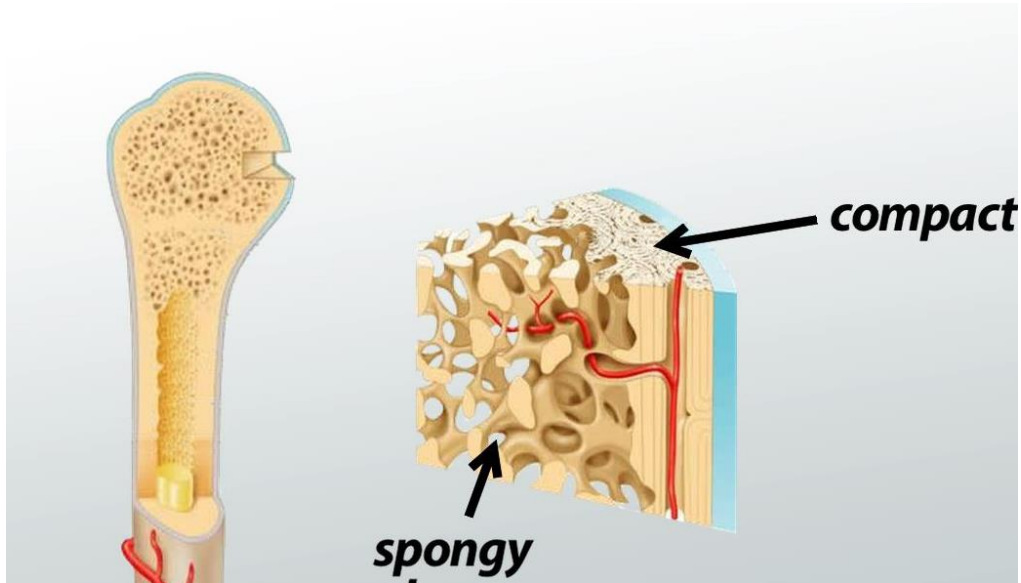
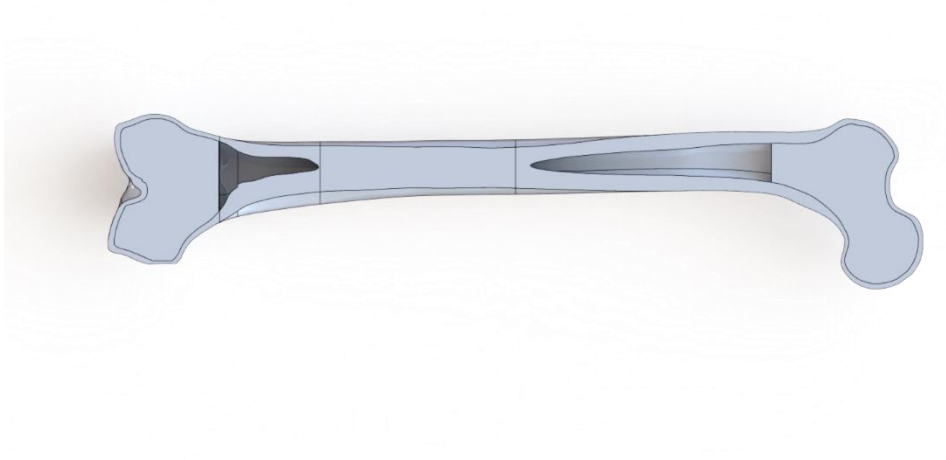


Figure 3.7 Solidworks: Compact Bone (green) – Marrow (blue)

It is important to note that the trabecular or spongy part of the bone was initially incorporated into the femur bone model. However, subsequent Finite Element Analysis (FEA) simulations revealed that there was no significant difference in the results with or without the inclusion of the spongy bone. Given this finding, and in an effort to conserve time and computational resources, we decided to proceed with the remaining simulations without considering the spongy bone in the femoral bone model.



*Figure 3.8 Compact and Spongy Bone*



*Figure 3.9 Assembly of Femur Bone with Spongy Bone*

### 3.2 Distal Femur Plates

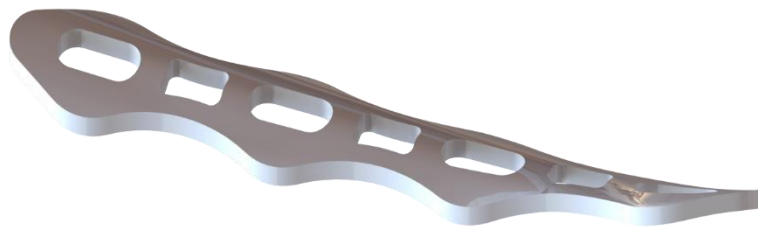
In this chapter, we delve into the design process of the distal femur plates, their assembly, and subsequent meshing for Finite Element Analysis (FEA). It's important to note that the design of the plates and nail was conducted at a surface level, as the primary focus of this thesis pertains to the mechanical strain that develops across the bone defect gap.

The design of the basic plate was inspired by the AxSOS 3 Ti Distal Lateral Femur plate from Stryker [11]. Using Solidworks software, we sketched the basic outline of the distal plate. The body of the plate was then created by extruding the sketch in a plate-bone assembly, utilizing the 'Extrude Boss-> Up to Surface' and 'Surface Knit' features. This ensured optimal contact between the plate and the bone.

Subsequently, we created the necessary holes on the plate using the 'Cut Extrude' feature, culminating in the final design of the main and secondary plates. The design process was meticulous and aimed at achieving a plate that would effectively facilitate the study of mechanical strain across the bone defect gap. It's worth noting that this exact procedure was also replicated for the secondary plate. The secondary plate is used in conjunction with the main plate in cases of double plating, providing additional support and stability to the bone structure.



*Figure 3.10 Main Distal Plate Final Design*



*Figure 3.11 Secondary Distal Plate*

Continuing with the design process, the next step involves the insertion of the locking screws, which serve to secure the plate to the bone. This is achieved by mating the screws with the holes that were created in the plate during the previous step.

Once the screws are in place, we proceed to modify the part of the bone that is to be screwed. This is done using the 'Cavity' feature in Solidworks. By selecting the screws, we are able to create the desired holes in the femur bone. This method ensures a precise fit between the screws, the plate, and the bone, thereby enhancing the stability and effectiveness of the assembly.

It's important to note that this technique is not exclusive to this particular assembly. In fact, it is a standard procedure that we employ for all the models that will be discussed in the subsequent sections of this thesis. This consistent approach ensures that all our models adhere to the same standards of accuracy and precision, thereby enhancing the validity and reliability of our findings.

The final assemblies of single plate, as well as double plating system are presented below.



*Figure 3.12 Single Plate Fixation Assembly*



*Figure 3.13 Double Plating Fixation Assembly*



*Figure 3.14 Double Plate Fixation Assembly – Inner Side*

### 3.3 Retrograde Intramedullary Nailing System

As we transition into the chapter concerning the retrograde intermedullary nailing system, it is crucial to clarify that only the retrograde approach was designed and utilized in this study. The antegrade approach was not considered due to the inherent challenges it presents in cases of distal bone defects.

Specifically, the lack of available bone for the nailing system to secure with screws on the lateral side of the femur makes the antegrade approach impractical, if not impossible, in these instances.

The design of the nailing system was inspired by the Alpha Femur Retrograde Nailing System by Stryker. However, the absence of access to the original drawings of this model added a layer of complexity to the design process. The creation of the essential bends in the nail became a particularly demanding task. The design and assembly of the nail with the bone turned into an iterative process, requiring continuous adjustments and refinements to achieve an accurate and functional model.

Finally, we proceeded to design the necessary holes for the placement of the locking screws. These screws are integral to the functionality of the nailing system, as they secure the nail in place within the bone, ensuring stability and promoting healing. The design and placement of these holes were carefully considered to optimize the performance of the nailing system and to facilitate the secure attachment of the nail to the bone.



*Figure 3.15 Retrograde Intramedullary Nailing System*



*Figure 3.16 Retrograde Nailing System Assembly - Section*



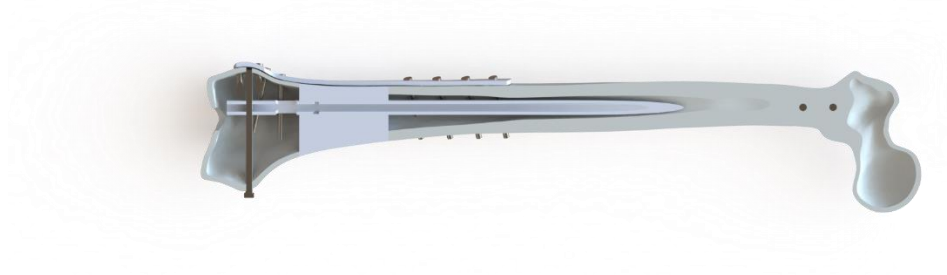


Figure 3.17 Combination of Plate and Retrograde Nail Assembly-Section

### 3.4 Porous Scaffold

In the ensuing chapter, we delve into the design of the porous scaffold. It is important to note at the outset that designing and exporting a model with an actual porous structure is a near-impossible task due to the complex and intricate nature of such structures, which makes the simulation of the FEA practically unsolvable. Consequently, we opted to design a solid model that represents the scaffold, rather than attempting to replicate the actual porous structure.

However, to ensure that our model accurately reflects the mechanical properties of a porous scaffold, we employed a technique known as material homogenization. This approach allows us to assign the appropriate mechanical characteristics to our solid model, effectively simulating the behavior of a porous scaffold. The specifics of the material homogenization process and how it is applied in this context will be elaborated upon in a subsequent chapter.

In the design of the solid model of the scaffold, we utilized a 6cm segment of the lateral side of the femur bone. This was done to ensure that the implant would accurately mimic the actual defected part of the bone. To secure the scaffold implant to the bone, we sketched and extruded two brackets on one side of the body. These brackets were designed to perfectly fit and align the original bone with the implant, ensuring a seamless integration. Additionally, we created holes in the brackets to accommodate locking screws. These screws serve to firmly fixate the implant to the bone, providing a stable and secure connection that is crucial for the success of the implant.

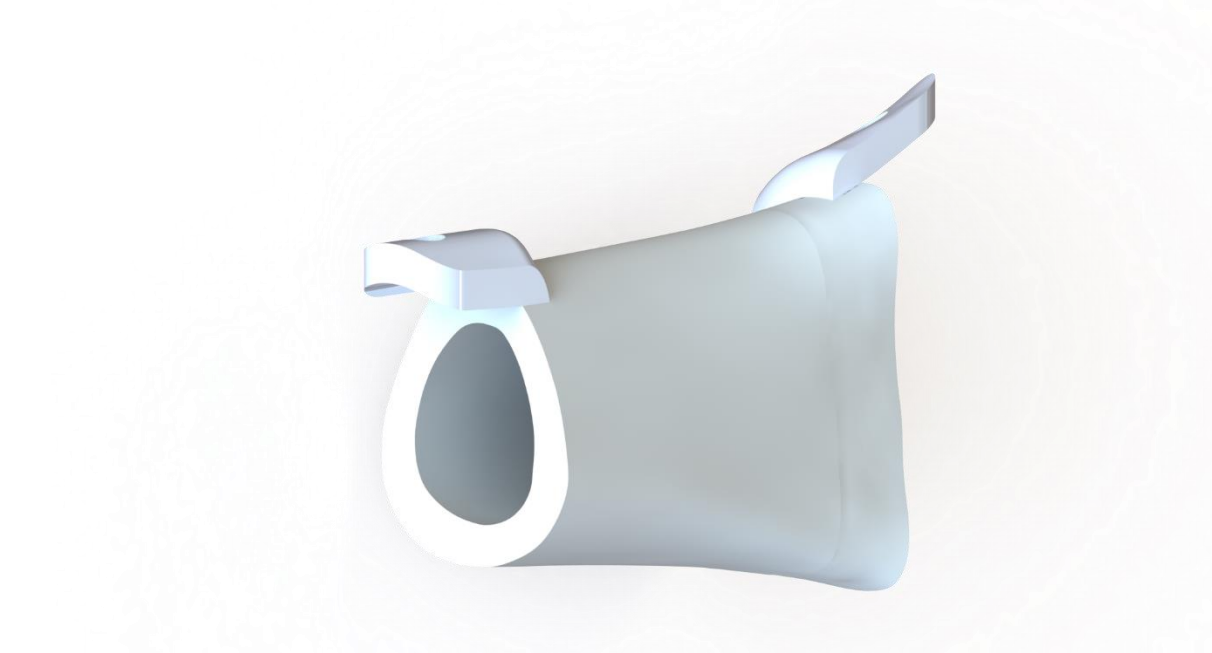


Figure 3.18 Porous Scaffold Implant with Brackets

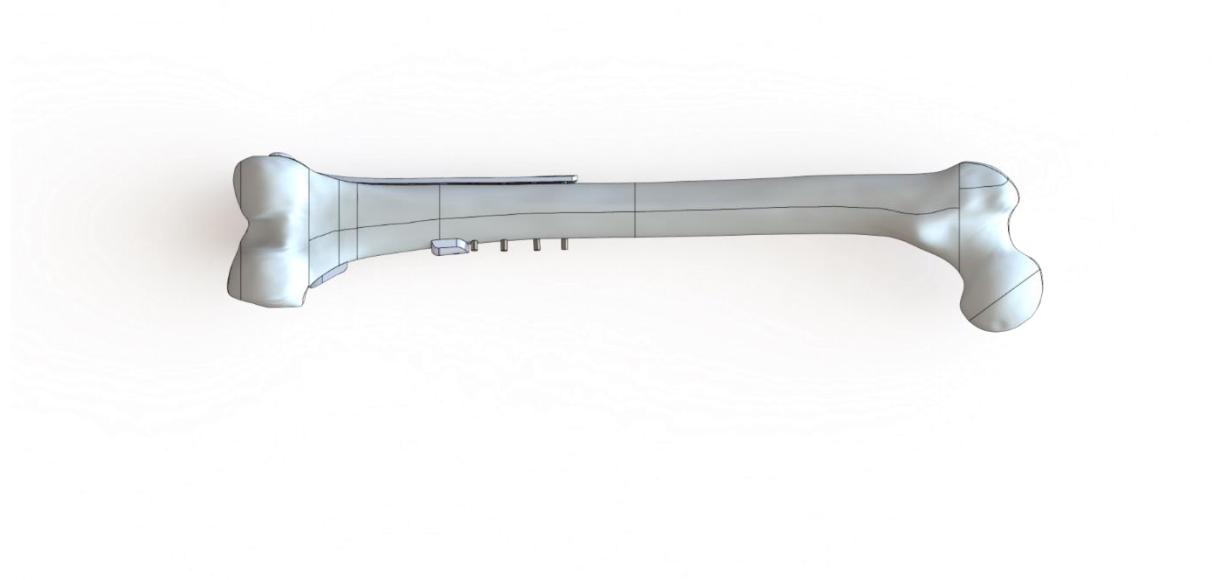


Figure 3.19 Porous Implant and Plate Assembly

### 3.5 Gait Analysis

The gait cycle is a fundamental concept in understanding the biomechanics of walking and running. It refers to the sequence of motions that an individual's lower limb goes through from the moment one foot makes contact with the ground to the moment that same foot contacts the ground again. This cycle is typically divided into two main phases: the stance phase and the swing phase.

The stance phase begins with initial contact (or heel strike) and ends with toe-off. It represents the period during which the foot is in contact with the ground and bears the body's weight. This phase is further subdivided into several stages, including loading response, mid-stance, terminal stance, and pre-swing, each of which involves specific movements and forces.

The swing phase follows the stance phase and represents the period during which the foot is not in contact with the ground. It is also subdivided into initial swing, mid-swing, and terminal swing stages. During this phase, the limb is essentially in motion, preparing for the next stance phase.

Understanding the gait cycle is crucial for the finite element analysis as it allows us to accurately model the forces applied to the femur bone during different stages of walking or running. This, in turn, enables us to predict how different designs of implants or prosthetics might perform under real-world conditions.

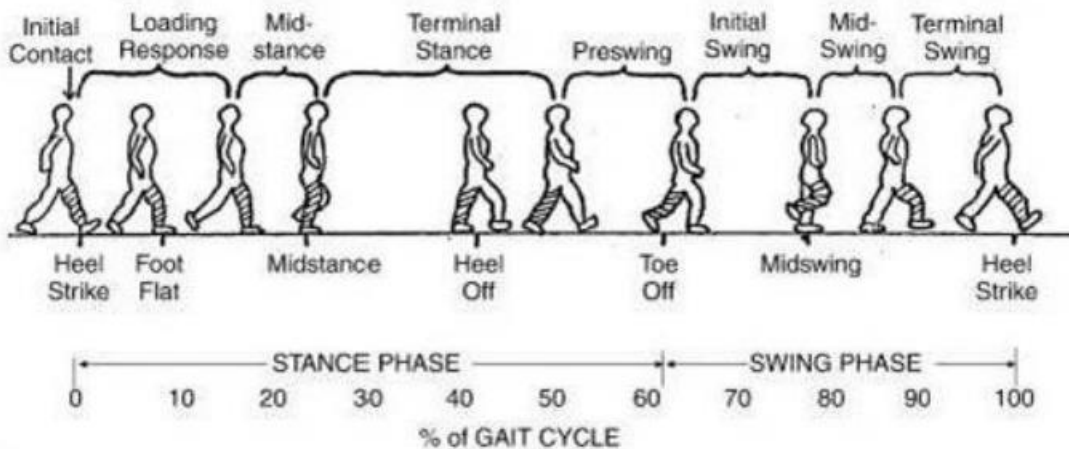


Figure 3.20 Gait Cycle [21]

In the context of the gait cycle, it is noteworthy that the maximum force exerted on the femoral head occurs at approximately 16% of the cycle. This force is estimated to range between 238% and 404% of an individual's body weight (BW) during typical walking activities. Although a total of 28 muscles are engaged during walking, our model, for the sake of simplicity, incorporates only the three primary muscle groups that have the most significant impact on the forces applied to the femur. These include the abductors, the quadriceps (mainly vastus lateralis) and the iliopsoas. According to relevant literature, the forces generated by these muscle groups during walking are within the range of 104-158% BW for the abductors, 58-95% BW for the quadriceps, and 20-32% BW for the iliopsoas [21].

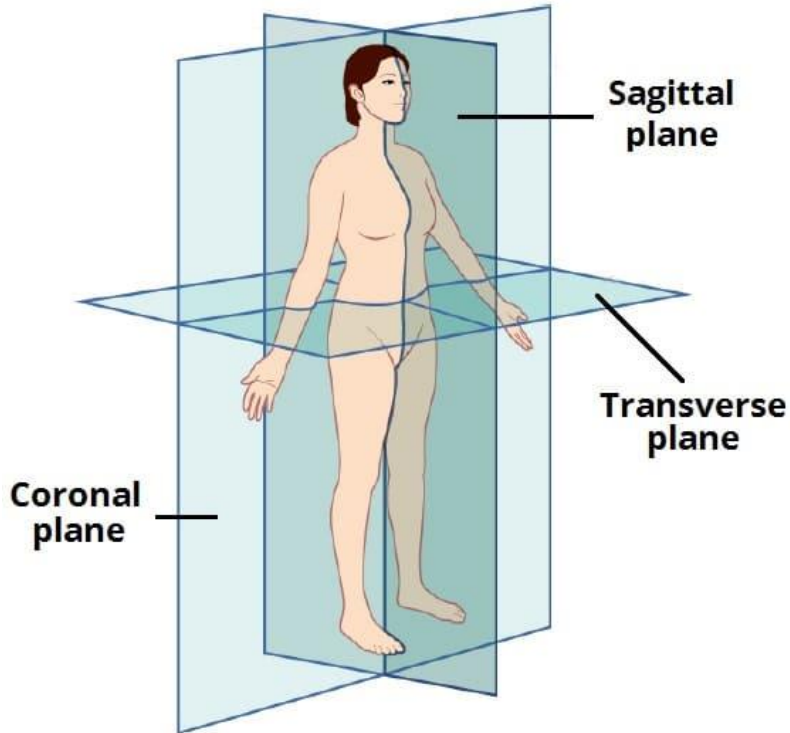


Figure 3.21 Anatomical Planes of Human Body [23]

The force vectors representing the muscle forces are oriented at respective angles with the sagittal plane of  $20^\circ$  medially for the abductors,  $0^\circ$  for the quadriceps, and  $9^\circ$  medially for the iliopsoas. With respect to the coronal plane, the force vectors are oriented at  $0^\circ$  for the abductors,  $0^\circ$  for the quadriceps, and  $47^\circ$  anteriorly for the iliopsoas.

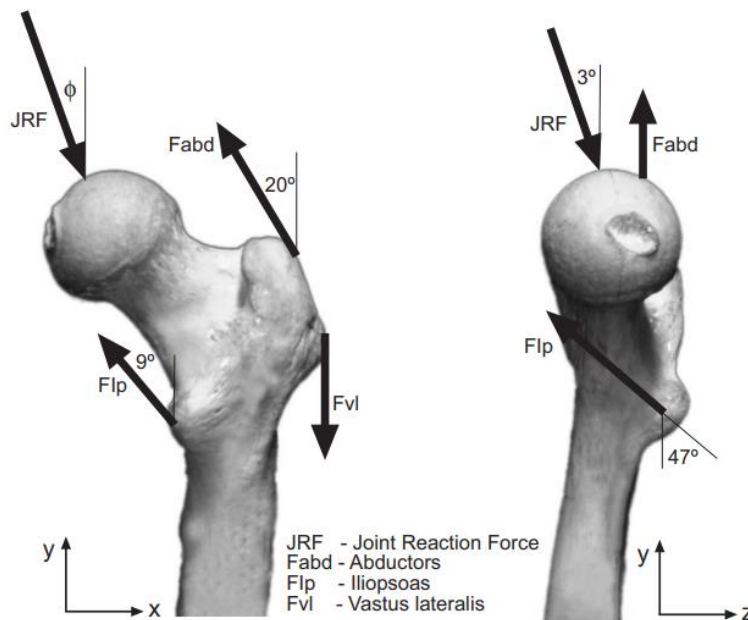


Figure 3.22 Forces Applied on Femur Bone [22]

The force vector for the joint force is strategically positioned on the area of the femoral head that is inserted into the hip socket and makes contact with the acetabulum. This force vector is oriented at an angle of 13° laterally with respect to the sagittal plane and at 3° posteriorly with respect to the coronal plane [22]. The resulting force components, derived from the aforementioned orientations and placements, are presented in the following table.

Table 1 Forces of Gait Cycle on Femoral Head

[N]	Total	X-Component	Y-Component	Z-Component
Joint Reaction	1751	-367	141	1706
Abductors	765	262	0	-719
Iliopsoas	146	15	-106	-100
Vastus Lateralis	427	0	0	427

### 3.6 Preparation and Boundary Conditions for Finite Element Analysis

#### 3.6.1 Material Assignment

In the following chapter of our thesis, we delve into the meticulous process of preparing for simulation runs on ANSYS Mechanical, a crucial step in our research. The first order of business is to specify the materials used for each component of the assembly. This involves assigning each part of the assembly - the bone, the plate etc. - a specific material. Each material is defined by its unique mechanical properties, like Young's modulus and Poisson's ratio. These properties are critical in determining how each component will behave under various loads and constraints during the simulation runs. The mechanical properties for each material are sourced from relevant literature and are presented in detail in the subsequent sections. This meticulous approach ensures that our simulations are as accurate and representative of real-world conditions as possible.

In our research, we identified five distinct types of bone, each with its own unique characteristics and mechanical properties.

1. *Cortical Bone*: This is the hard outer layer of bone that provides the rigidity needed for weight-bearing and protection. It's characterized by its high density and low porosity.
2. *Spongy Bone*: Also known as cancellous or trabecular bone, this type is found at the ends of long bones and in the inner layer of flat bones. It has a porous, honeycomb-like structure that provides strength while being lighter than cortical bone.
3. *Immature Bone*: This is a type of bone that is in the process of formation and maturation. It is softer and less dense than mature bone, and it is gradually replaced by mature bone as the individual grows.
4. *Cartilage Bone*: This is a type of bone that is formed by the replacement of cartilage during the process of endochondral ossification. It is typically found in the growth plates of long bones.

5. *Granulation Tissue*: More like a type of tissue that forms during the healing process of wounds, ulcers, or inflamed tissue. It is characterized by its rich supply of blood vessels and its role in the formation of new connective tissue.

The mechanical properties of each of these bone types, such as their respective Young's modulus, Poisson's ratio, and yield strength, were derived from relevant literature and used in our simulations to accurately represent the behavior of the bone under various conditions [24].

Table 2 Material Properties of Various Bone Types [24]

	<b>Cortical Bone</b>	<b>Marrow</b>	<b>Granulation Tissue</b>	<b>Fibrous Tissue</b>	<b>Cartilage</b>	<b>Immature Bone</b>	<b>Mature Bone</b>
Elastic Modulus (MPa)	20,000	2	0.001-2	2	10	1000	6000
Permeability (m <sup>4</sup> /Ns)	1E-17	1E-14	1E-14	1E-14	5E-15	1E-13	3.7E-13
Poisson's Ratio	0.3	0.17	0.17	0.17	0.17	0.3	0.3
Solid bulk modulus (MPa)	20,000	2300	2300	2300	3400	20,000	20,000
Fluid bulk modulus (MPa)	2300	2300	2300	2300	2300	2300	2300
Porosity	0.04	0.8	0.8	0.8	0.8	0.8	0.8

In the following section we provide comprehensive tables detailing the mechanical properties of each bone type, as they are represented within the ANSYS interface.

Table 3 Material Properties of *Cortical Bone*

	A	B	C	D	E
1	Property	Value	Unit		
2	Material Field Variables	Table			
3	Density	1900	kg m <sup>-3</sup>		
4	Orthotropic Elasticity				
5	Young's Modulus X direction	1.01E+10	Pa		
6	Young's Modulus Y direction	1.01E+10	Pa		
7	Young's Modulus Z direction	1.803E+10	Pa		
8	Poisson's Ratio XY	0.4			
9	Poisson's Ratio YZ	0.3			
10	Poisson's Ratio XZ	0.3			
11	Shear Modulus XY	4E+09	Pa		
12	Shear Modulus YZ	3.3E+09	Pa		
13	Shear Modulus XZ	3.3E+09	Pa		
14	Orthotropic Stress Limits				
15	Tensile X direction	5.3E+07	Pa		
16	Tensile Y direction	5.3E+07	Pa		
17	Tensile Z direction	1.35E+08	Pa		
18	Compressive X direction	-1.31E+08	Pa		
19	Compressive Y direction	-1.31E+08	Pa		
20	Compressive Z direction	-2.05E+08	Pa		
21	Shear XY	6.5E+07	Pa		
22	Shear YZ	6.5E+07	Pa		
23	Shear XZ	6.5E+07	Pa		

Table 4 Material Properties of *Spongy Bone*

	A	B	C	D	E
1	Property	Value	Unit		
2	Material Field Variables	Table			
3	Density	0.5	kg m <sup>-3</sup>		
4	Isotropic Elasticity				
5	Derive from	Young's Modulus and Poi...			
6	Young's Modulus	2E+09	Pa		
7	Poisson's Ratio	0.3			
8	Bulk Modulus	1.6667E+09	Pa		
9	Shear Modulus	7.6923E+08	Pa		

Table 5 Material Properties of *Immature Bone*

	A	B	C	D	E
1	Property	Value	Unit		
2	Material Field Variables	Table			
3	Density	1800	kg m <sup>-3</sup>		
4	Isotropic Elasticity				
5	Derive from	Young's Modulus and Poi...			
6	Young's Modulus	1E+09	Pa		
7	Poisson's Ratio	0.3			
8	Bulk Modulus	8.3333E+08	Pa		
9	Shear Modulus	3.8462E+08	Pa		

Table 6 Material Properties of *Cancellous Bone*

	A	B	C	D	E
1	Property	Value	Unit		
2	Material Field Variables	Table			
3	Density	1100	kg m <sup>-3</sup>		
4	Isotropic Elasticity				
5	Derive from	Young's Modulus and Poi...			
6	Young's Modulus	1E+07	Pa		
7	Poisson's Ratio	0.167			
8	Bulk Modulus	5.005E+06	Pa		
9	Shear Modulus	4.2845E+06	Pa		

Table 7 Material Properties of *Granulation Tissue*

	A	B	C	D	E
1	Property	Value	Unit		
2	Material Field Variables	Table			
3	Density	1100	kg m <sup>-3</sup>		
4	Isotropic Elasticity				
5	Derive from	Young's Modulus and Poi...			
6	Young's Modulus	5E+05	Pa		
7	Poisson's Ratio	0.167			
8	Bulk Modulus	2.5025E+05	Pa		
9	Shear Modulus	2.1422E+05	Pa		

In the context of the other components involved in the simulation, such as plates, nails, screws, and scaffold brackets, these are all composed of a titanium alloy. Titanium alloys are widely used in orthopedic and dental implants due to their high strength, low density, and excellent biocompatibility. They exhibit a unique combination of mechanical properties, including good tensile strength and toughness, which makes them resistant to fracture and failure under physiological loading conditions. Furthermore, titanium alloys are resistant to corrosion in the body's harsh physiological environment, ensuring their longevity once implanted. Lastly, their excellent biocompatibility minimizes the risk of adverse reactions, promoting successful integration with the surrounding bone tissue.

Ti-6Al-4V, also known as Grade 5 titanium, is a popular choice for **porous scaffolds** in bone implants due to its unique combination of properties. It is a titanium alloy, with 6% aluminum and 4% vanadium, which contributes to its superior mechanical strength, light weight, and excellent biocompatibility. The mechanical strength of Ti-6Al-4V is similar to that of human bone, which minimizes the risk of stress shielding - a phenomenon where the implant bears the load instead of the bone, leading to bone resorption and eventual implant loosening. Its light weight makes it comfortable for patients and reduces the load on the skeletal system. In terms of biocompatibility, Ti-6Al-4V is resistant to corrosion in the body and does not elicit a significant immune response, reducing the risk of adverse reactions. It also supports osseointegration, the process where new bone grows on and bonds with the surface of the implant, which is crucial for the stability and longevity of the implant.



The porous structure of the scaffold, made possible by modern manufacturing techniques like 3D printing, further enhances these properties. The pores allow for the ingrowth of bone and vascular tissue, improving integration with the surrounding bone. They also reduce the overall weight of the implant and can be designed to mimic the structure of natural bone, optimizing load distribution.

Therefore, Ti-6Al-4V is an ideal material for porous scaffolds in bone implants due to its strength, light weight, biocompatibility, and compatibility with porous structures [25,26].

the material properties for both the Titanium Alloy and Ti-6Al-4V are sourced directly from the ANSYS library, which provides a comprehensive and reliable database of material properties.

Table 8 Material Assignment and References

Model Part	Material	Reference
Bone Models	Cortical Bone	Table 3
	Spongy Bone	Table 4
	Immature Bone	Table 5
	Cartilage Bone	Table 6
	Granulation Tissue	Table 7
Porous Scaffold	Ti-6Al-4V	Ansys Material Library
Scaffold Brackets	Titanium Alloy	
Plates		
Nailing System		
Screws		

### 3.6.2 Contact Definition

In the subsequent chapter of our study, we inspect the crucial task of defining the contacts between the various components within the ANSYS environment. This step is of great importance as it dictates how the different parts of our model interact with each other during the simulation. The accurate definition of these interactions is fundamental to the reliability of our results. In a real-world scenario, the bone, plates, screws, and scaffold are not isolated entities; they interact with each other, transferring forces and responding to the mechanical environment as a unified system. By meticulously defining the contacts in our ANSYS model, we are able to replicate this complex interplay, thereby enhancing the realism and accuracy of our simulations.

In the ANSYS Static Structural environment, there are several types of contact that can be defined between components. These include Bonded, Frictional, and Frictionless contacts, each of which has unique characteristics and applications.

1. **Bonded Contact:** This type of contact is used when the components are assumed to be perfectly adhered or glued together. There is no relative motion between the surfaces in contact, and they behave as a single entity. This is often used when modeling welded or glued connections, or when the components are in such close contact that they can be assumed to move together.

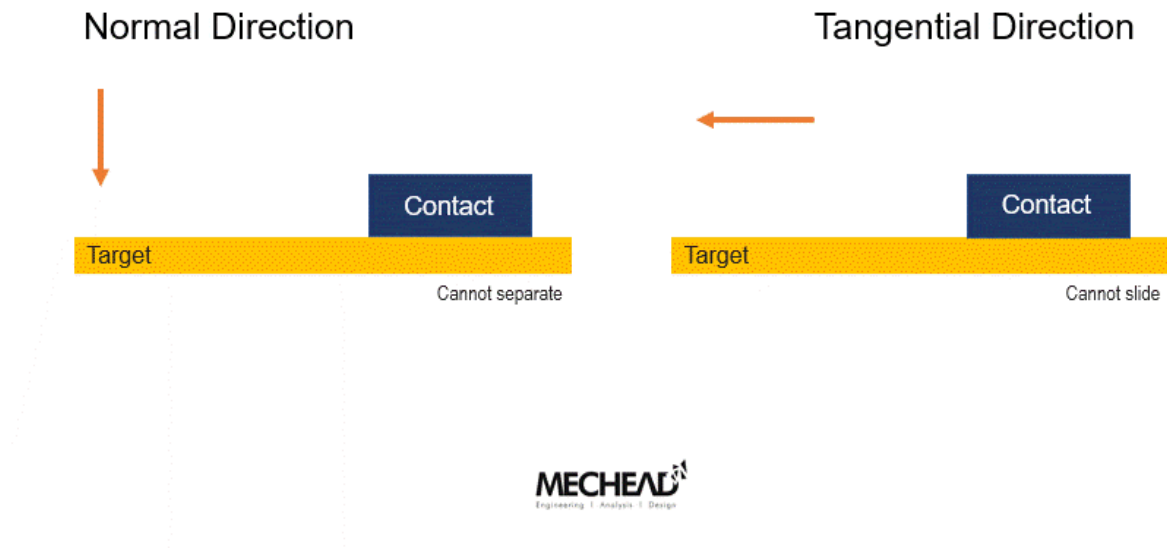


Figure 3.23 ANSYS Bonded Contact [27]

2. Frictional Contact: This type of contact allows for relative sliding between the components, but resists this motion based on a defined coefficient of friction. This is used when the components are in contact but can slide against each other, such as the interaction between a tire and the road.

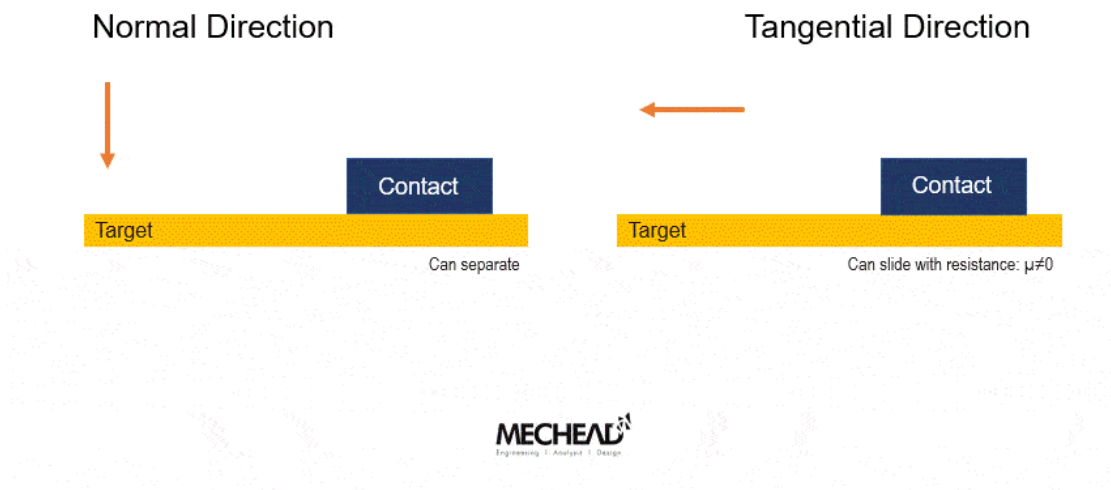


Figure 3.24 ANSYS Frictional Contact [27]

3. Frictionless Contact: This type of contact also allows for relative sliding between the components, but does not resist this motion - i.e., there is no friction. This is used when the components are in contact but can freely slide against each other.

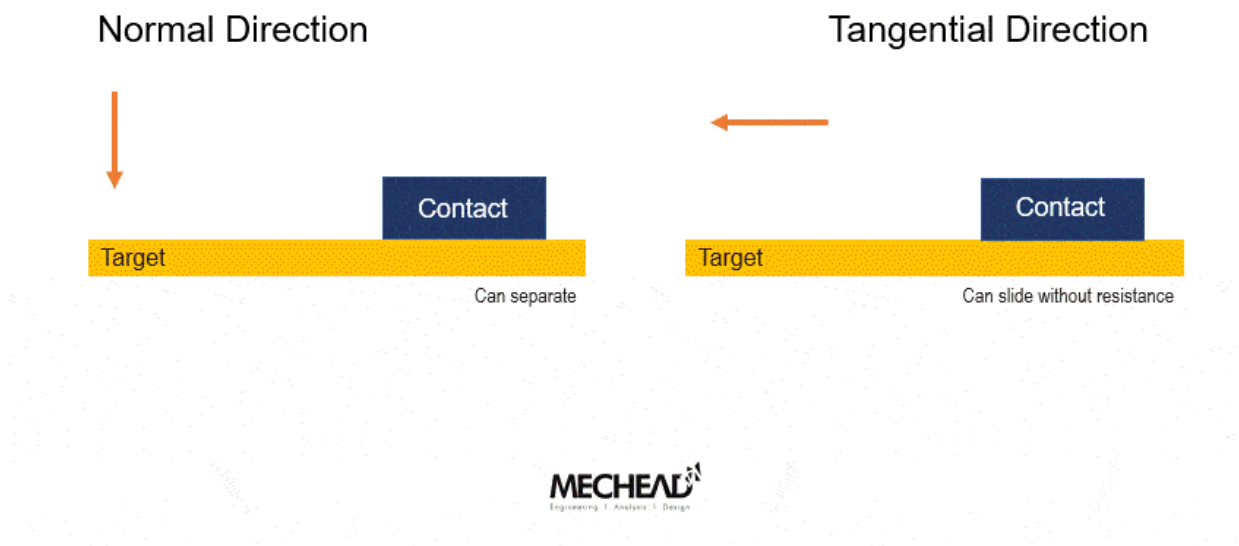


Figure 3.25 ANSYS Frictionless Contact [27]

In our computational model, all screws are of the locking type. This design choice guarantees a bonded connection with both the bone and the plate or nail into which they are screwed. This bonded connection simulates the real-world scenario where the screws are tightly secured, preventing any relative motion between the components. Additionally, the brackets of the scaffold are inherently bonded with the porous scaffold by design. This ensures that the scaffold and its brackets behave as a single unit during the simulations, accurately reflecting the intended design of the scaffold implant.

Then we turn our attention to the frictional contacts, which are representative of the interaction between the plate and the bone. The friction coefficient in such scenarios can fluctuate between 0.3 and 1.3, contingent upon a variety of factors. For the purposes of our analysis, we have opted to adopt a conservative approach and set the coefficient at the lower limit of this range, i.e., 0.3 [28]. Frictional contacts are also indicative of the interface between the bone fragments, as well as the bone and the porous implant. Based on a comprehensive review of the relevant literature, we have determined that the friction coefficient between two bone surfaces is approximately 0.4 [29]. In contrast, the friction between the scaffold and the bone is considered slightly higher, estimated to be around 0.5.

Contacts	Bone (All Types)	Porous Scaffold	Scaffold Brackets	Plates	Nailing System	Screws
Bone (All Types)	Frictional - 0.4	Frictional - 0.5	Frictional - 0.3	Frictional - 0.3	Frictional - 0.3	Bonded
Porous Scaffold		-	Bonded	Frictional - 0.3	-	-
Scaffold Brackets			-	-	-	Bonded
Plates				-	-	Bonded
Nailing System					-	Bonded
Screws						-

Figure 3.26 Contact between models

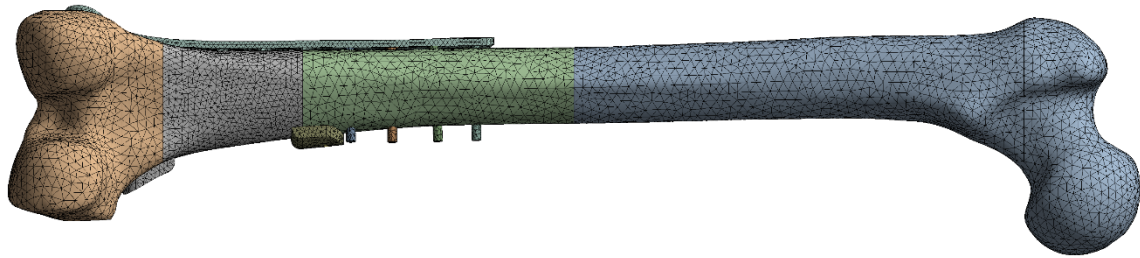
### 3.6.3 Geometry Meshing

In the ensuing chapter of our study, we examine the intricacies of meshing, a critical aspect of our simulation. Meshing, in essence, involves the division of the geometry of an object into a finite number of elements, thereby enabling the accurate computation of variables such as stress and strain at discrete points. The choice of meshing method and element size can significantly influence the accuracy of the results, thus underscoring its importance.

In our simulation, we opted for the patch conforming method, which employs tetrahedrons as the primary elements. This choice was motivated by the versatility of tetrahedrons, which can adapt to complex geometries with relative ease, thereby ensuring a more accurate representation of the actual structure.

The element size was determined based on the significance of each part in the simulation. For instance, the porous scaffold and the cartilage bone, whose strain is of paramount importance for osteogenesis, were assigned a mesh size of 2.5 mm. On the other hand, the cortical bone, which is less critical for the simulation, was assigned a larger mesh size of 4 mm.

Similarly, the plates and screws, despite their smaller size, were also assigned a mesh size of 2 mm. This decision was informed by the primary focus of our study, which is the strains developed between the bone defect. As such, the design and resistance to stresses of the plates and screws were deemed less significant, thereby justifying the larger mesh size.



0.00 50.00 100.00 (mm)  
25.00 75.00

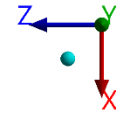
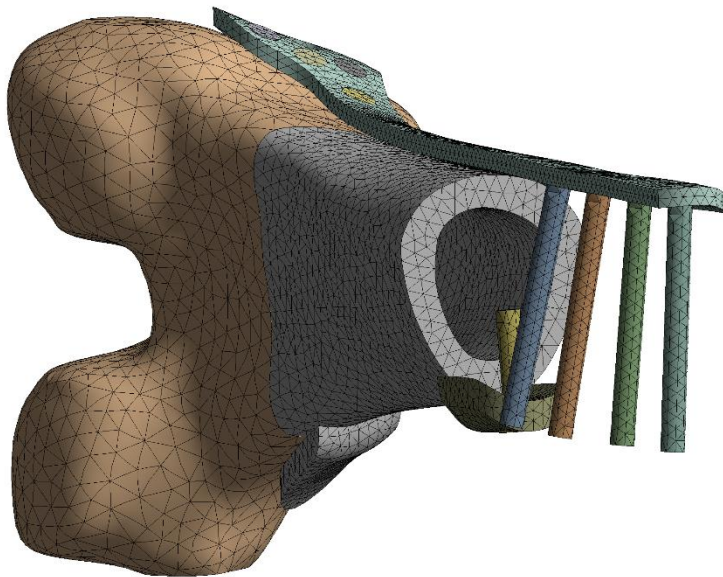


Figure 3.27 ANSYS: Mesh Example



0.00 30.00 60.00 (mm)  
15.00 45.00

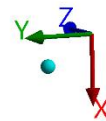


Figure 3.28 Scaffold, Screws and Plate Mesh

Table 9 Meshing Method and Element Size for Every Model

Model Part	Comforming Method	Mesh Size (mm)
Cortical Bone	Tetrahedrons	4
Spongy Bone		4
Immature Bone		2
Cartilage Bone		2
Granulation Tissue		2
Porous Scaffold		2
Scaffold Brackets		2
Plates		2
Nailing System		2
Screws		2

An important note on meshing pertains to the practical considerations of computational resources and time. The mesh sizes we have outlined are indeed optimal for capturing the most accurate results. However, they are not always feasible to implement in every simulation due to the substantial computational power and time they require.

To address this, we conducted a mesh sensitivity analysis. This analysis revealed that using larger meshes does not significantly alter the conclusions drawn from our simulations. Therefore, we can confidently assert that similar results would be obtained even with the use of larger, less computationally demanding meshes. This finding allows us to strike a balance between computational efficiency and the accuracy of our simulation results.

### 3.6.4 Simulation Analysis Settings

In the following chapter, we look into the critical decisions made concerning the analysis settings in the Static Structural simulations. One of the most significant choices is the enabling of large deformation. This is a crucial aspect as it takes into account the changes in geometry (and hence changes in stiffness) during the load application. This is particularly important in scenarios where large strains are expected, such as in the modeling of bone structures under significant loads. Without this option enabled, ANSYS would assume that the geometry remains constant throughout the load application, which could lead to inaccurate results when the deformations are large. Therefore, to accurately capture the behavior of the structure, the large deformation option is enabled.

Furthermore, all the forces are applied in a single step of 1 second, divided into 10 substeps. Only in extreme and hard-to-converge solutions, this substep may have been increased up to 25. The Weak Springs are turned on with program-controlled stiffness, which helps to stabilize the model and aids in convergence. Lastly, the Newton-Raphson nonlinear control is set to unsymmetric due to the large

frictional coefficient used in contacts. This setting is used to solve the nonlinear equations that arise from the large deformations and contact conditions, ensuring a more accurate and stable solution.

Table 10 Simulation Analysis Settings

Analysis Settings	
Number of Steps	1
Substeps	10
Large Deflection	On
Weak Springs	On
Newton-Raphson	Unsymmetric

### 3.6.5 Application and Analysis of Forces and Supports

In the ensuing chapter, we explore the application of forces and supports on the femur bone, a critical aspect of our simulation. The accurate application of these forces and supports is crucial as they directly influence the results of the simulation, dictating the stress distribution and deformation patterns within the bone structure. In terms of support, a fixed support is applied solely at the lateral and medial condyles of the femur. This is because, in the context of our simulation, the hip joint is now exerting force on the femur. This fixed support mimics the natural constraints of the knee joint, which restricts movement in certain directions. Drawing from the gait analysis discussed in a previous chapter, we have already determined the forces that will be applied (Table 1). These forces, derived from the peak force exerted on the femoral head during the gait cycle, along with the forces produced by the primary muscle groups, will be used to simulate the physiological conditions experienced by the femur during ambulation.

**H: Plate DiamondFinal**

Static Structural  
Time: 1. s  
09/07/2023 19:53

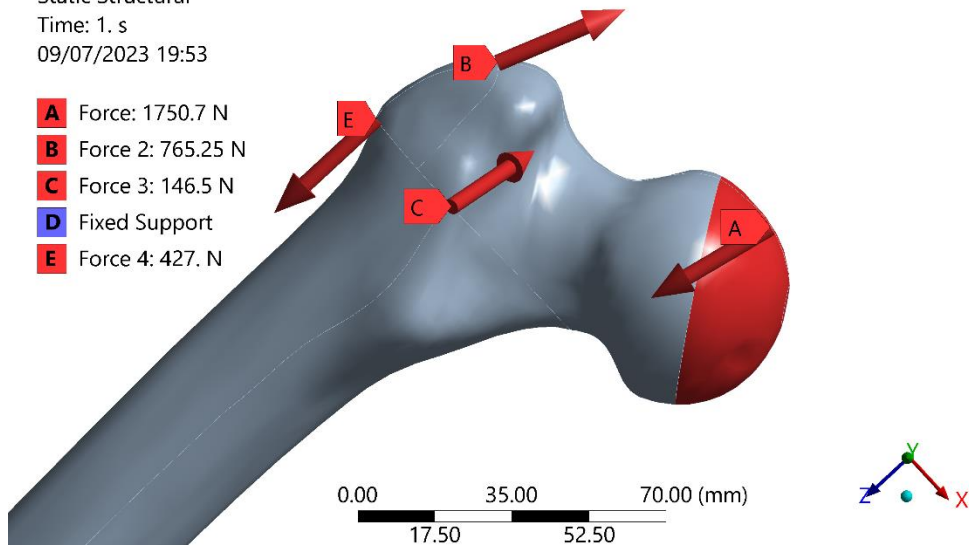


Figure 3.29 Forces Applied on Femur Head

**H: Plate DiamondFinal**

Static Structural  
Time: 1. s  
09/07/2023 19:52

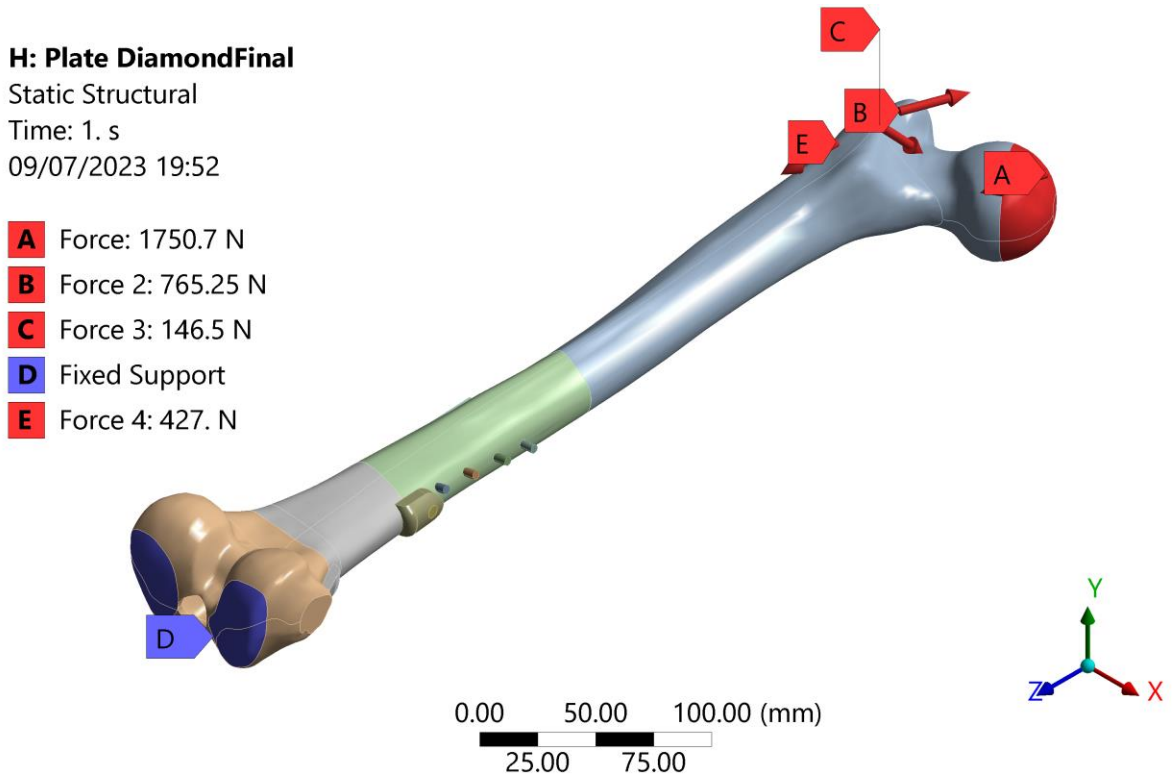


Figure 3.30 Support and Forces on Femur Bone



## 4. Exploring Non-Scaffold Approaches to Bone Defect Healing

### 4.1 Non-Scaffold Specifications

In this chapter, we focus into the exploration of managing bone defects solely through the use of plates and nails, without the incorporation of a scaffold implant. This approach necessitates a revisit to a prior chapter where we discussed the stages of wound healing. The healing process of a bone defect is a complex and dynamic process, involving a series of biological events that lead to the restoration of bone continuity. In the initial stage of healing, **cartilage bone** is generated in the defect. This stage is crucial as it sets the foundation for the subsequent healing stages. Therefore, understanding the strains applied during this stage is of paramount importance. Through our simulations, we examine these strains to gain insights into the biomechanical environment of the healing bone.

In the subsequent simulations, we shift our focus to a later stage in the healing process, where immature bone has formed. **Immature bone**, also known as woven bone, is the first type of bone formed during bone repair. It is characterized by its relatively low strength and its ability to be remodeled into mature bone. By conducting simulations for this stage, we aim to understand how the biomechanical environment changes as the healing process progresses and how this affects the effectiveness of the treatment approach.

The overarching goal of this chapter is to discern which non-scaffold approach - whether it be a single plate, double plate, or a combination of plate and nail - is most effective and efficient for bone defect healing. By comparing the results of the simulations for the different approaches, we aim to provide insights into the optimal treatment strategy for bone defects. This could potentially lead to improved patient outcomes and a better understanding of the biomechanics of bone healing.

Table 11 Approaches without Porous Scaffold

Non-Scaffold Approaches
Plate
Retrograde Nailing
Plate and Nailing
Double Plate

In our simulation, the modeling of cartilage or immature bone is approached with a few key assumptions. We consider it as a solid geometry that precisely mirrors the geometry of the defected bone. This assumption is based on the understanding that during the healing process, the newly formed cartilage or immature bone fills the defect, adopting its shape and dimensions.

It's also important to clarify the nature of the contact between the healthy cortical bone and the newly formed cartilage or immature bone. In the context of our simulation, we assume this contact to be **bonded** rather than frictional. This assumption is grounded in the biological reality of the healing process. The cartilage or immature bone that develops in the defect is essentially an extension of the healthy bone. It is not a separate entity sliding against the healthy bone, but rather a continuation of it,

growing and integrating into the existing bone structure. Therefore, a bonded contact, which implies a fixed, inseparable connection, is a more accurate representation of this biological process in our simulation.

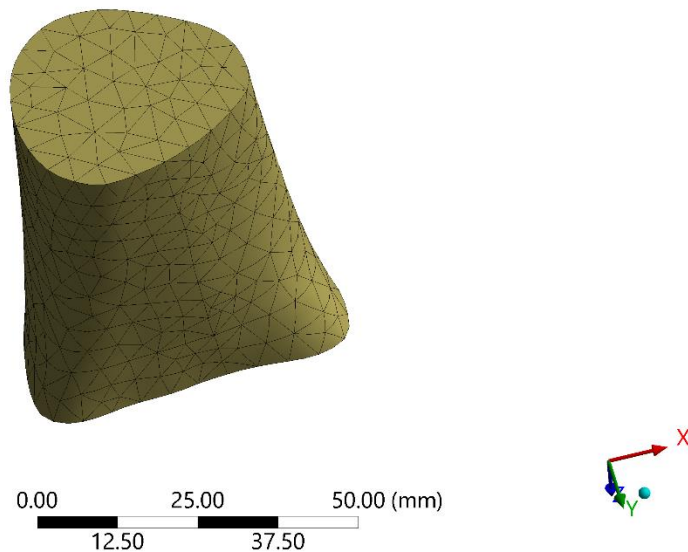


Figure 4.1 Tissue Model in Defect Gap

## 4.2 Initial Stage - Cartilage Bone

In the following chapter, we specifically focus on scenarios where cartilage bone fills the defect. It is important to note that our primary interest lies in the strain values at the interface between the healthy and the cartilage bone. This is the critical region where bone regeneration initiates, and thus, understanding the strain dynamics here is crucial for evaluating the effectiveness of each approach.

However, while focusing on this interface, we must not overlook the overall structural integrity of the femur. In particular, we need to monitor the total deformation of the femoral head. In some scenarios, the deformation might become unrealistic, indicating that the particular approach is not feasible in real-world applications (Figure 4.2).

To gain a comprehensive understanding of each approach, we conduct the simulation under three different total force conditions. Apart from the full load on the femur, derived from the gait analysis which simulates walking, we also simulate scenarios with half and a quarter of this load. This allows us to assess the patient's optimal mobility under each approach, providing a more nuanced understanding of the potential outcomes and justifying the best approach.

In the subsequent sections, we offer a comprehensive display of the strain dynamics at the interface between the healthy and cartilage bone for each non-scaffold approach. This includes visual representations that illustrate the distribution and intensity of strains developed under different conditions.

Furthermore, we provide a detailed tabular breakdown for each approach under every force condition. These tables not only present the maximum strain observed at the interface but also provide an average strain value. This dual-perspective approach to presenting strain values allows better understanding of the strain dynamics in the interface region. By combining these visual and tabular presentations, we aim to offer a thorough and insightful analysis of the strain behavior under different conditions and approaches.

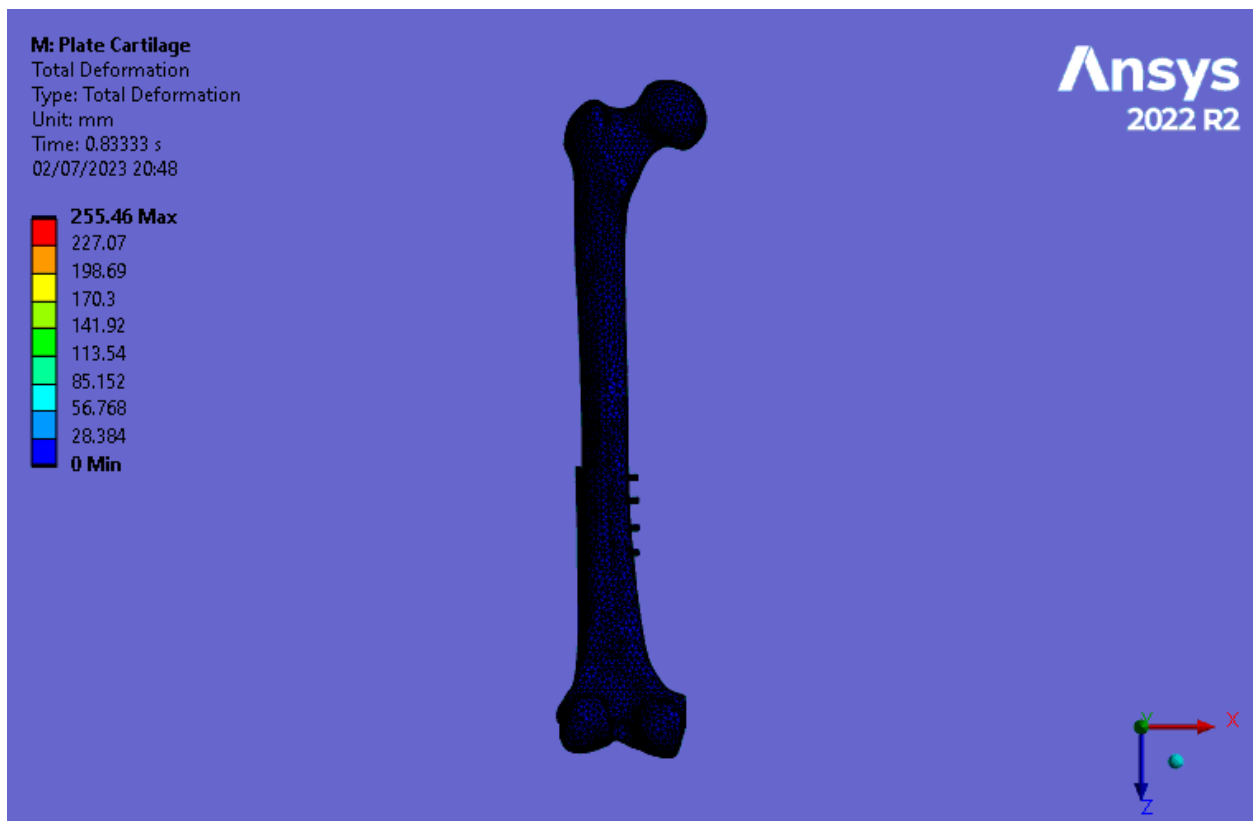


Figure 4.2 Plate Cartilage - Full Load - Unrealistic Deformation

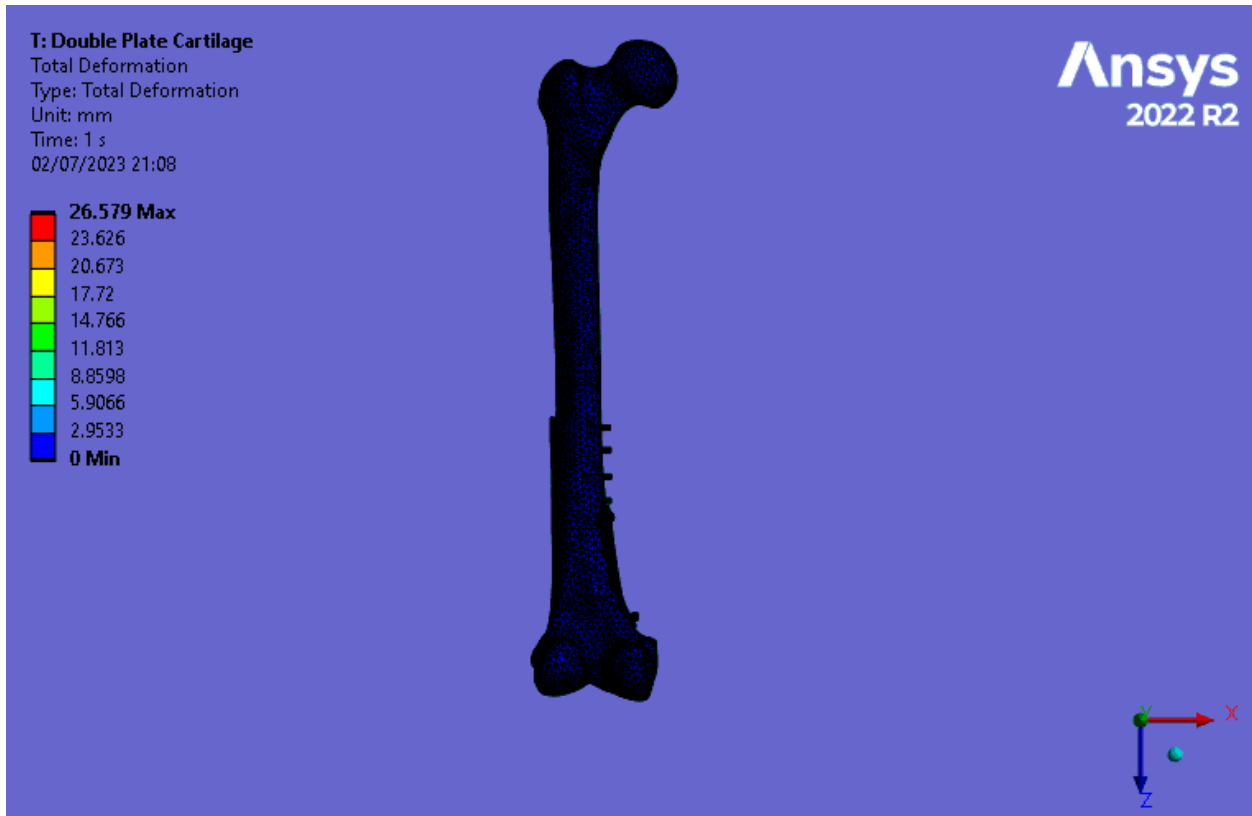


Figure 4.3 Double Plate Cartilage - Full Load - Realistic Deformation

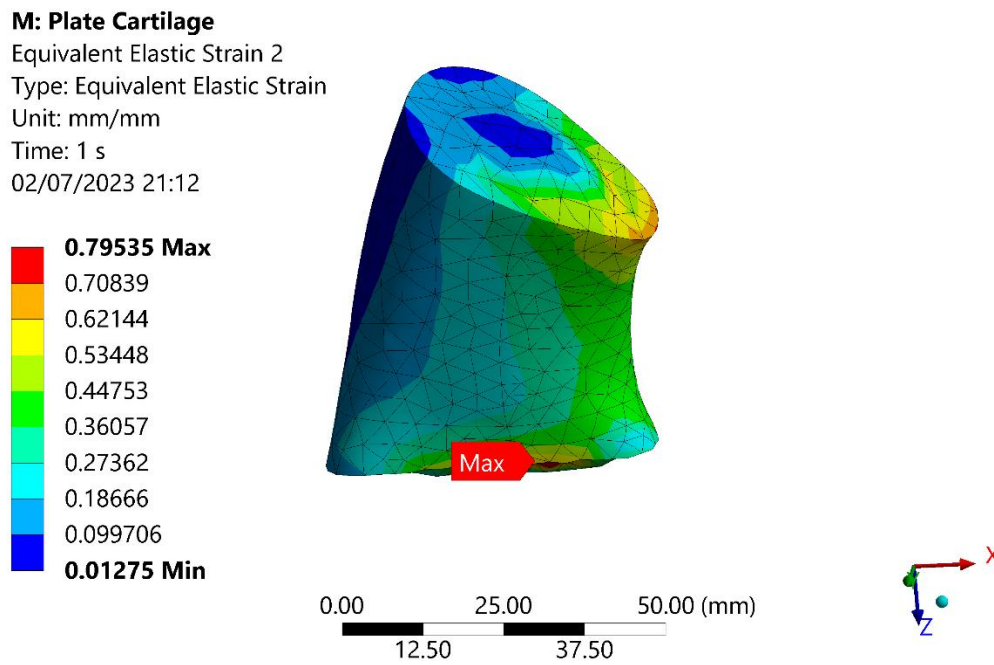


Figure 4.4 Strains for Plate Cartilage - Full Load - Unrealistic Deformation

**T: Double Plate Cartilage**

Equivalent Elastic Strain 2  
 Type: Equivalent Elastic Strain  
 Unit: mm/mm  
 Time: 1 s  
 02/07/2023 21:13

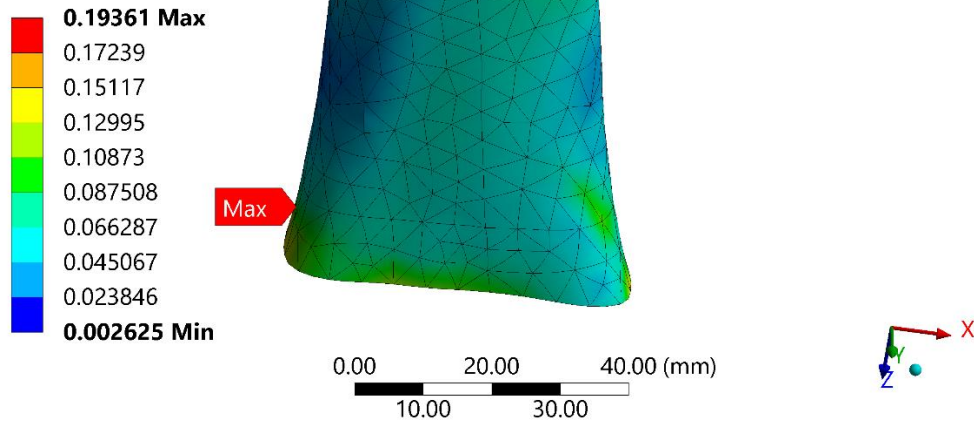


Figure 4.5 Strains for Double Plate Cartilage - Full Load - Realistic Deformation

Table 12 Table of Strains and Deformations for Initial Stage

	Cartilage Bone			
	Gait Load	Deformation (mm)	Max Strain	Avg Strain (Contact)
Plate	Full	255	80%	50%
	Half	144	42%	33%
	25%	80	21%	12%
Retrograde Nailing	Full	x	x	x
	Half	68	30%	18%
	25%	38	16%	8%
Plate and Nailing	Full	52	25%	14%
	Half	31	18%	8%
	25%	17	9%	6%
Double Plate	Full	27	19%	11%
	Half	18	10%	5%
	25%	8	4%	2.50%

Upon reviewing the table, several noteworthy observations can be made. Firstly, it is evident that the simulation involving the full load retrograde nailing system was unable to converge to a result. This suggests that this approach may not be feasible under high load conditions.

Furthermore, cells highlighted in red indicate scenarios where the deformation and strain values were unrealistic. These scenarios are likely not viable solutions to our problem due to the excessive strain they impose on the bone.

Conversely, cells marked in green represent ideal strain conditions. These scenarios yielded strain values within the optimal range for bone regeneration, suggesting that they could potentially provide effective solutions to our problem. These results underscore the importance of carefully considering the loading conditions and the choice of fixation method when addressing bone defects.

It is also important to note that the maximum strain values, as depicted in the figures, refer to a very small area of the interface. Consequently, these maximum values may not provide a comprehensive understanding of the overall strain conditions. Therefore, our primary focus is on the average strain values across the interface, as these provide a more representative indication of the overall strain conditions within the bone.

A more definitive conclusion regarding the optimal choice of fixation method will be drawn at the conclusion of this chapter.

### 4.3 Later Stage – Immature Bone

In the subsequent chapter, we adhere to the same procedure as before, with the sole distinction being the use of immature bone material in place of cartilage. At this advanced stage, we operate under the assumption that the bone has progressed to a more mature phase. It is crucial at this juncture to simulate and assess our approaches under each load condition, given the evolved state of the bone.



Figure 4.6 Plate Immature - Full Load – Deformation



Figure 4.7 Double Plate Immature - Full Load – Deformation

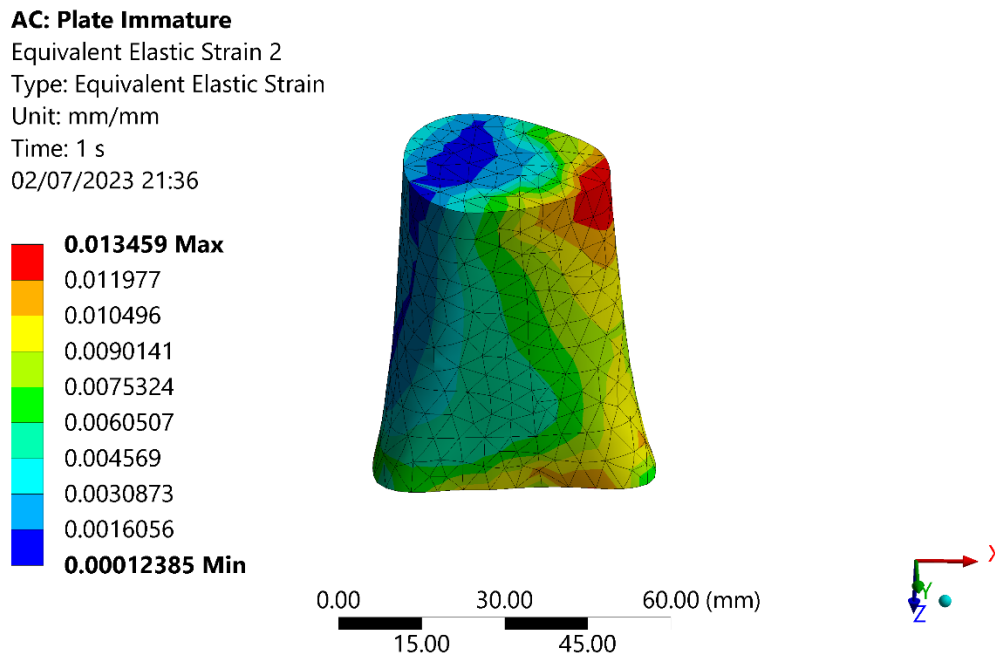


Figure 4.8 Strains for Plate Immature - Full Load – Deformation

**AE: Double Plate Immature**

Equivalent Elastic Strain 2  
 Type: Equivalent Elastic Strain  
 Unit: mm/mm  
 Time: 1 s  
 02/07/2023 21:47

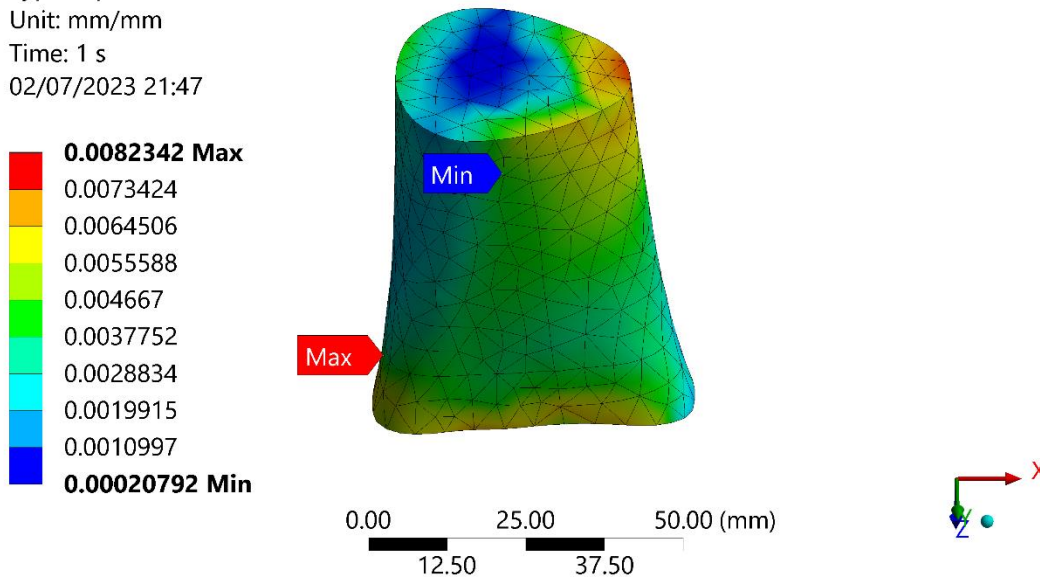


Figure 4.9 Strains for Double Plate Immature - Full Load – Deformation

Table 13 Table of Strains and Deformations for Later Stage

	Immature Bone			
	Gait Load	Deformation (mm)	Max Strain	Avg Strain (Contact)
Plate	Full	15	1.30%	0.90%
	Half	8	0.60%	0.40%
	25%	4	0.35%	0.20%
Retrograde Nailing	Full	22	1.60%	1.20%
	Half	11	0.90%	0.60%
	25%	6	1.20%	0.80%
Plate and Nailing	Full	13	1.20%	0.70%
	Half	6.6	0.60%	0.30%
	25%	3.4	0.32%	0.15%
Double Plate	Full	10.6	0.82%	0.48%
	Half	5.3	0.40%	0.25%
	25%	2.7	0.20%	0.10%

Upon examining the above table, it is both anticipated and evident that the average strains are significantly lower than in the previous stage. At this mature stage of bone healing, all proposed solutions appear to be practically viable.



#### 4.4 An Alternative Approach

In the subsequent chapter, we explore an alternative approach to simulating the problem, with the primary difference lying in how we treat the cartilage (or immature) bone developing in the defect area. We now posit that the cartilage model part is not actually bonded to the healthy bone, but rather, they share a frictional contact with a frictional coefficient of 0.5. This hypothesis necessitates a modification in the geometry of the cartilage part. Given the absence of constraints, using the previous geometry would result in the cartilage part detaching from the assembly, rendering the solution unfeasible. To circumvent this, we expand the cartilage model to maintain contact with the healthy bone, regardless of the movement. Additionally, we introduce a frictionless support on the upper and lower sides to prevent unrealistic deformation of the cartilage, as shown below.

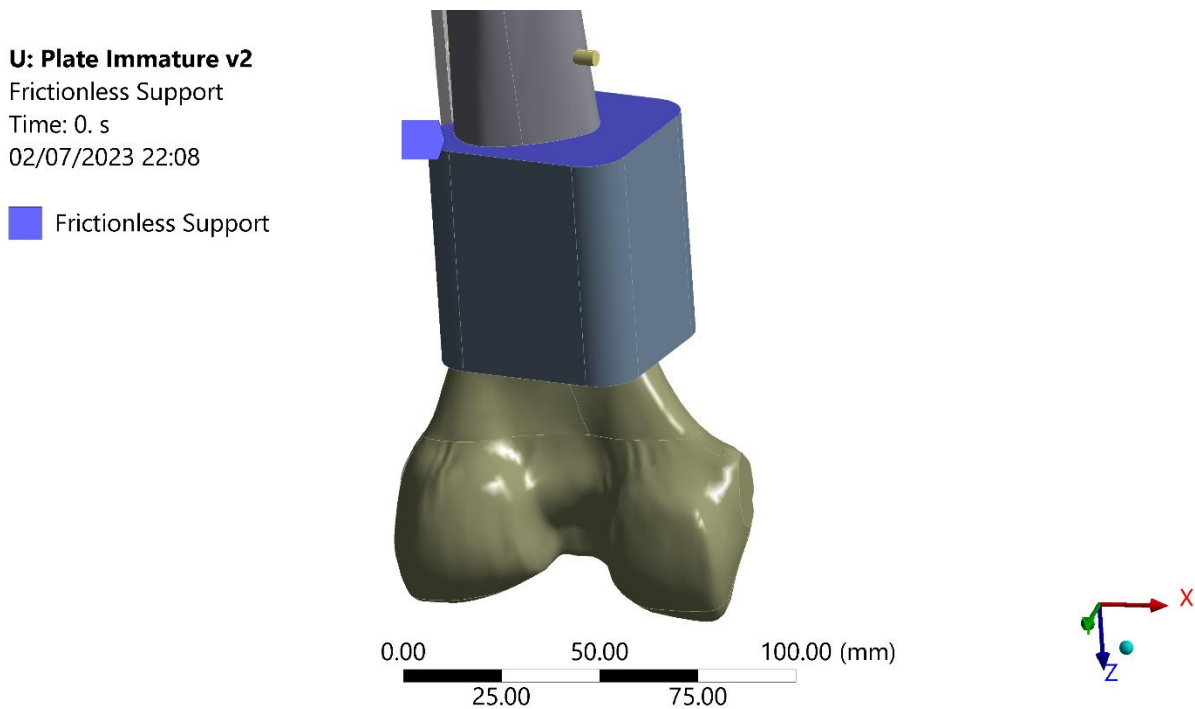


Figure 4.10 Alternative Approach of Cartilage Bone

Given the extensive scope of this thesis, we were unable to analyze this approach by testing all different fixation methods. However, we can conclude that this may serve as a promising avenue for future research. The strains developed at the interface for both cartilage and immature bone are illustrated in the subsequent figures.

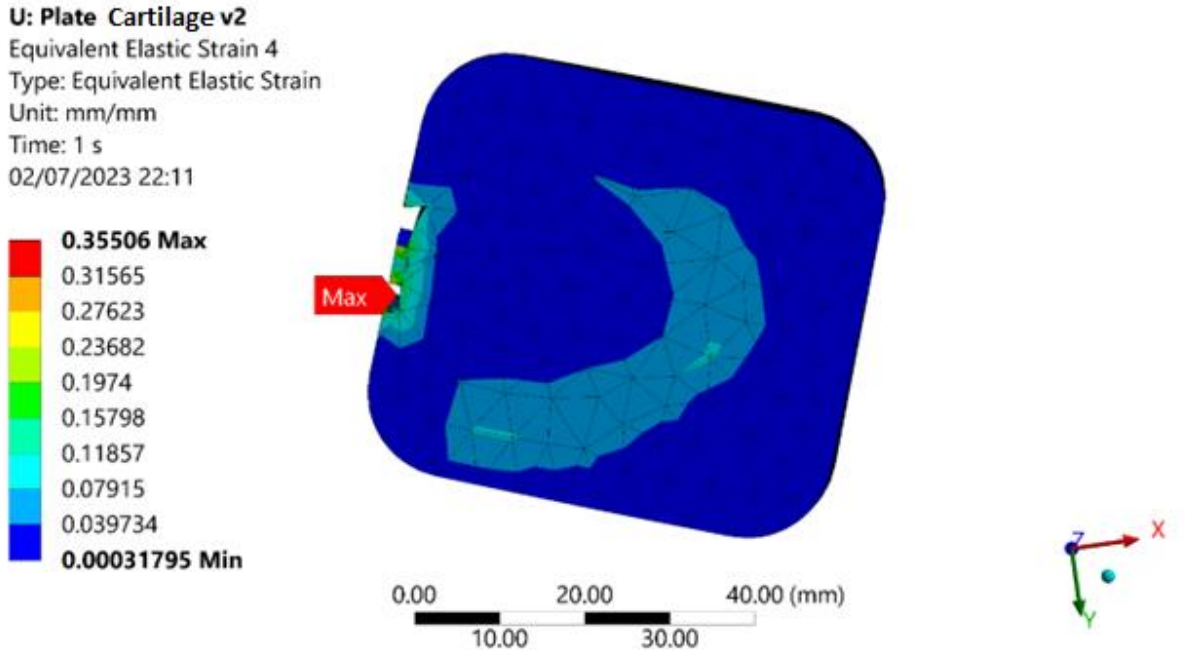


Figure 4.11 Cartilage Bone Strains – Swollen Model

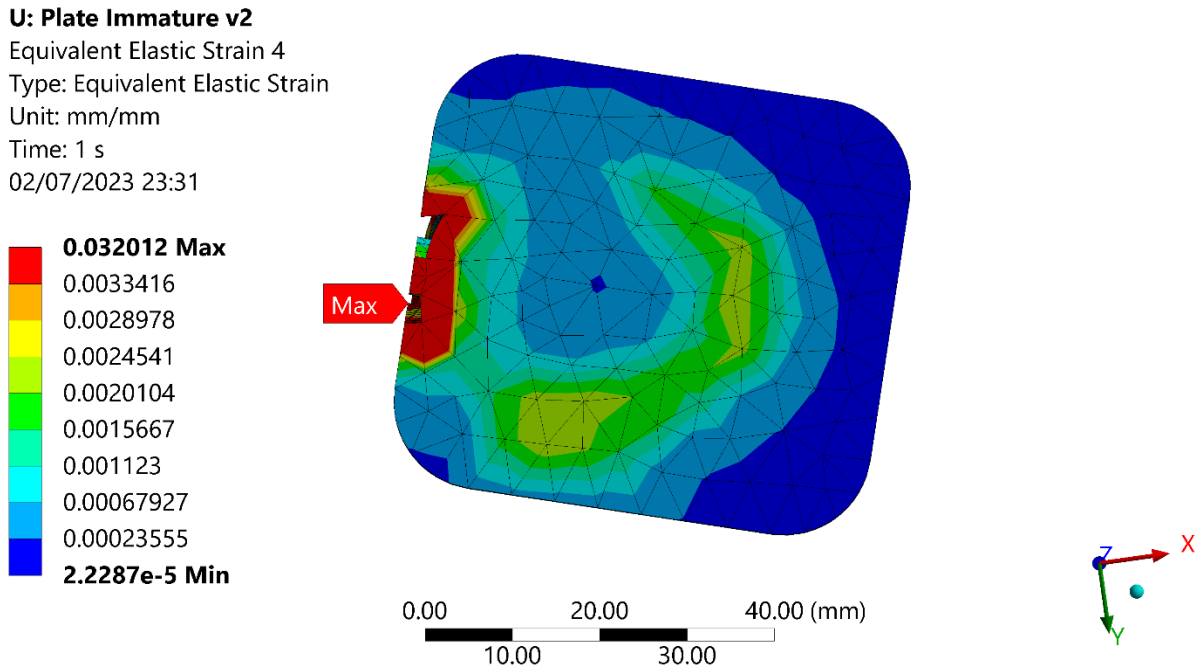


Figure 4.12 Immature Bone Strains – Swollen Model

#### 4.5 Non-Scaffold Fixating Techniques - Conclusion

In light of the data presented in Tables 12 and 13, and particularly the data pertaining to the cartilage bone, we can draw comprehensive conclusions about the non-scaffold technique. It becomes clear that the single plating or single nailing technique is not feasible when there is no scaffold implant in the defect. Conversely, the double plating fixation approach is highly recommended and can ensure the patient's natural mobility.

Moreover, the combination of a plate and nailing system can also be viable in certain circumstances, albeit with some limitations on walking. It's also important to note that as the healing process progresses and the bone transitions into its immature form, it becomes less susceptible to mobility restrictions. At this later stage, all the different techniques examined could potentially be applied.

Table 14 Non-Scaffold Viable Fixating

Viable Fixating Techniques	Gait Load
Plate	25%
Retrograde Nailing	25%
Plate and Nailing	50%
Double Plate	Full

## 5. Design and Finite Element Analysis of Porous Scaffold Implant for Bone Defect Management

### 5.1 Unit Cell to Scaffold

In the following chapter of this dissertation, we turn our attention to the scenario of bone defect management involving the application of a porous scaffold within the defect gap, in conjunction with the previously discussed fixation techniques (namely, single plate, single nailing system, and a combination of plate and nail). A comprehensive discussion is required to determine the optimal scaffold design, taking into account factors such as unit cell geometry and size, thickness, and porosity. This chapter aims to shed light on these considerations and their implications for effective bone defect treatment.

In this segment of the chapter, we introduce the various types of unit cells utilized in the design of the scaffold. Initially, we attempted to tackle the challenge of unit cell design and scaffold creation using Solidworks software. However, we quickly realized that the process of creating a unit cell in Solidworks was not only complex but also time-consuming. Furthermore, generating the final scaffold proved to be an insurmountable task due to the software's limitations in handling such intricate structures.

The software that facilitated the creation of these unit cells and the scaffold as a whole was nTop Platform. nTop Platform is a cutting-edge computational software that enables engineers to design advanced and complex geometries, such as lattices and porous structures, with relative ease. It offers a high degree of control over the design parameters, allowing for the creation of structures that are tailored to specific applications.

One of the key advantages of nTop Platform is its ability to handle lattice structures, which are often used in the design of porous scaffolds. Lattice structures are geometric designs that consist of repeating units, or unit cells, which can be manipulated to control the properties of the overall structure. This is particularly useful in the design of porous scaffolds, where the size, shape, and arrangement of the pores can significantly influence the scaffold's mechanical properties and its interaction with biological tissues.

Furthermore, nTop Platform's robust computational capabilities allow for the efficient generation and manipulation of these complex structures, which can often be computationally intensive. This makes it an ideal tool for the design and optimization of porous scaffolds in bone defect treatment. In the following sections, we will delve into the specific unit cell designs that were utilized in this study.

These unit cells form the building blocks of the scaffold and play a crucial role in determining its overall mechanical properties and performance. Each unit cell type possesses unique characteristics and offers different advantages, making them suitable for specific applications. The choice of unit cell structure is a critical aspect of scaffold design and has a significant impact on the success of bone regeneration.

1. **Honeycomb Unit Cell:** The honeycomb structure is one of the most commonly used unit cells in scaffold design due to its high strength-to-weight ratio and anisotropic properties. This structure, as the name suggests, resembles the hexagonal pattern found in natural honeycombs. It provides excellent mechanical stability and has a high degree of porosity, making it ideal for promoting cell growth and nutrient diffusion.

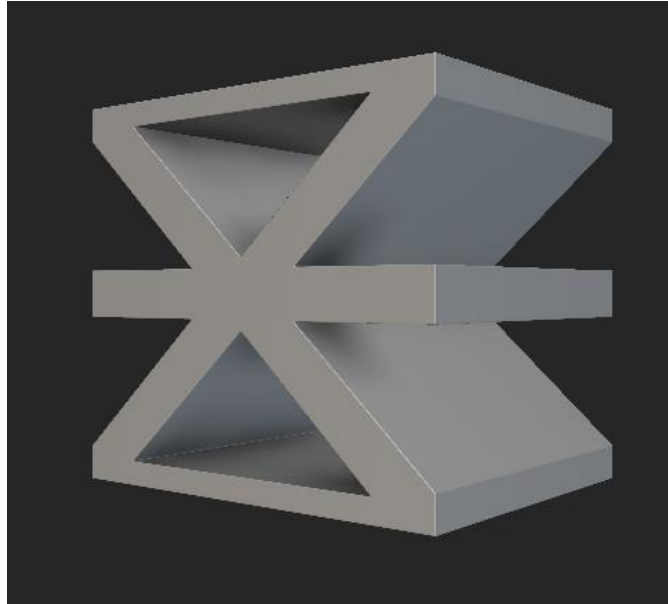


Figure 5.1 Honeycomb Unit Cell

2. **Diamond Unit Cell:** The diamond unit cell is characterized by its complex, interconnected lattice structure that resembles a diamond. This structure provides a high degree of isotropy, meaning it has uniform properties in all directions. The diamond unit cell is known for its excellent mechanical strength and durability, making it a suitable choice for load-bearing applications.

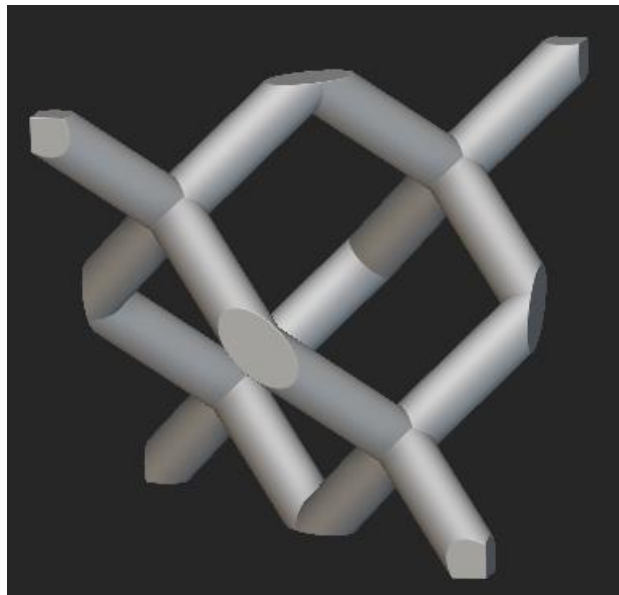


Figure 5.2 Diamond Unit Cell

3. **Voronoi Unit Cell:** The Voronoi unit cell is based on Voronoi tessellation, a mathematical concept where a plane is divided into regions based on distance to points in a specific subset of the plane. This results in a complex, irregular structure that closely mimics the random, porous structure of natural bone. The Voronoi unit cell is highly customizable and can be tailored to match the specific mechanical and biological requirements of the scaffold.

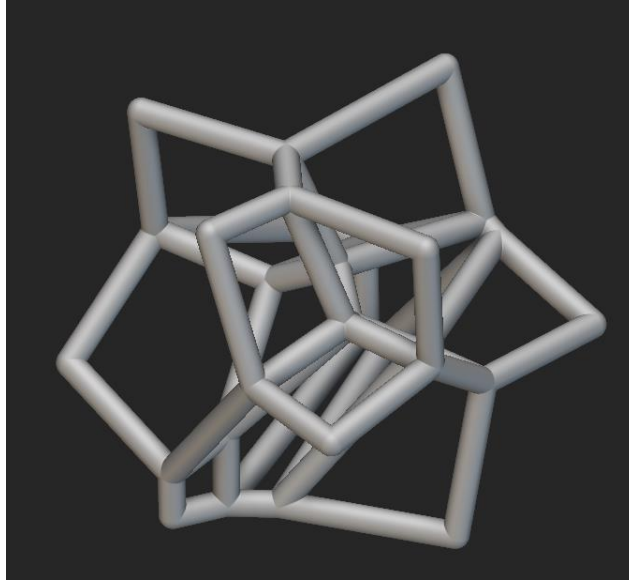


Figure 5.3 Voronoi Unit Cell

In our pursuit of the optimal scaffold design, we employed an iterative process of trial and error, adjusting the size and thickness of each unit cell to achieve the desired porosity. The aim was to create a scaffold that would promote the ideal strain environment for bone regeneration. This iterative process involved a continuous cycle of design modification, simulation, and evaluation, each time refining the scaffold parameters based on the results obtained.

After numerous iterations, we were able to determine the optimal structure parameters for each unit cell type. These parameters, which include the unit cell size, strut thickness, and overall porosity, were carefully calibrated to ensure that the resulting scaffold would provide the optimal mechanical environment for bone regeneration.

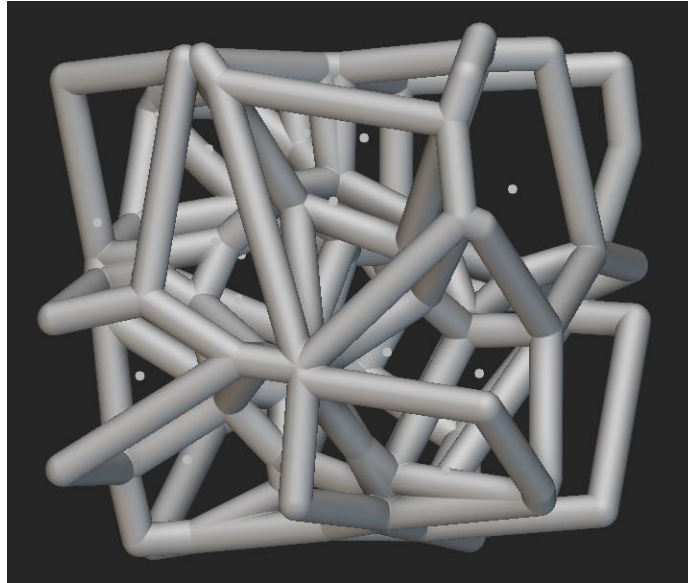
The specific parameters for each unit cell type are detailed in the following sections. These parameters represent the culmination of our iterative design process and reflect the optimal balance between mechanical performance and biological compatibility for each unit cell type.

Table 15 Final Unit Cells

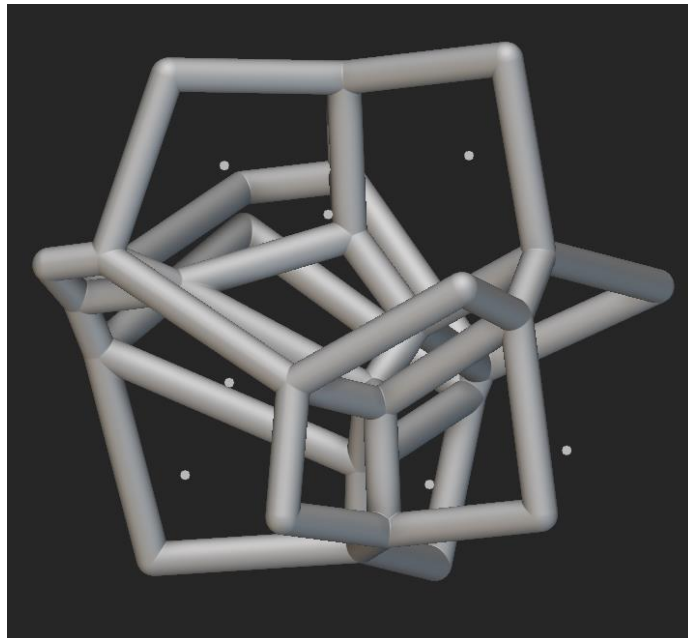
Unit Cell	Size (mm)	Thickness (mm)	Point Spacing (mm)
Honeycomb	2x2x2	0.25	-
Diamond	2x2x2	0.35	-
		0.25	-
Voronoi	2x2x2	0.2	1
		0.15	1.2

In the context of a Voronoi lattice, point spacing refers to the distance between the seed points that are used to generate the Voronoi diagram. These seed points are randomly distributed within a given space, and each point forms the nucleus of a cell in the Voronoi lattice. The boundaries of each cell are

determined by the midpoint between any two adjacent seed points. Therefore, the point spacing in a Voronoi lattice directly influences the size and shape of the cells within the lattice. A smaller point spacing results in smaller, more densely packed cells, while a larger point spacing results in larger, more loosely packed cells. This parameter is crucial in determining the overall structure and porosity of the Voronoi lattice, and thus plays a significant role in the mechanical properties of the resulting scaffold.



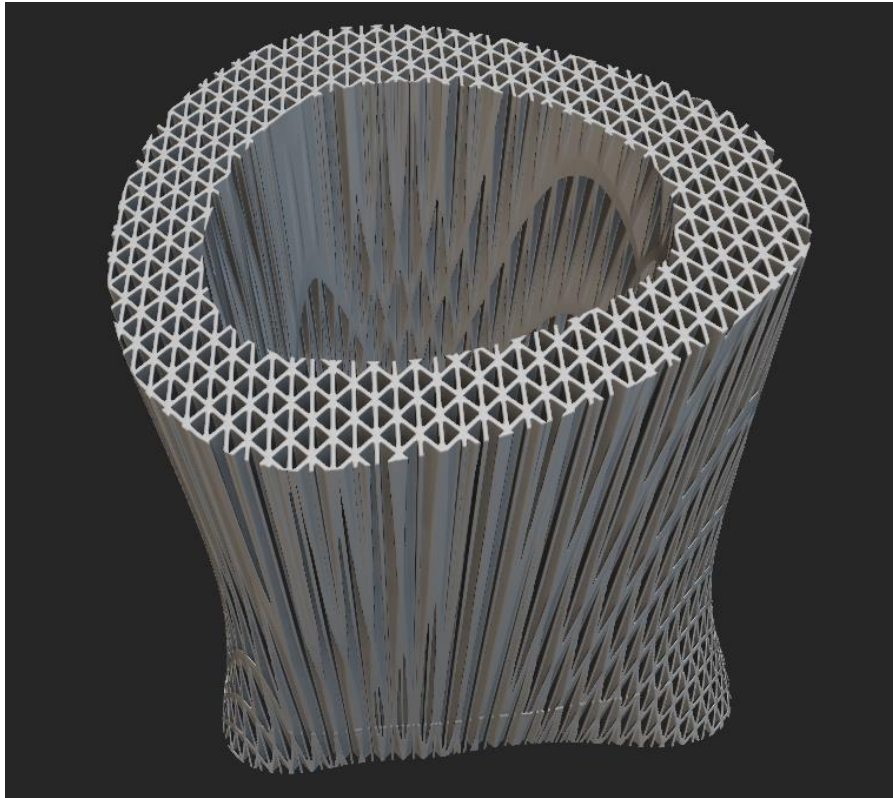
*Figure 5.4 Voronoi Unit Cell - 0.9 mm Point Spacing*



*Figure 5.5 Voronoi Unit Cell – 1.2 mm Point Spacing*

Indeed, as illustrated in the figures above, a larger point spacing value results in a less dense unit cell. This characteristic is crucial in tailoring the porosity and mechanical properties of the scaffold, allowing for the optimization of the scaffold design to meet specific requirements.

In the following section, we will showcase the final bone-shaped scaffolds that have been generated from each unit cell type listed in the previous table. These scaffolds were created using the nTop software, which allowed us to shape the unit cells into the form of the bone defect. This process involved manipulating the unit cells to conform to the specific dimensions and shape of the bone defect, resulting in a scaffold that closely mimics the structure of the missing bone segment. The images below provide a visual representation of these final bone-shaped scaffolds for each unit cell type.



*Figure 5.6 Honeycomb Final Scaffold*



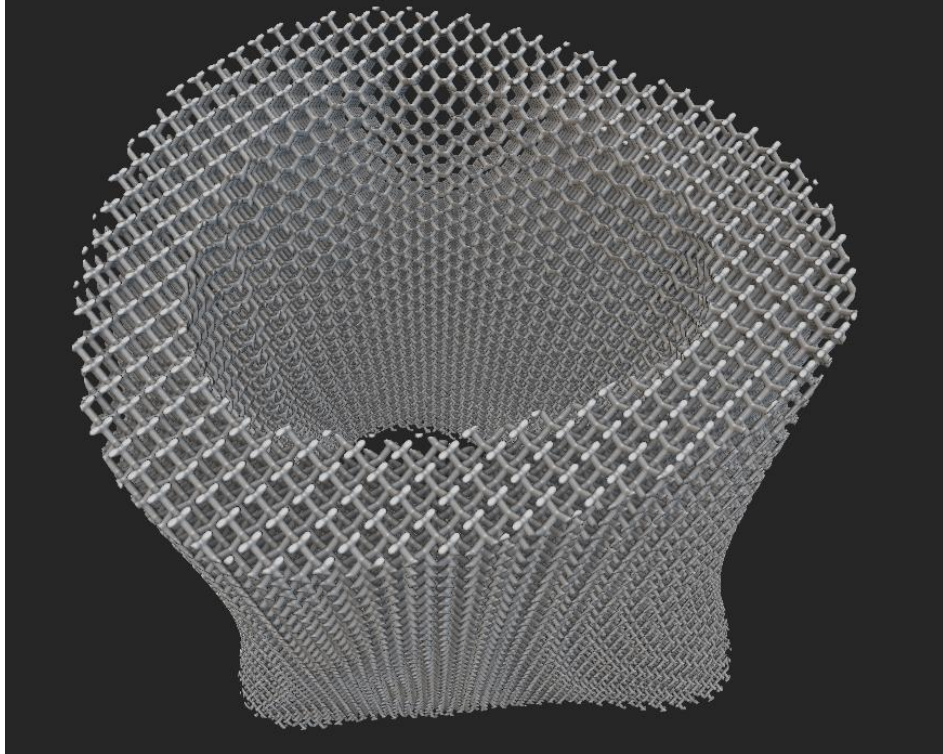


Figure 5.7 Diamond Scaffold - 0.35

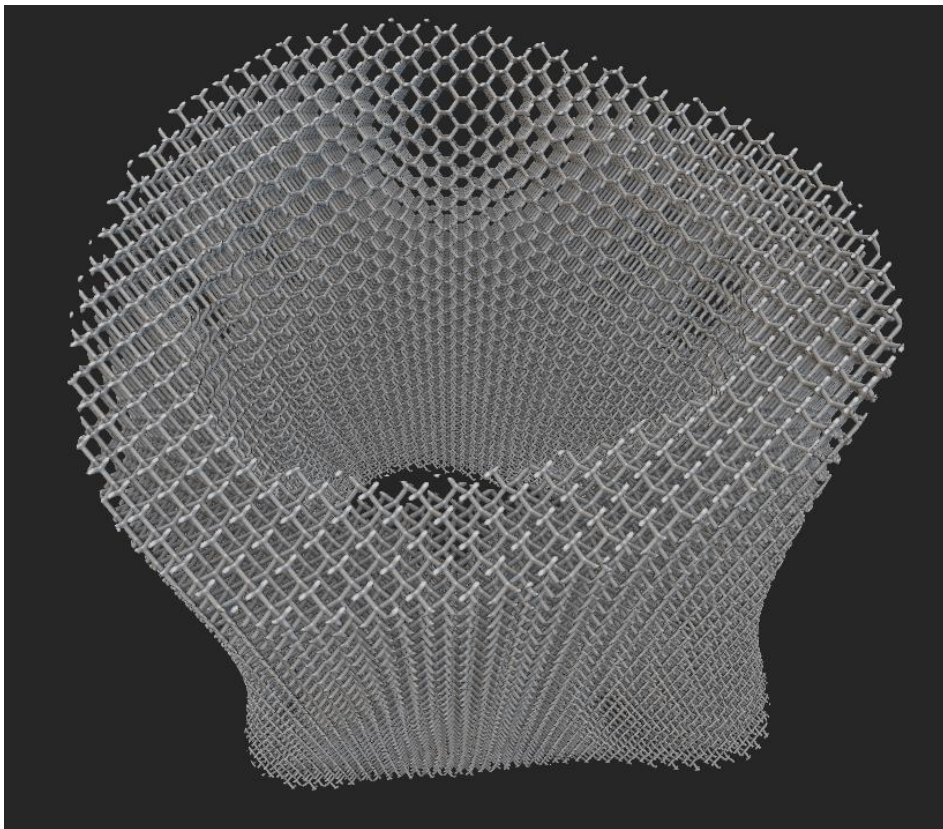
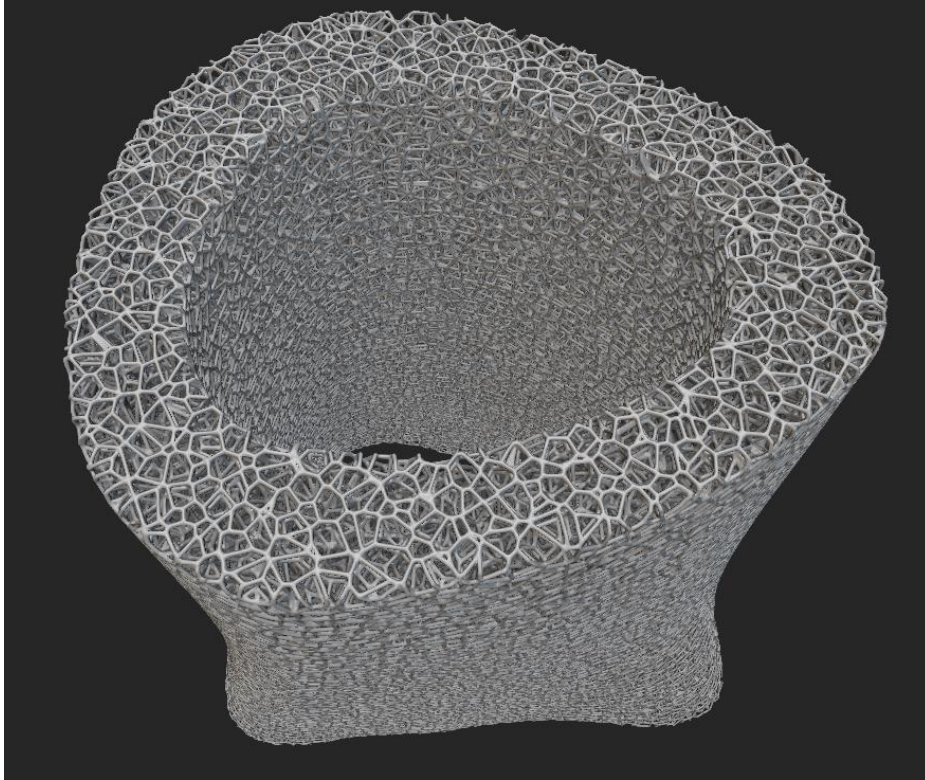
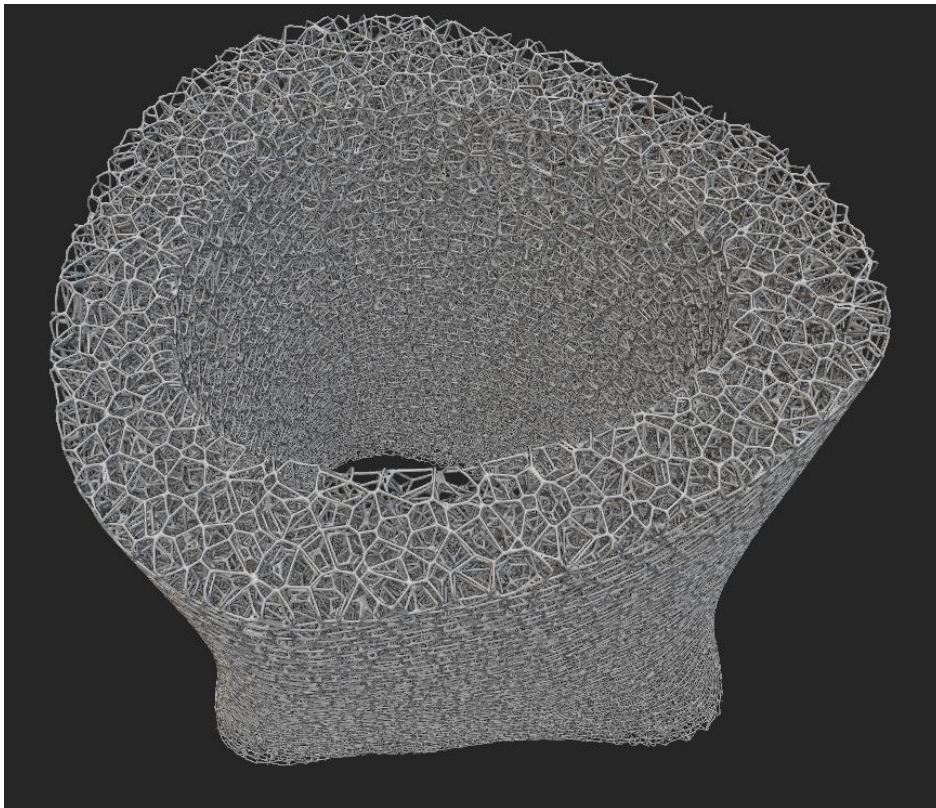


Figure 5.8 Diamond Scaffold - 0.25



*Figure 5.9 Voronoi Scaffold - 0.2 Thickness - 1 Point Spacing*



*Figure 5.10 Voronoi Scaffold - 0.15 Thickness – 1.2 Point Spacing*

In evaluating the final scaffolds created, several observations can be made. Firstly, the honeycomb structure appears unsuitable for scaffold implantation, as it does not adequately mimic the natural structure of bone. Its design, which allows for regeneration in only one axis, seems to limit the potential for comprehensive bone regeneration. Despite this initial impression, simulations will still be performed on the honeycomb scaffold to ensure the comprehensiveness of this thesis.

Conversely, the diamond structure appears to be a more viable option. As indicated in previous literature, this structure allows for bone regeneration in multiple directions, making it a more suitable choice for scaffold design.

However, the most promising scaffold appears to be the one resulting from the Voronoi structure. This structure closely resembles the natural structure of bone, which could potentially enhance the process of bone regeneration. The Voronoi structure's resemblance to natural bone structure, coupled with its allowance for multi-directional bone growth, makes it a strong candidate for optimal scaffold design.

## 5.2 Homogenization

In the following chapter, we focus into the process of material homogenization for the unit cells previously discussed. This step is crucial for our study as it allows us to assign effective mechanical properties to the complex structures of the unit cells, thereby simplifying the computational model for our simulations in ANSYS software.

Material homogenization is a technique used to approximate the mechanical behavior of complex structures, such as our unit cells, by assigning them an equivalent homogeneous material. This process significantly reduces the computational cost and complexity of our simulations, while still providing an accurate representation of the mechanical behavior of the porous scaffold.

There are two methods by which we performed material homogenization: one using ANSYS software, and the other using nTop software. Both of these methods will be thoroughly analyzed in the sections that follow.

### 5.2.1 ANSYS Homogenization

In the subsequent section, we concentrate on the homogenization process as performed in ANSYS software, specifically utilizing the Material Designer tool. The process begins with the importation of the unit cell geometry, which is in the .step format, exported from nTop software.

Within Material Designer, we select the 'User Defined' model type and after we switch to normal scale (mm), we proceed to input the .step file. Following this, we select our material, in this case, Ti6Al4V, which is imported from the engineering data. In the geometry section, we select the body of the unit cell and assign it with a name. This process allows us to define the material properties of the unit cell based on the selected material, Ti6Al4V, thereby enabling the homogenization of the unit cell's mechanical properties.

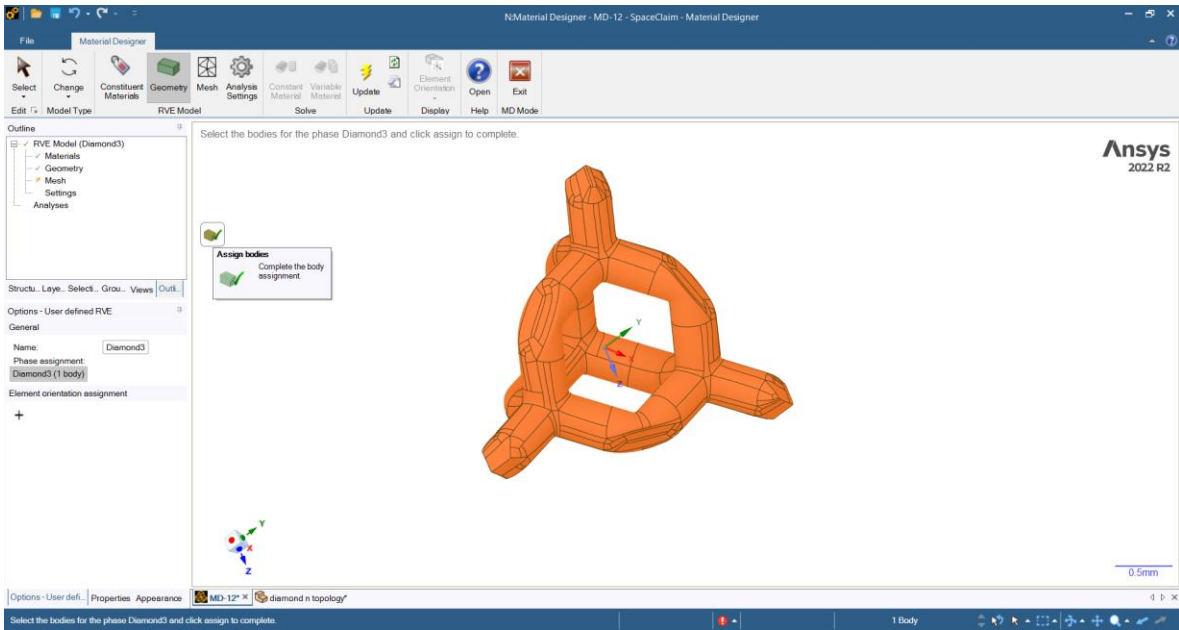


Figure 5.11 Material Designer Interface: Body and Material Assigning

Following the aforementioned steps, we are now prepared to mesh the unit cell. This is achieved by specifying certain parameters and setting a maximum mesh size. Subsequently, we define the settings for the homogenization process. We opt for the 'Constant Material Evaluation' and initiate the simulation. This process yields the necessary Young's modulus and Poisson's ratio for each direction, as well as the density of the final material. These values are critical as they represent the effective mechanical properties of the homogenized material, which are used in the subsequent finite element analysis in ANSYS [30].

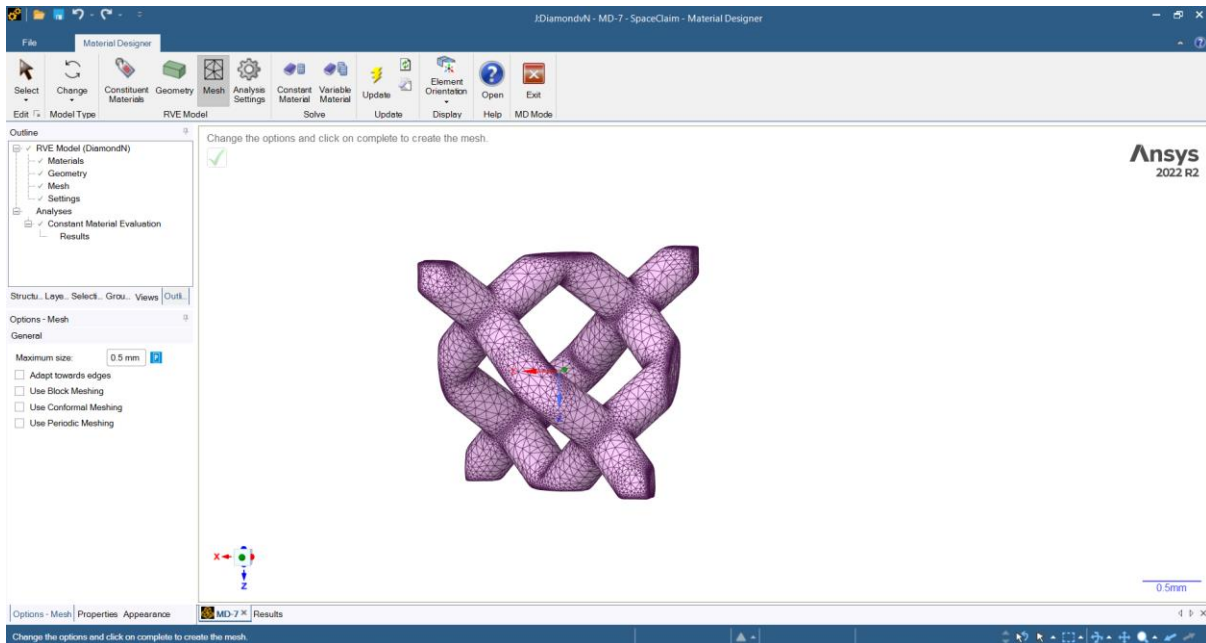

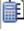


Figure 5.12 Meshing the Unit Cell

Table 16 Final Homogenization Results

	Name	Value	Unit	P
<b>Engineering Constant</b>				
	E1	1.4851E+09	Pa	<input type="checkbox"/>
	E2	1.4684E+09	Pa	<input type="checkbox"/>
	E3	1.4745E+09	Pa	<input type="checkbox"/>
	G12	1.3126E+09	Pa	<input type="checkbox"/>
	G23	1.3224E+09	Pa	<input type="checkbox"/>
	G31	1.3141E+09	Pa	<input type="checkbox"/>
	nu12	0.4211		<input type="checkbox"/>
	nu13	0.41954		<input type="checkbox"/>
	nu23	0.42345		<input type="checkbox"/>
<b>Density</b>				
	rho	738.64	kg m <sup>-3</sup>	<input type="checkbox"/>
<b>Logs</b>				
	RVE log			
	Solver logs			

### 5.2.2 nTop Homogenization

In the next phase of our study, we turn our attention to the homogenization process within the nTop platform. To create our unit cell, we utilize the appropriate volume lattice block. For the Honeycomb and Diamond Unit Cells, we use the Rectangular Volume Lattice, while for the Voronoi unit cell, we employ the Voronoi Volume Lattice.

For the Voronoi unit cell, it is necessary to incorporate a Random Seed Points block and a Mesh Box of the Boundary of the unit cell. This allows us to generate the Voronoi Unit Cell effectively. Following this, we proceed to mesh the desired unit cell using the Mesh from Implicit Body block.

To create the Finite Element Mesh of the Unit Cell, we utilize the FE Volume Mesh block, selecting a quadratic geometric order. This process enables us to accurately represent the complex geometry of the unit cell and is a crucial step in preparing for the subsequent simulation within ANSYS.

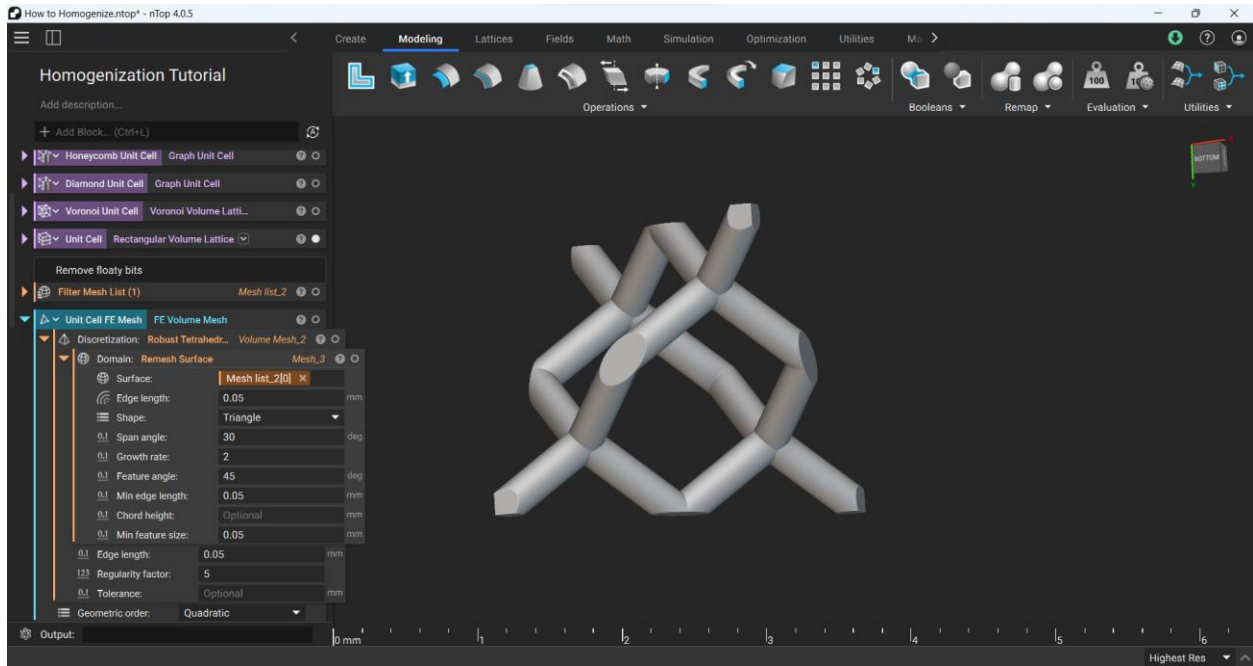


Figure 5.13 Creating FE Mesh of Unit Cell

In the subsequent step of our process, we utilize the Homogenization Unit Cell block, importing the Finite Element Mesh that we previously created. By specifying the material and the design volume, we are able to prepare the simulation for execution.

The figures below provide a visual representation of the homogenized unit cells, illustrating the displacement that occurs within each cell. Additionally, we present the results for the directional Young's modulus.

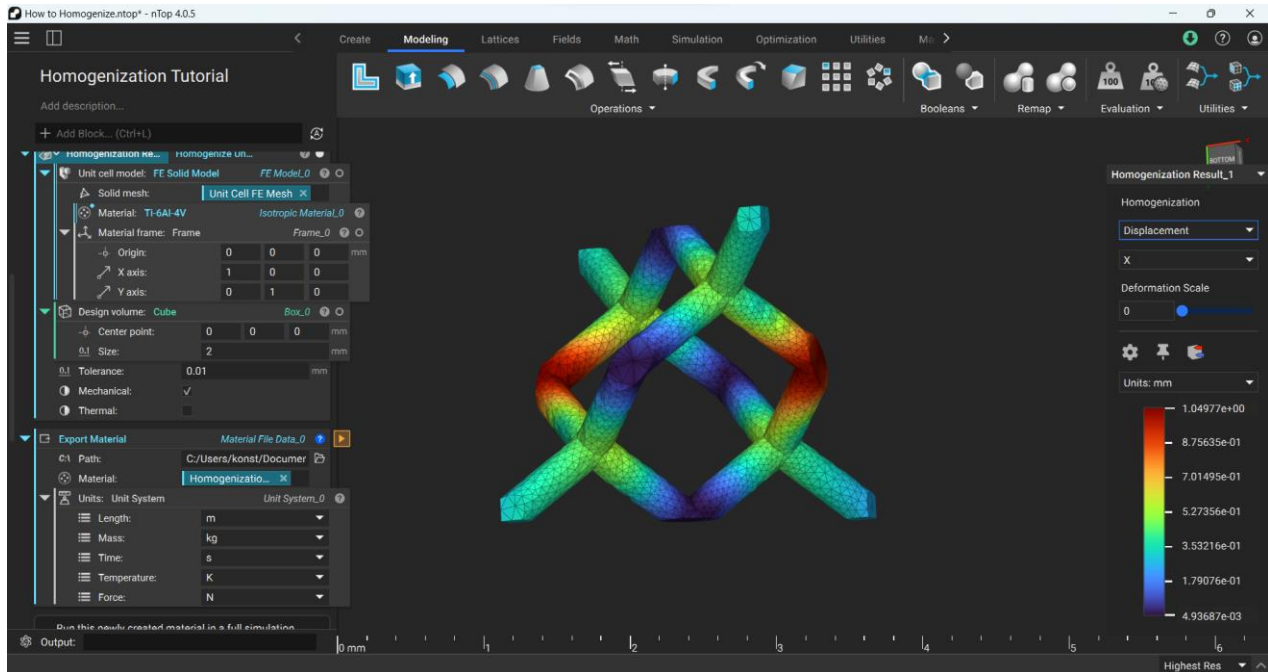


Figure 5.14 Diamond Unit Cell X-Axis Displacement

The directional Young's modulus, also known as the modulus of elasticity, is a measure of a material's ability to deform elastically (i.e., non-permanently) when a force is applied to it. It is defined as the ratio of stress (force per unit area) to strain (proportional deformation) in a material. In the context of unit cells in a scaffold, the directional Young's modulus is particularly important as it provides insights into how the material will behave under different loading conditions in different directions.

In an isotropic material, the Young's modulus is the same in all directions. However, in anisotropic materials, such as the unit cells in our scaffold, the Young's modulus can vary depending on the direction of the applied load. This directional dependence is a crucial factor in the design of the scaffold, as it influences the overall mechanical behavior of the implant. Understanding the directional Young's modulus allows us to predict and control the deformation behavior of the scaffold under physiological loading conditions, thereby optimizing its performance for bone regeneration.

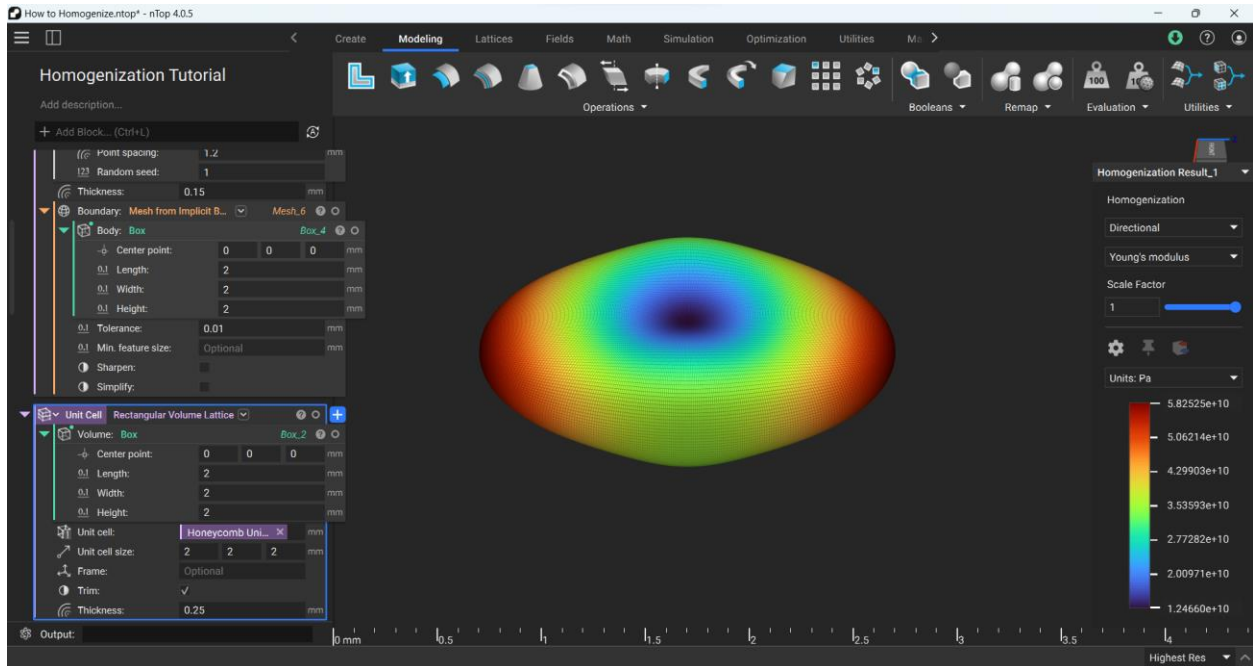


Figure 5.15 Directional Young's Modulus of Honeycomb Unit Cell

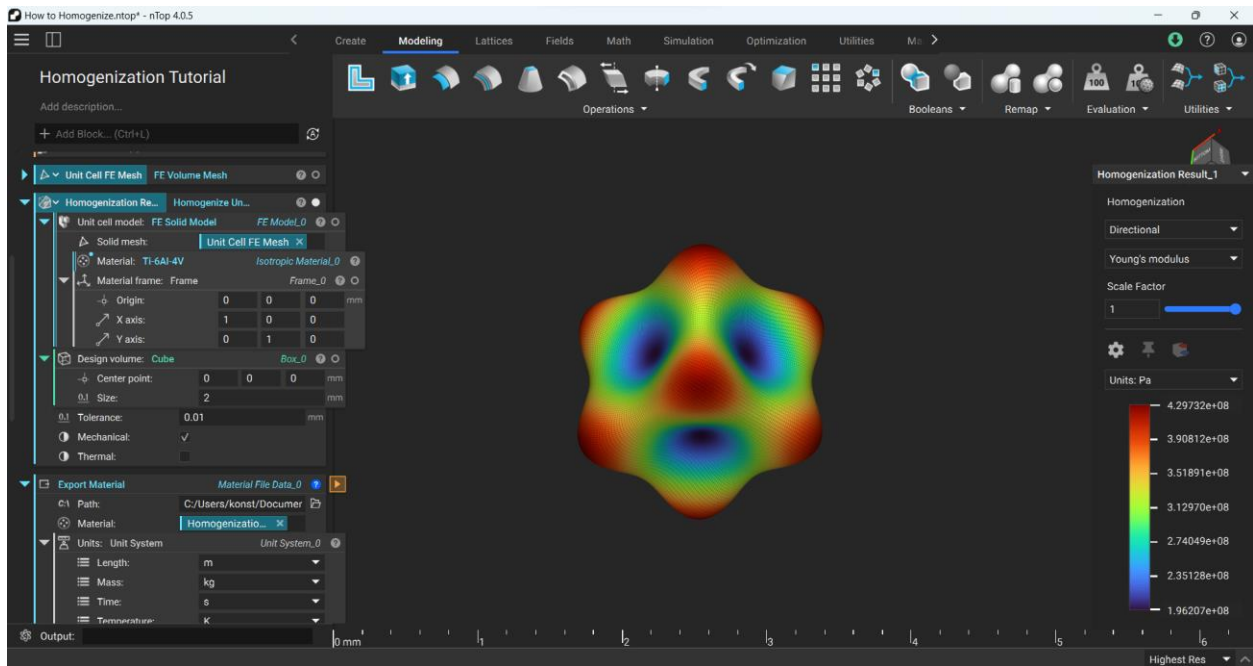


Figure 5.16 Directional Young's Modulus of Diamond Unit Cell



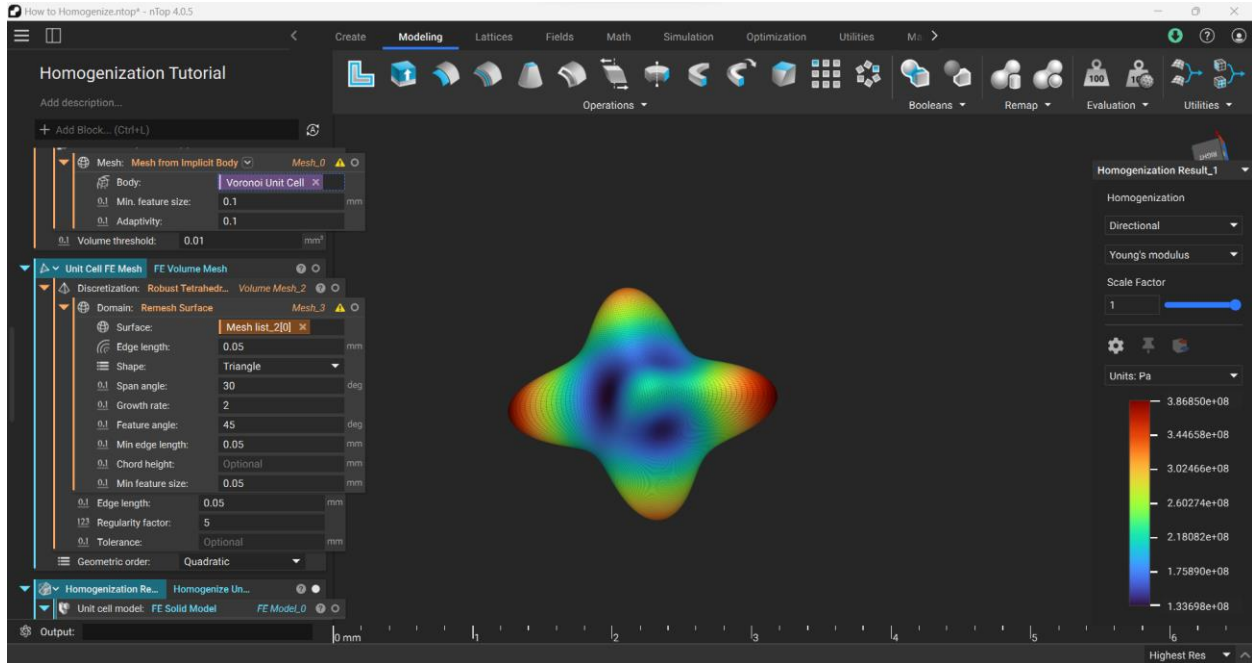


Figure 5.17 Directional Young's Modulus of Voronoi Unit Cell

In the next phase of the process, once the homogenization simulation has been completed, we are able to export the material properties directly from nTop. This is achieved using the 'Export Material' block. This function allows us to export the anisotropic elasticity table, which provides a comprehensive overview of the material's elastic properties in different directions. Alongside this, the density corresponding to the homogenized material is also exported. These exported properties can then be seamlessly imported into ANSYS software, where they are recognized as a new material. This new material, complete with its unique properties, is then ready to be applied in our subsequent simulations.

Table 17 ANSYS Interface: Anisotropic Elasticity Matrix of Diamond Unit Cell

DiamondFinal: Elasticity					
Options					
D[*],1 [M Pa]	D[*],2 [M Pa]	D[*],3 [M Pa]	D[*],4 [M Pa]	D[*],5 [M Pa]	D[*],6 [M Pa]
397	258	253	-1.82	0.62585	2.86
258	399	256	-2.32	3.98	-0.033155
253	256	395	-1.26	3.7	2.31
-1.82	-2.32	-1.26	170	1.31	0.45653
0.62585	3.98	3.7	1.31	168	1.31
2.86	-0.033155	2.31	0.45653	1.31	166

Upon completion of the homogenization process, it is essential to evaluate and compare the two methods employed. The nTop approach appears to be more efficient, faster, and more precise compared to the Ansys Software method. One of the primary reasons for this is the fact that the unit cells are generated directly within nTop, eliminating the need to export them as .step files and subsequently import them into another software. This not only saves time but also enhances the accuracy of the process, as it avoids potential errors or inconsistencies that may arise during the file conversion and transfer process. Therefore, for these reasons, the nTop method is deemed to be the more effective approach for this particular application.

### 5.3 Strain Analysis Based on Scaffold Design Variations

In the ensuing chapter, we perform the final simulations for the selected unit cells previously discussed. The primary objective of these simulations is to ascertain the strain patterns at the interface between the scaffold and the healthy bone. This critical analysis will allow us to determine which scaffold designs are most conducive to bone regeneration in the context of a bone defect. We will conduct these simulations for each fixation method, thereby providing a comprehensive overview of the most effective strategies for managing bone defects. This chapter is pivotal in our quest to identify the optimal scaffold and fixation combination to facilitate successful bone healing and restoration of function.

#### 5.3.1 Single Plating Technique

##### D: Plate Honeycomb Titanium

Equivalent Elastic Strain 2

Type: Equivalent Elastic Strain

Unit: mm/mm

Time: 1 s

04/07/2023 00:12

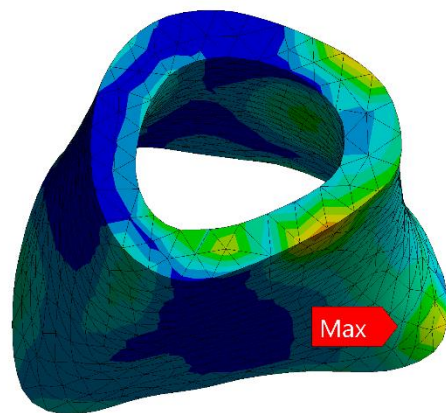
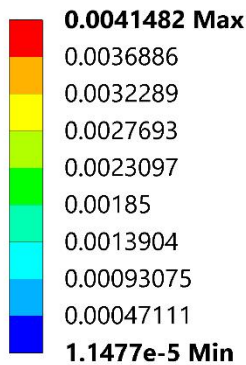


Figure 5.18 Plate Honeycomb - Strains Developed Upper Side

**D: Plate Honeycomb Titanium**

Equivalent Elastic Strain 2

Type: Equivalent Elastic Strain

Unit: mm/mm

Time: 1 s

04/07/2023 17:39

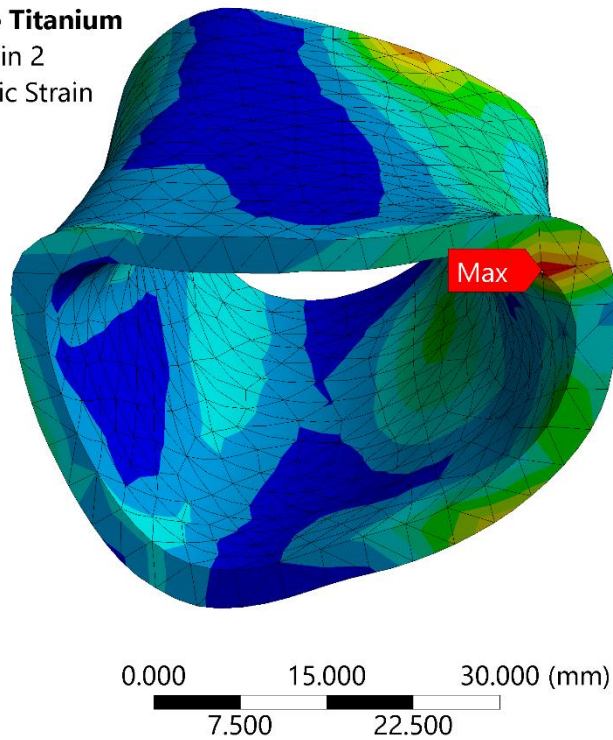
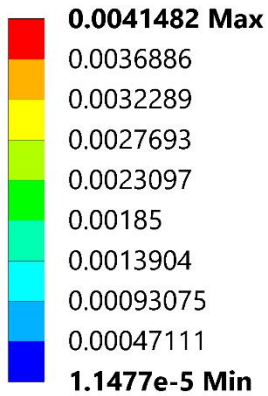


Figure 5.19 Plate Honeycomb - Strains Developed Lower Side

As anticipated, the strain values for the honeycomb scaffold, as depicted in the above figure, fall significantly below the optimal range. This outcome confirms our initial assessment that the honeycomb scaffold may not be the most suitable choice for our purposes. Therefore, in the interest of focusing on the most promising solutions, we will not include further simulations involving the honeycomb scaffold in the subsequent sections of this thesis.

**G: Plate Diamond1st**

Equivalent Elastic Strain  
Type: Equivalent Elastic Strain  
Unit: mm/mm  
Time: 1 s  
04/07/2023 00:22

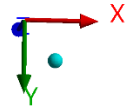
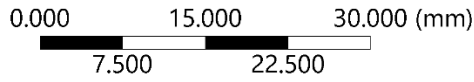
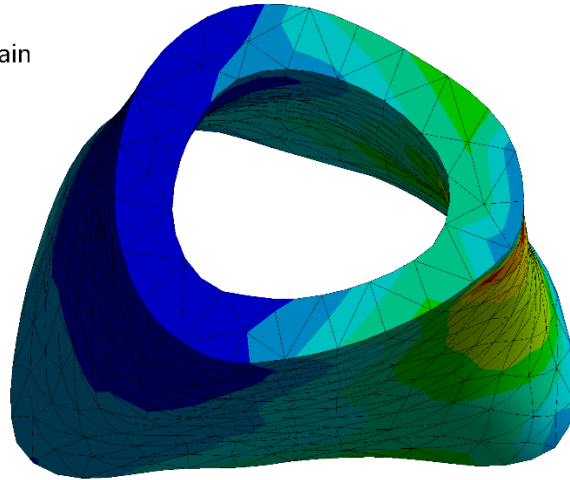
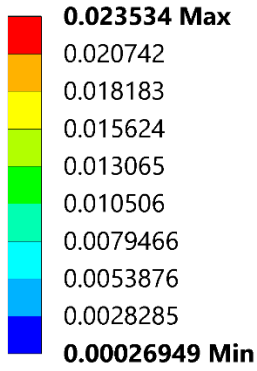


Figure 5.20 Plate Diamond 0.35 – Upper Side

**G: Plate Diamond1st**

Equivalent Elastic Strain  
Type: Equivalent Elastic Strain  
Unit: mm/mm  
Time: 1 s  
04/07/2023 00:21

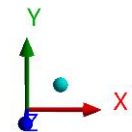
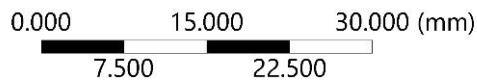
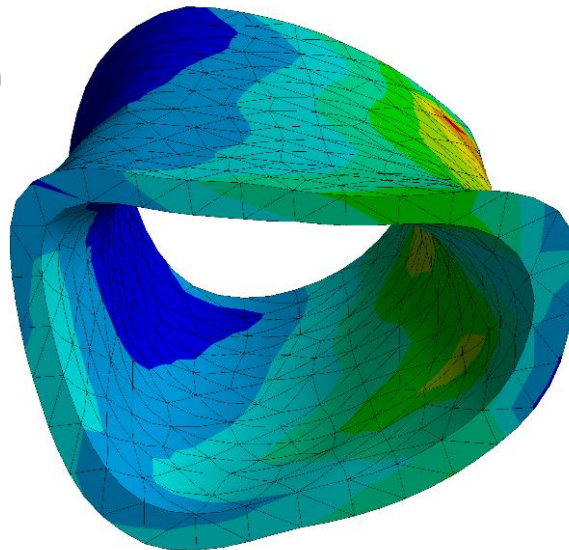
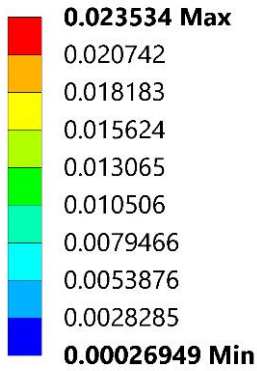


Figure 5.21 Plate Diamond 0.35 - Lower Side

**H: Plate DiamondFinal**

Equivalent Elastic Strain 2  
Type: Equivalent Elastic Strain  
Unit: mm/mm  
Time: 1 s  
04/07/2023 00:03

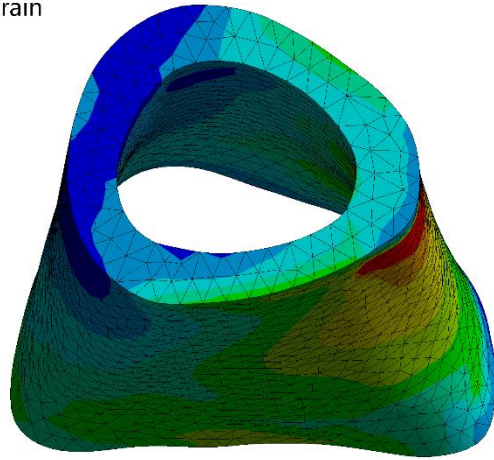
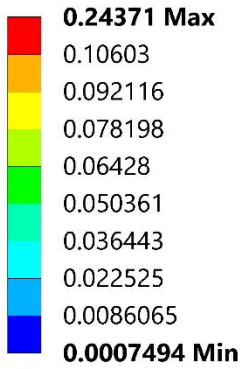


Figure 5.22 Plate Diamond 0.25 – Upper Side

**H: Plate DiamondFinal**

Equivalent Elastic Strain 2  
Type: Equivalent Elastic Strain  
Unit: mm/mm  
Time: 1 s  
04/07/2023 00:04

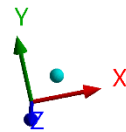
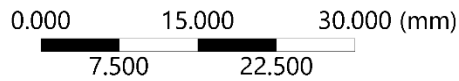
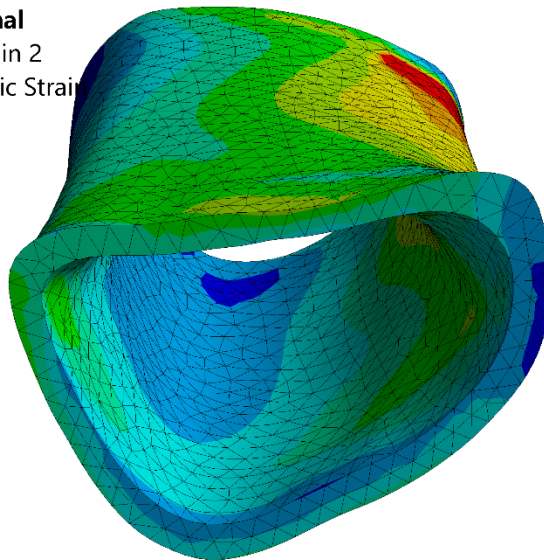
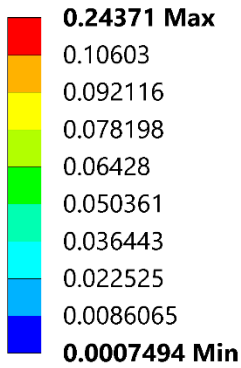


Figure 5.23 Plate Diamond 0.25 - Lower Side

**G: Plate Voronoi1st**

Equivalent Elastic Strain

Type: Equivalent Elastic Strain

Unit: mm/mm

Time: 1 s

04/07/2023 02:04

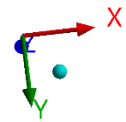
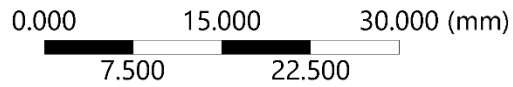
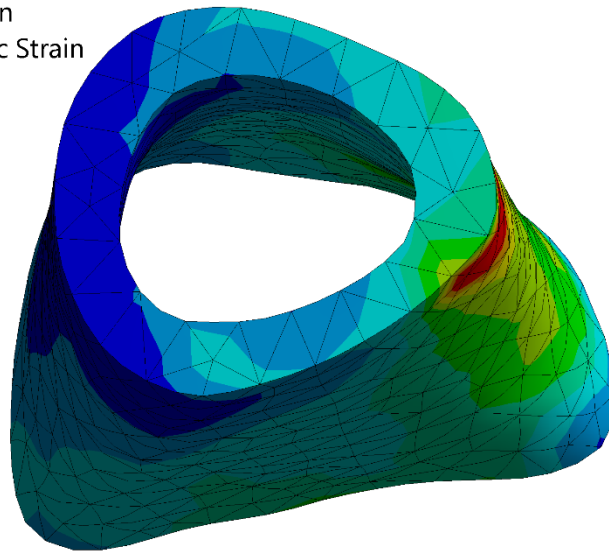
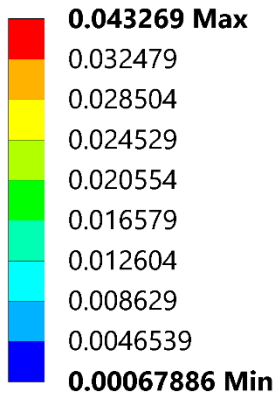


Figure 5.24 Plate Voronoi 0.2 – Upper Side

**G: Plate Voronoi1st**

Equivalent Elastic Strain

Type: Equivalent Elastic Strain

Unit: mm/mm

Time: 1 s

04/07/2023 02:05

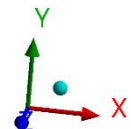
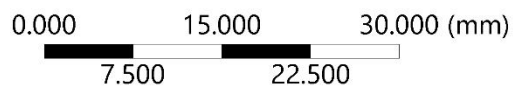
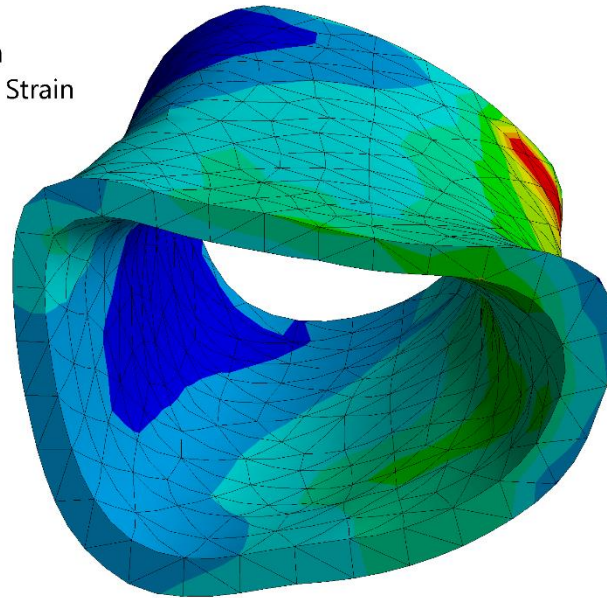
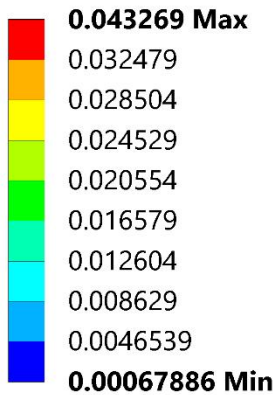


Figure 5.25 Plate Voronoi 0.2 – Lower Side

**I: Plate Voronoi**

Equivalent Elastic Strain 2  
Type: Equivalent Elastic Strain  
Unit: mm/mm  
Time: 1 s  
04/07/2023 00:25

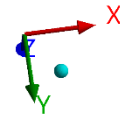
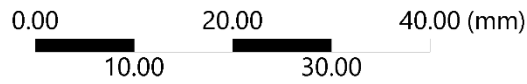
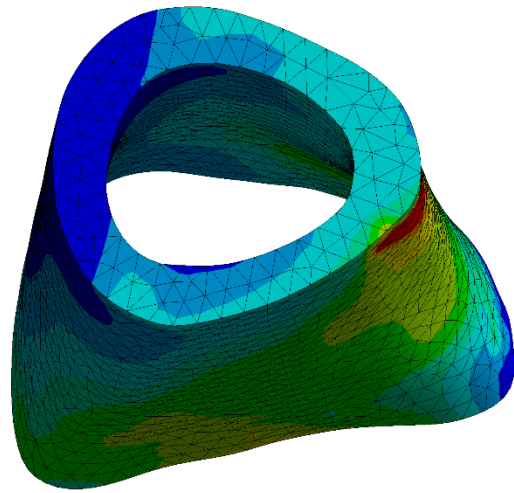
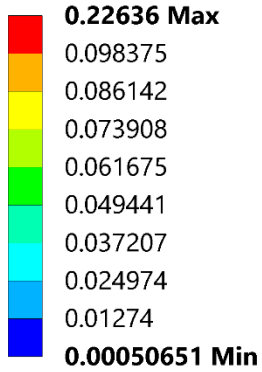


Figure 5.26 Plate Voronoi 0.15 – Upper Side

**I: Plate Voronoi**

Equivalent Elastic Strain 2  
Type: Equivalent Elastic Strain  
Unit: mm/mm  
Time: 1 s  
04/07/2023 00:26

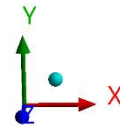
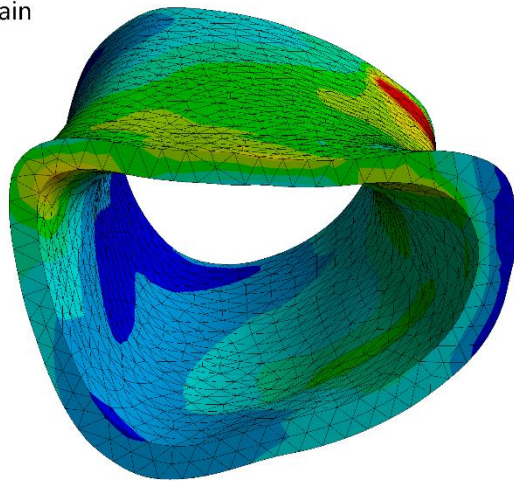
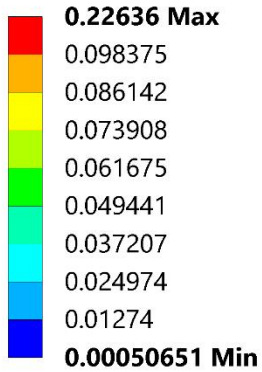


Figure 5.27 Plate Voronoi 0.15 – Lower Side

5.3.2 Single Nailing Technique

**L: Retrograde Diamond**

Equivalent Elastic Strain 2  
 Type: Equivalent Elastic Strain  
 Unit: mm/mm  
 Time: 1 s  
 04/07/2023 00:42

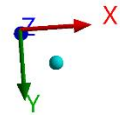
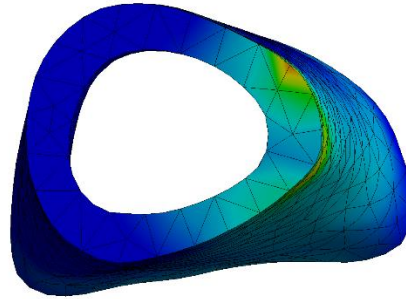
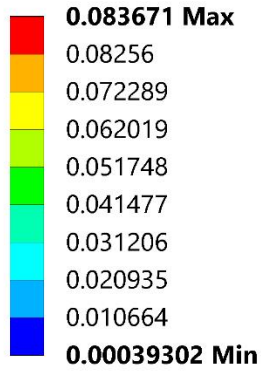


Figure 5.28 Nail Diamond 0.35 – Upper Side

**L: Retrograde Diamond**

Equivalent Elastic Strain 2  
 Type: Equivalent Elastic Strain  
 Unit: mm/mm  
 Time: 1 s  
 04/07/2023 00:42

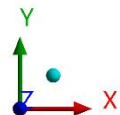
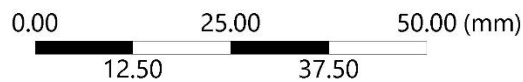
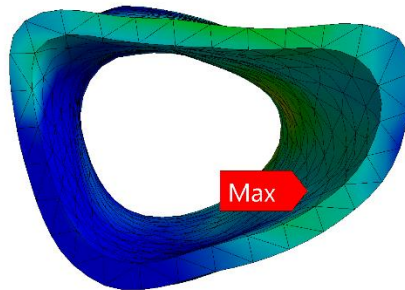
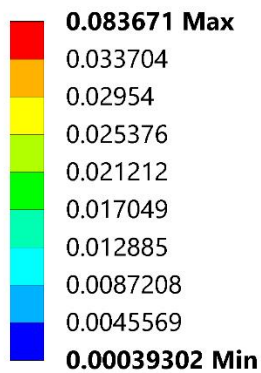


Figure 5.29 Nail Diamond 0.35 – Lower Side



**L: Retrograde Voronoi**

Equivalent Elastic Strain 2

Type: Equivalent Elastic Strain

Unit: mm/mm

Time: 1 s

10/07/2023 01:22

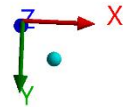
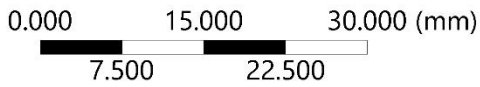
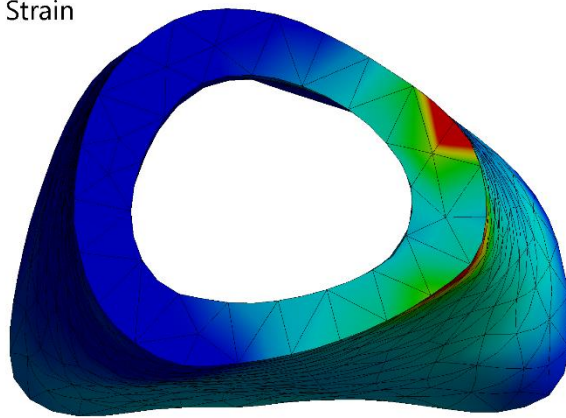
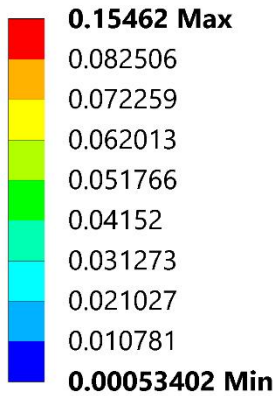


Figure 5.30 Nail Voronoi 0.2 – Upper Side

**L: Retrograde Voronoi**

Equivalent Elastic Strain 2

Type: Equivalent Elastic Strain

Unit: mm/mm

Time: 1 s

10/07/2023 01:21

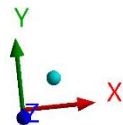
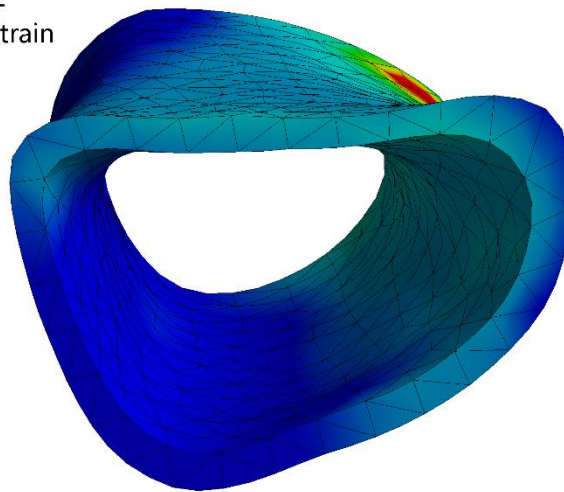
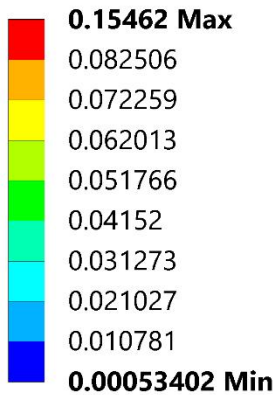


Figure 5.31 Nail Voronoi 0.2 – Lower Side

In our simulations, it is noteworthy that the retrograde intramedullary nailing method of fixation does not converge to a solution when applied to the thinner thickness diamond and Voronoi scaffolds. This observation suggests that the pairing of the single nailing technique with these particular scaffold designs may not be a feasible option. We will delve deeper into this matter and present more comprehensive conclusions at the end of this chapter.

### 5.3.3 Plate and Nail Technique

#### R: Plate and Retro Diamondv4

Equivalent Elastic Strain 2

Type: Equivalent Elastic Strain

Unit: mm/mm

Time: 1 s

04/07/2023 01:20

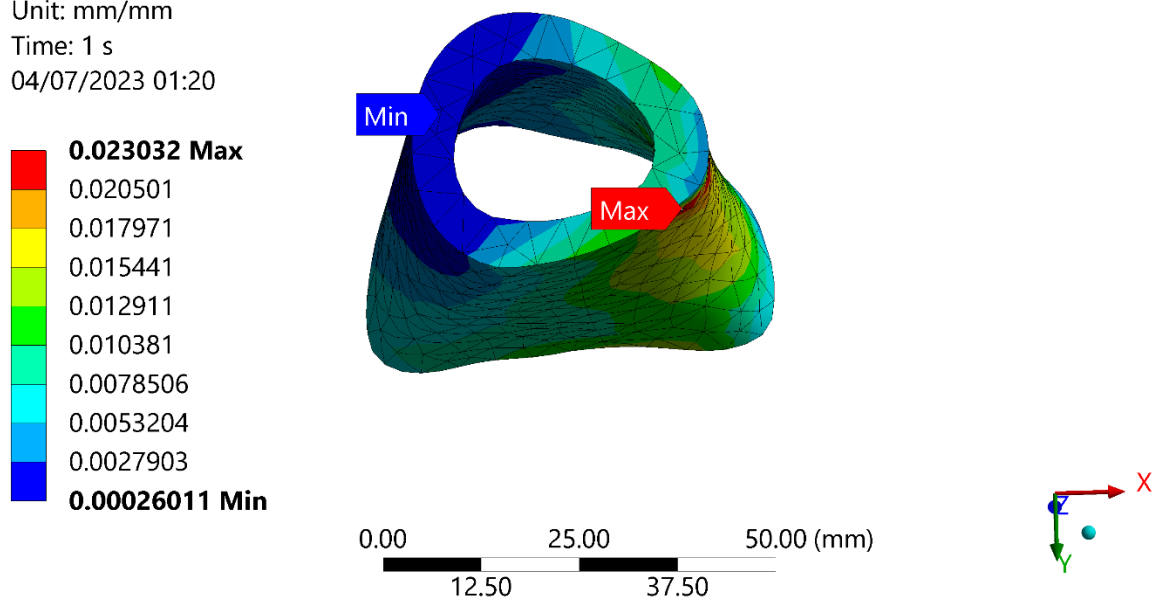


Figure 5.32 Plate&Nail Diamond 0.35 – Upper Side

**R: Plate and Retro Diamondv4**

Equivalent Elastic Strain 2

Type: Equivalent Elastic Strain

Unit: mm/mm

Time: 1 s

04/07/2023 01:20

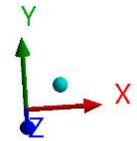
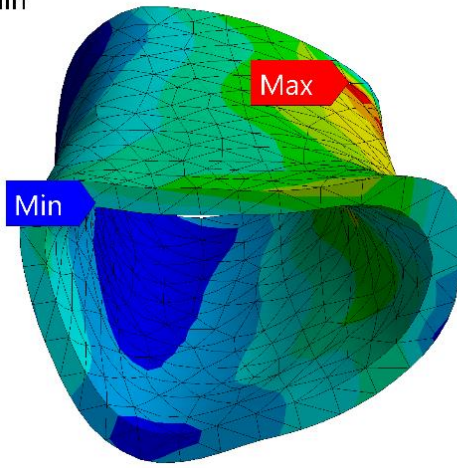
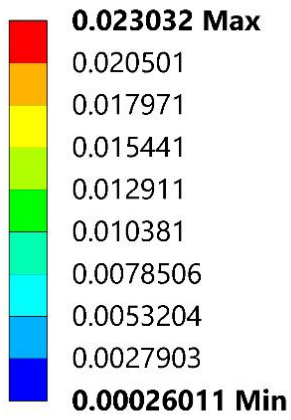


Figure 5.33 Plate&Nail Diamond 0.35 – Lower Side

**Q: Plate and Retro DiamondFinal**

Equivalent Elastic Strain 2  
Type: Equivalent Elastic Strain  
Unit: mm/mm  
Time: 1 s  
04/07/2023 00:40

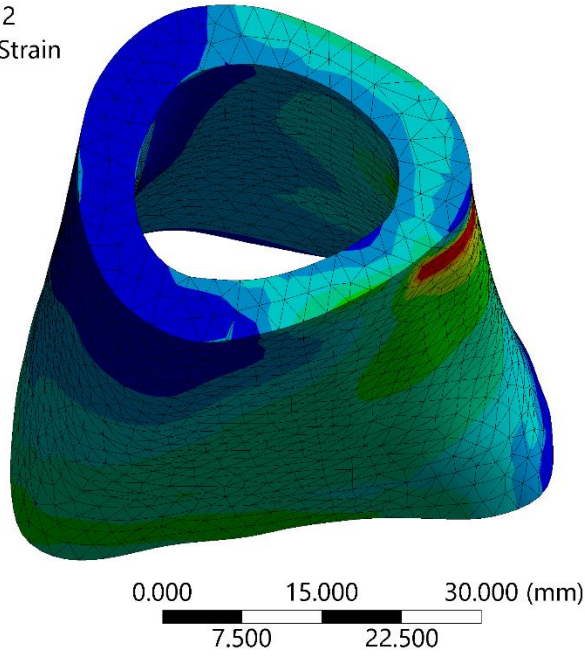
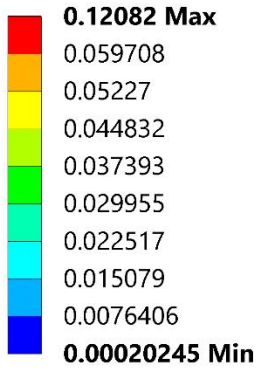


Figure 5.34 Plate&Nail Diamond 0.25 – Upper Side

**Q: Plate and Retro DiamondFinal**

Equivalent Elastic Strain 2  
Type: Equivalent Elastic Strain  
Unit: mm/mm  
Time: 1 s  
04/07/2023 00:39

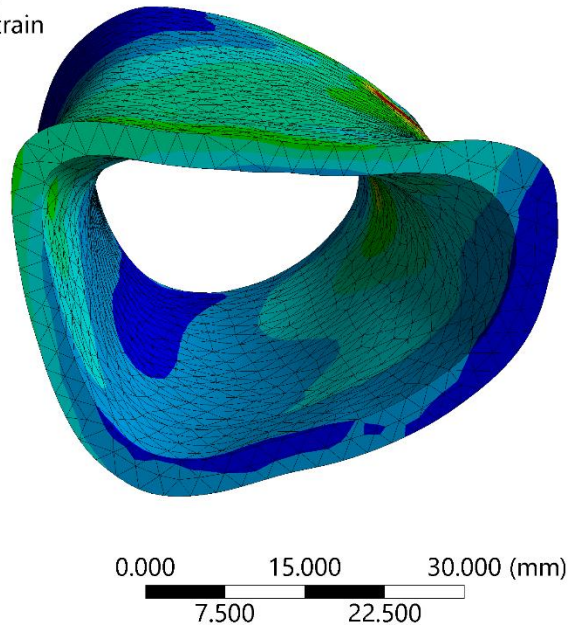
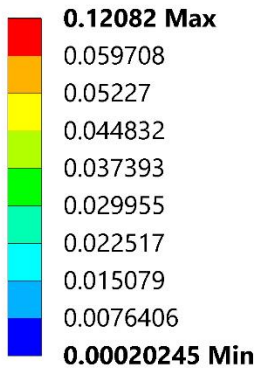


Figure 5.35 Plate&Nail Diamond 0.25 – Lower Side

**R: Plate and Retro Voronoi**

Equivalent Elastic Strain 2  
Type: Equivalent Elastic Strain  
Unit: mm/mm  
Time: 1 s  
04/07/2023 01:53

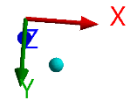
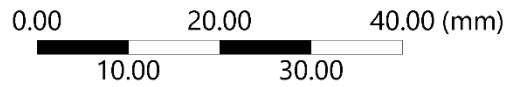
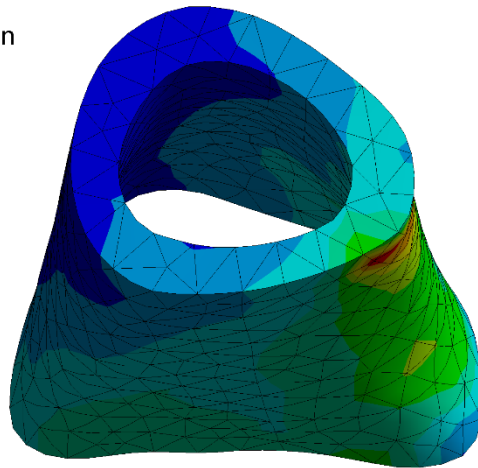
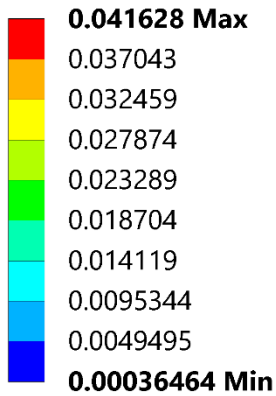


Figure 5.36 Plate&Nail Voronoi 0.2 – Upper Side

**R: Plate and Retro Voronoi**

Equivalent Elastic Strain 2  
Type: Equivalent Elastic Strain  
Unit: mm/mm  
Time: 1 s  
04/07/2023 01:52

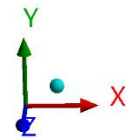
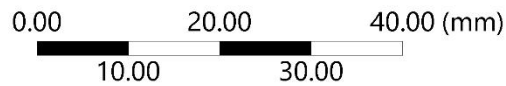
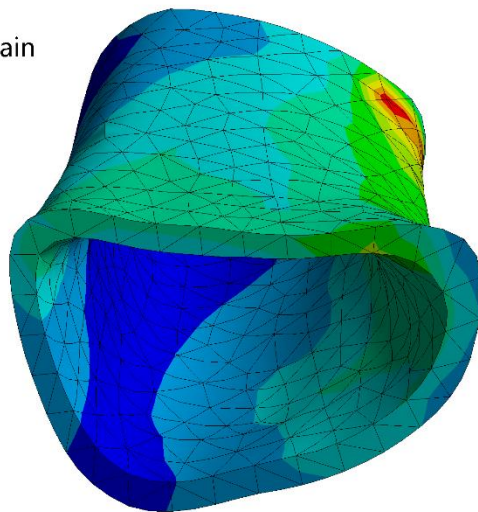
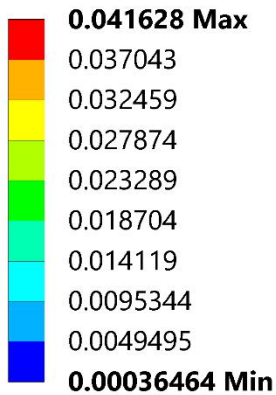


Figure 5.37 Plate&Nail Voronoi 0.2 – Lower Side

**R: Plate and Retro Voronoi**

Equivalent Elastic Strain 2

Type: Equivalent Elastic Strain

Unit: mm/mm

Time: 1 s

04/07/2023 01:46

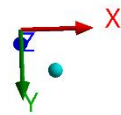
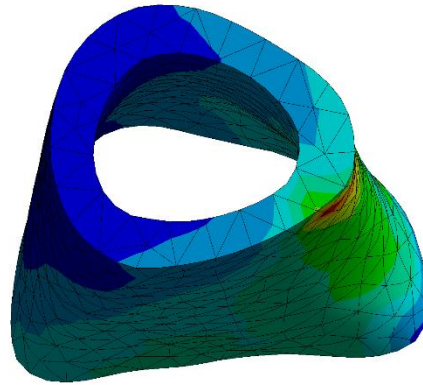
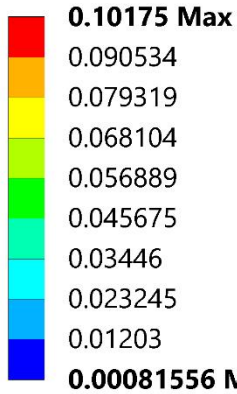


Figure 5.38 Plate&Nail Voronoi 0.15 – Upper Side

**R: Plate and Retro Voronoi**

Equivalent Elastic Strain 2

Type: Equivalent Elastic Strain

Unit: mm/mm

Time: 1 s

04/07/2023 01:46

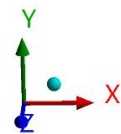
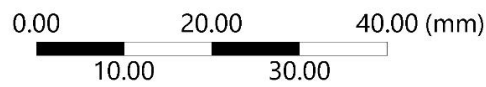
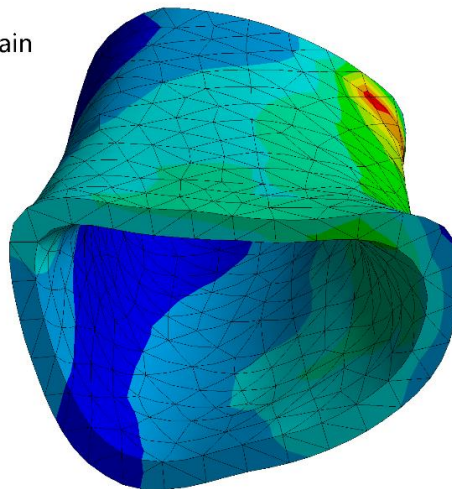
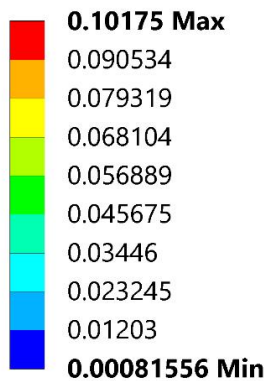


Figure 5.39 Plate&Nail Voronoi 0.15 – Lower Side

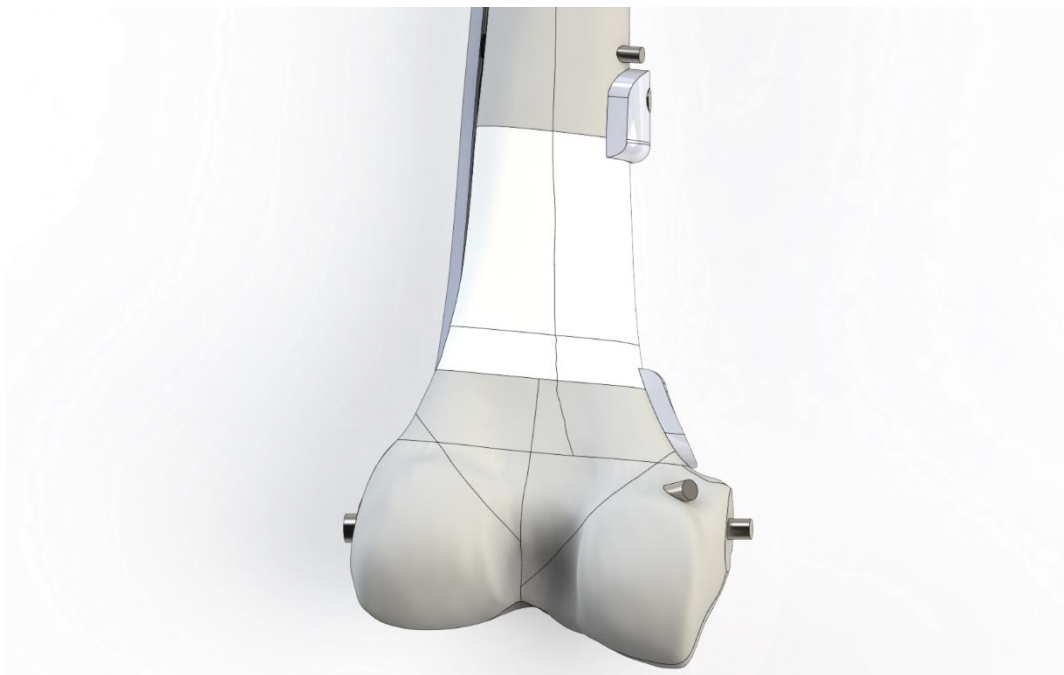
Following the presentation of all the figures for each method, it is important to note that we will be drawing conclusions regarding the simulation results and determining the optimal scaffold design for each case at the end of this chapter. This will allow us to consider all the data and findings in a comprehensive manner, ensuring a thorough and well-informed analysis.

#### 5.4 Testing Method on C3 Fractures

In the following chapter, we extend our investigation to a more complex scenario, incorporating a C3 fracture into our model in conjunction with the existing distal femur bone defect. This allows us to evaluate the performance of our scaffold design under more challenging conditions, and to assess the impact of such a fracture on the strain distribution at the interface between the scaffold and the bone.

To simulate this scenario, we modified our existing assembly to include three fractures at the lower end of the distal femur, effectively replicating a C3 fracture pattern. The modified assembly, illustrating the location and orientation of the fractures, is depicted in the figure below.

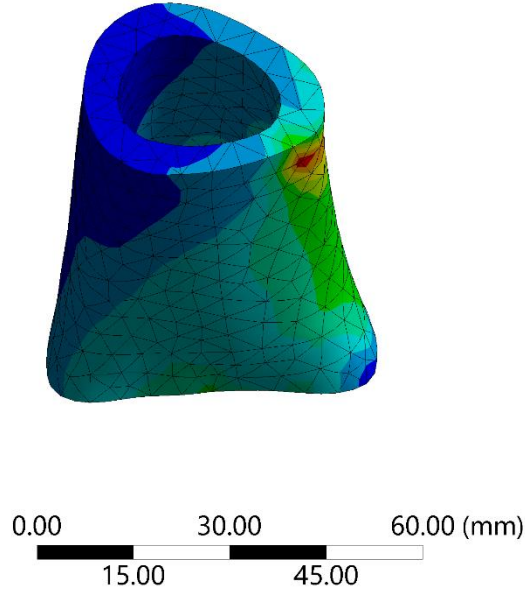
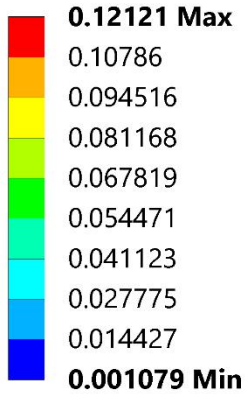
By comparing the results of this simulation with those obtained for the bone defect alone, we aim to identify any significant deviations that might influence the effectiveness of our scaffold design in promoting bone regeneration. This analysis will provide valuable insights into the adaptability of our design to different clinical scenarios, thereby enhancing its potential applicability in the treatment of complex bone defects.



*Figure 5.40 C3 Fracture Model – Plating Technique on Solidworks Interface*

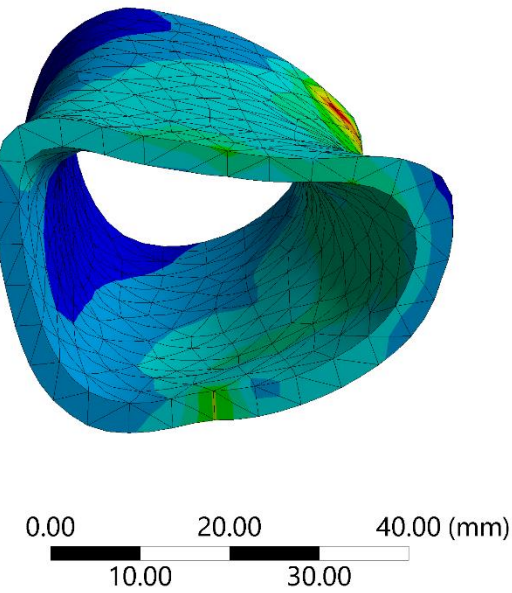
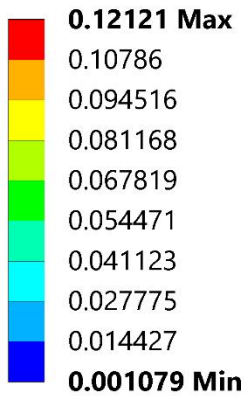
**AB: C3 Plate Voronoi**

Equivalent Elastic Strain 2  
Type: Equivalent Elastic Strain  
Unit: mm/mm  
Time: 1 s  
04/07/2023 16:45



**AB: C3 Plate Voronoi**

Equivalent Elastic Strain 2  
Type: Equivalent Elastic Strain  
Unit: mm/mm  
Time: 1 s  
04/07/2023 16:45





Upon examining the figures presented above, it is reasonable to conclude that the presence of a C3 fracture in our model does not significantly alter our results. The strain distributions observed in the interface between the scaffold and the bone remain largely consistent with those obtained in the absence of the C3 fracture. This suggests that the fracture does not critically impact the performance of our scaffold design in promoting bone regeneration.

Therefore, it appears unnecessary to delve further into this specific scenario. We can confidently assert that our porous scaffold design is robust and adaptable, capable of accommodating complex clinical scenarios such as the co-existence of a distal femur bone defect and a C3 fracture. This finding enhances the potential applicability of our design in the treatment of a wide range of bone defects.

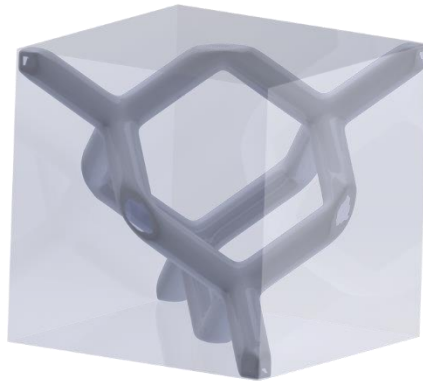
### 5.5 Post-Regeneration Simulations

In the following chapter of this thesis, we will delve into an analysis of the fully regenerated bone, after it has matured and filled the pores of the scaffold. This stage of the analysis is crucial as it provides insights into the post-healing condition of the bone, and whether the patient's bone structure has been fully restored to its original state.

Understanding the post-healing condition of the bone is critical for several reasons. Firstly, it allows us to evaluate the effectiveness of the scaffold in facilitating bone regeneration. Secondly, it provides insights into the mechanical properties of the regenerated bone, such as its strength and durability, which are key indicators of the success of the treatment. Lastly, it helps us understand whether the patient can regain normal function and mobility, and whether any further treatments or interventions are required.

By simulating this stage, we can gain a comprehensive understanding of the entire healing process, from the initial treatment to the final outcome. This will not only help in assessing the effectiveness of our current scaffold design but also provide valuable insights for future improvements and innovations in the field of bone regeneration.

To investigate this, we will utilize the homogenization method previously discussed. Specifically, we will create a block in which the negative space of the unit cell box will possess the properties of healthy cortical bone. This approach allows us to simulate the portion of the porous scaffold that has been filled with regenerated healthy bone within ANSYS Software. By doing so, we can effectively mimic the conditions of a fully healed bone, providing us with valuable insights into the mechanical properties and overall robustness of the regenerated bone structure.



*Figure 5.41 Regenerated Diamond Unit Cell*

The figure below illustrates the setup for our homogenization process. The transparent box containing the diamond unit cell is filled with healthy bone material, representing the regenerated bone within the scaffold's pores. This setup is now prepared for the homogenization process, which will yield the material properties of the regenerated bone structure. These properties will then be used in subsequent simulations to assess the mechanical performance of the fully healed bone.

To evaluate the robustness of the fully healed bone, we will compare it with a healthy, unfractured bone. This comparison will involve simulating the load from a gait cycle on both a healthy bone and the healed bone. The key parameters we will examine are the total deformation of the bone, which we discussed in a previous chapter as an indicator of bone robustness, and the strains developed in the same section of both the healthy and healed bones. This comparison will provide valuable insights into the mechanical performance of the healed bone and its ability to withstand physiological loads.

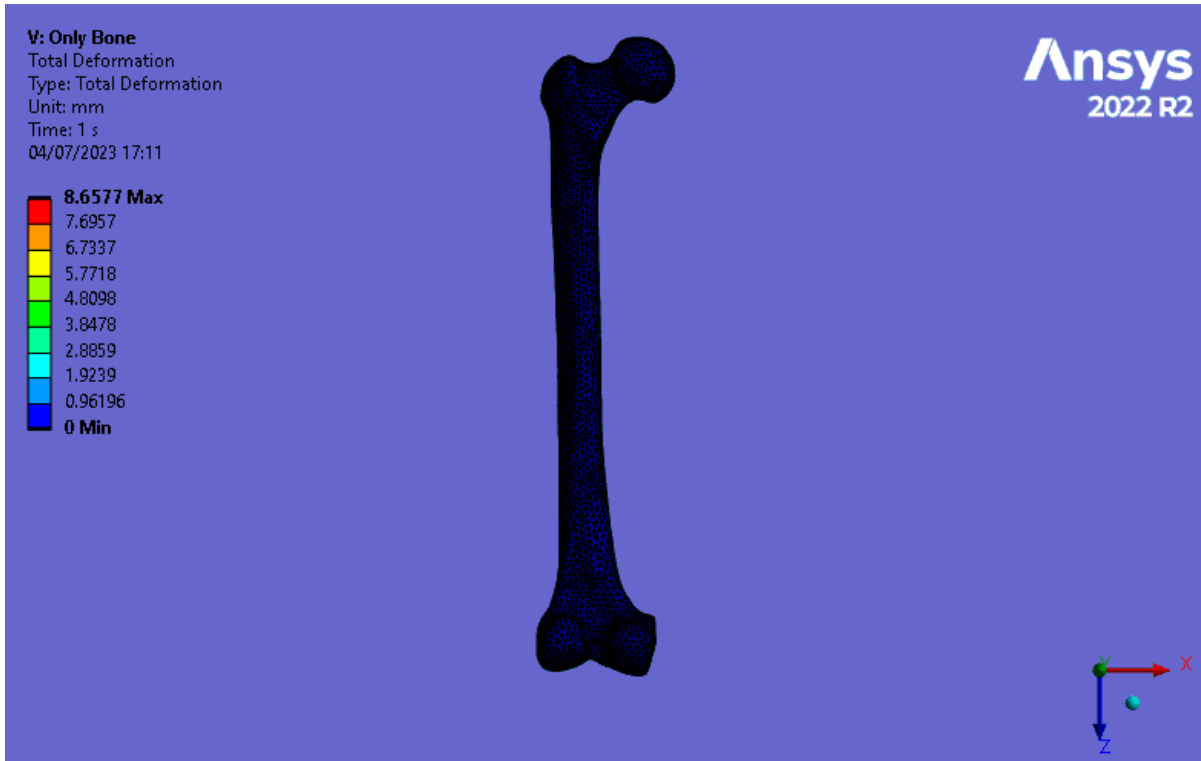


Figure 5.42 Deformation of Healthy Bone

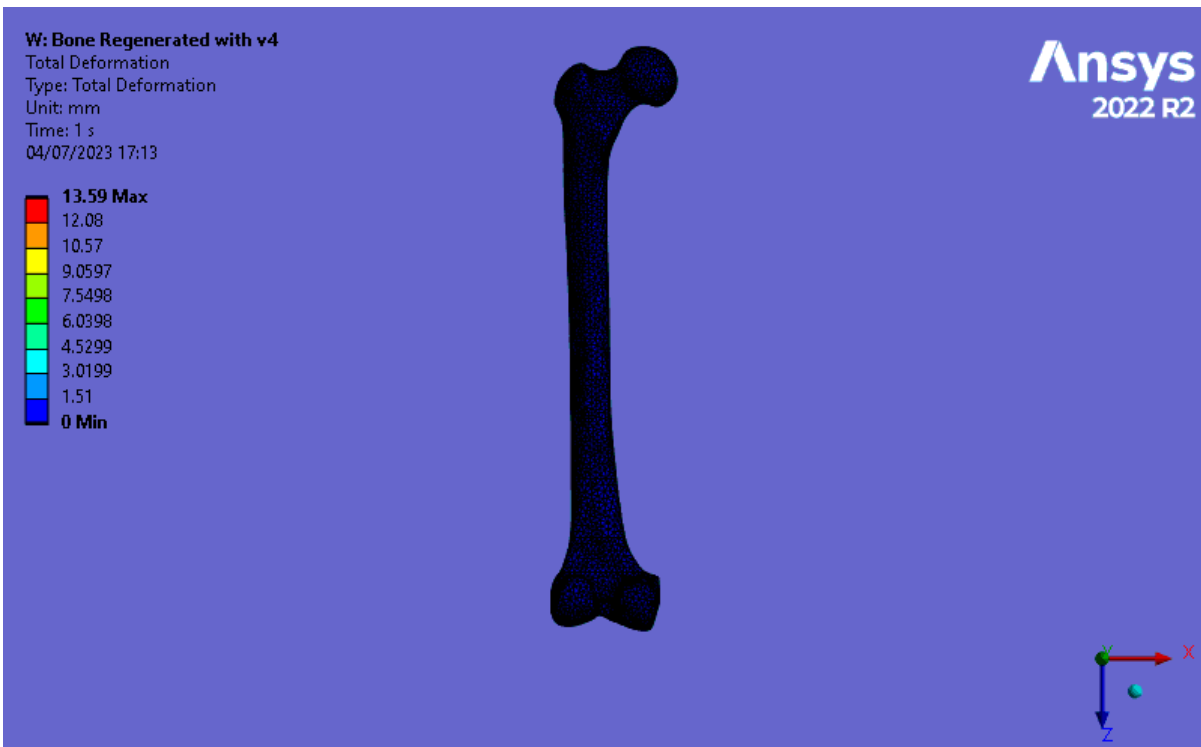


Figure 5.43 Deformation of Healed Bone with Diamond Scaffold

**V: Only Bone**

Equivalent Elastic Strain 2  
Type: Equivalent Elastic Strain  
Unit: mm/mm  
Time: 1 s  
04/07/2023 17:15

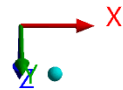
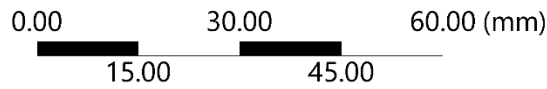
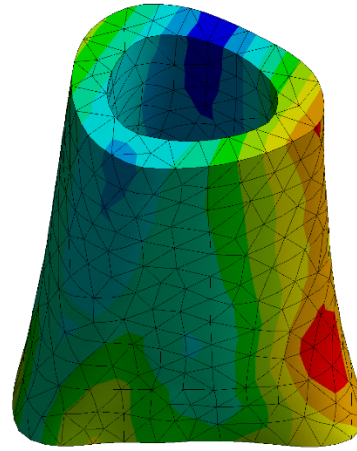
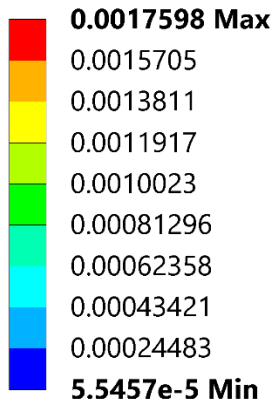


Figure 5.44 Strains Developed on Healthy Bone

**W: Bone Regenerated with v4**

Equivalent Elastic Strain 2  
Type: Equivalent Elastic Strain  
Unit: mm/mm  
Time: 1 s  
04/07/2023 17:15

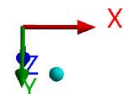
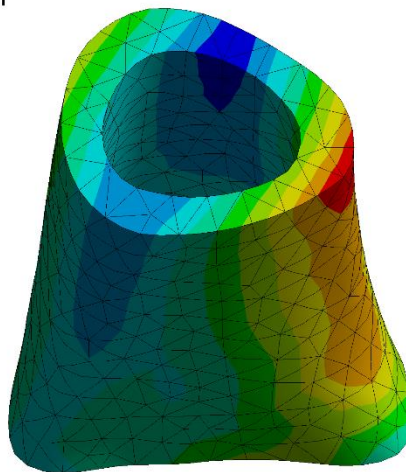
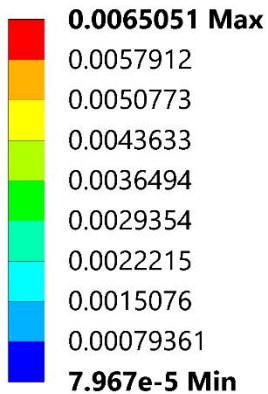


Figure 5.45 Strains Developed on Healed Bone with Diamond Scaffold

Upon reviewing the results, it is clear that while the deformation and strains developed in the healed bone may not perfectly match those of the healthy bone, the healed bone can still be considered fully functional and operational. It is important to note that a bone that has experienced a fracture may never fully return to its pre-fracture state. However, the goal of treatment and rehabilitation is to restore as much function as possible, and the results of our simulations suggest that this goal can be achieved with the use of the designed porous scaffold.

## 5.6 Conclusions and Final Scaffold Design Selection

To conclude this chapter, we will now compile all the data regarding the strains developed at the interface of the porous scaffold (5.3) into a comprehensive table. This will allow us to assess each design solution in a clear and concise manner. By comparing the strain values and other critical parameters across different designs, we can make an informed decision about the optimal design for the porous scaffold. This table will serve as a valuable reference point for our final conclusions and recommendations.

Table 18 Table of Strains Developed

Fixation Technique	Unit Cell Parameters			Average Strains Developed	
	Geometry	Thickness (mm)	Point Spacing (mm)	Upper Side	Lower Side
Plating	Honeycomb	0.25	-	0.27%	0.30%
	Diamond	0.35	-	1.05%	1.20%
		0.25	-	4.50%	5.50%
	Voronoi	0.2	1	1.30%	1.40%
0.15		1.2	3.70%	5.80%	
Nailing	Diamond	0.35	-	3.10%	2.10%
		0.25	-	x	x
	Voronoi	0.2	1	2.10%	1.30%
		0.15	1.2	x	x
Plate and Nail	Diamond	0.35	-	1.00%	1.50%
		0.25	-	2.30%	2.60%
	Voronoi	0.2	1	1.30%	1.70%
		0.15	1.2	3.20%	4.40%

The strain development observed in our simulations is influenced not only by the design of the scaffold but also by the method of fixation. As we have previously noted, the honeycomb structure was excluded from further simulations due to the very low strains it produced and given the inherent limitations of the honeycomb structure in facilitating multi-directional bone regeneration.

A notable observation from our simulations is the inability of the retrograde nailing technique to converge to a result when used with the thinner diamond and Voronoi structures. This suggests that these two scaffolds designs may not be suitable for a single nailing approach.

This is indicated in the table above, where these combinations are highlighted in red. Furthermore, it is noteworthy that the nailing technique tends to produce larger strains on the lower side of the scaffold compared to the upper side.

In our pursuit of the optimal scaffold design, we find the thinner Voronoi and diamond options to be promising when used in conjunction with the plating or the combined plating and nailing technique. However, for the single nailing technique, the thicker scaffold designs appear to be more suitable.

Taking into account the literature on the Voronoi structure and its resemblance to the actual bone structure, we lean towards preferring the Voronoi scaffold over the diamond one. However, the choice of scaffold design should always be guided by the specific requirements of the case at hand.

In conclusion, the table below presents the best solutions for each case, based on our simulations and analysis. These recommendations represent our best understanding of the optimal scaffold design and fixation method for promoting successful bone regeneration in the context of a bone defect.

Table 19 Optimal Scaffold Choice for Every Fixating Technique

	Optimal Scaffold		
Fixation Technique	Geometry	Thickness (mm)	Point Spacing (mm)
Plating	Voronoi	0.15	1.2
Nailing	Diamond	0.35	-
Plate and Nail	Voronoi	0.15	1.2

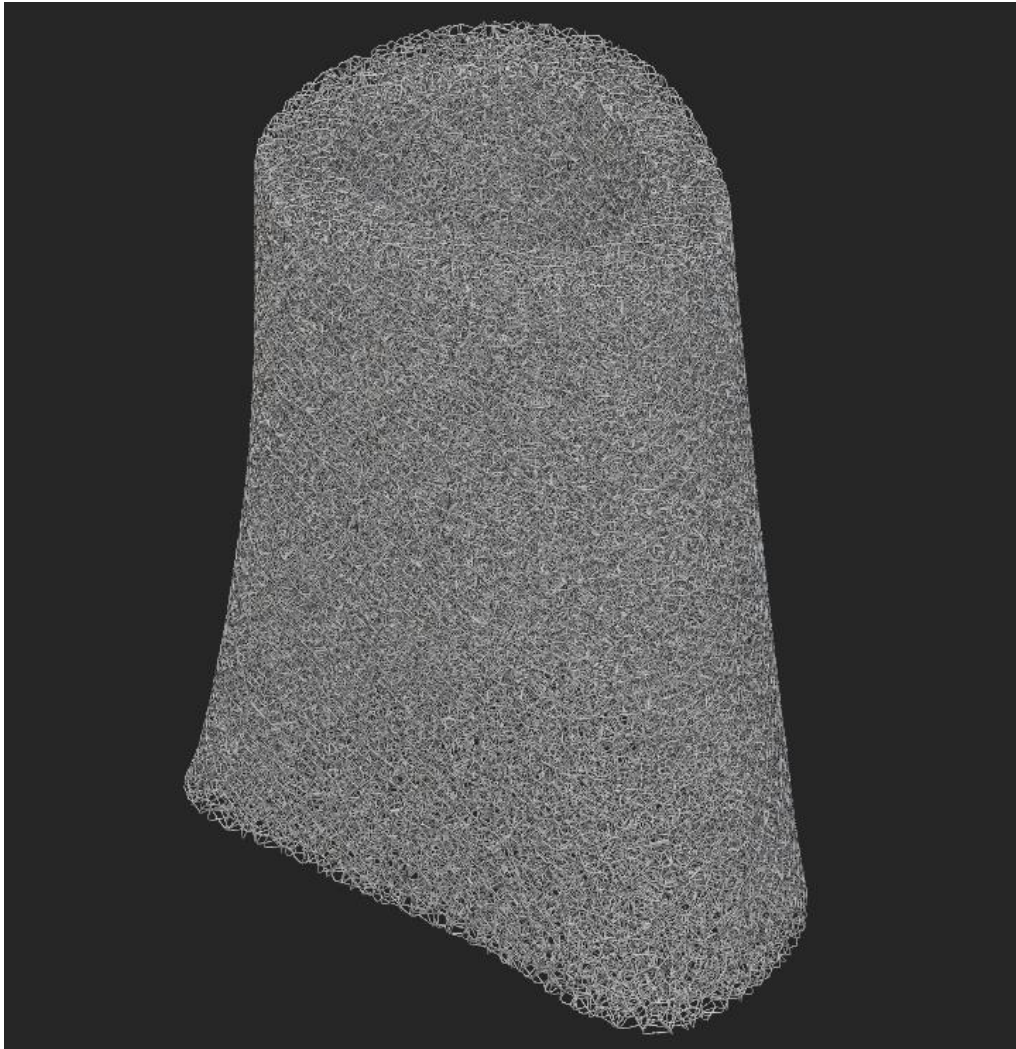


Figure 5.46 Voronoi Ideal Scaffold on nTop

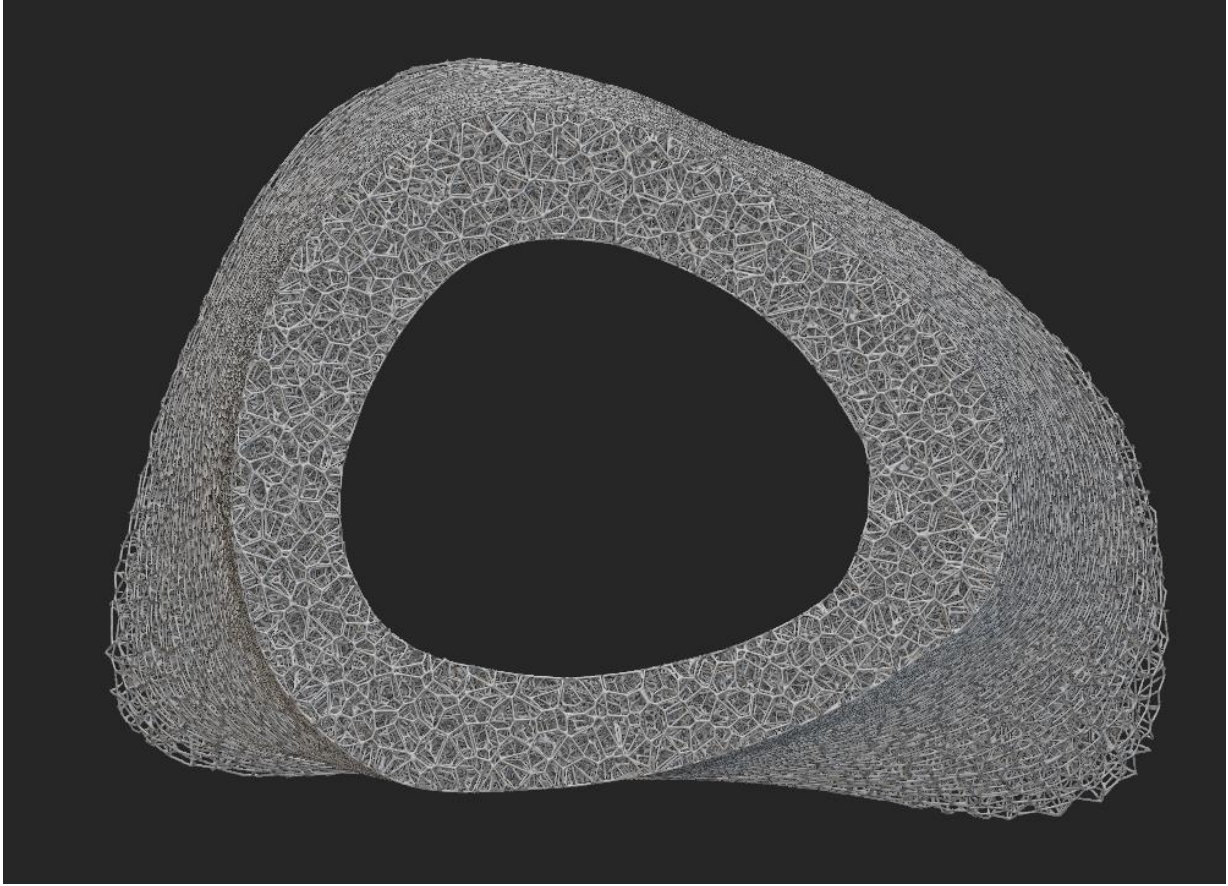


Figure 5.47 Voronoi Ideal Scaffold - Upper Side

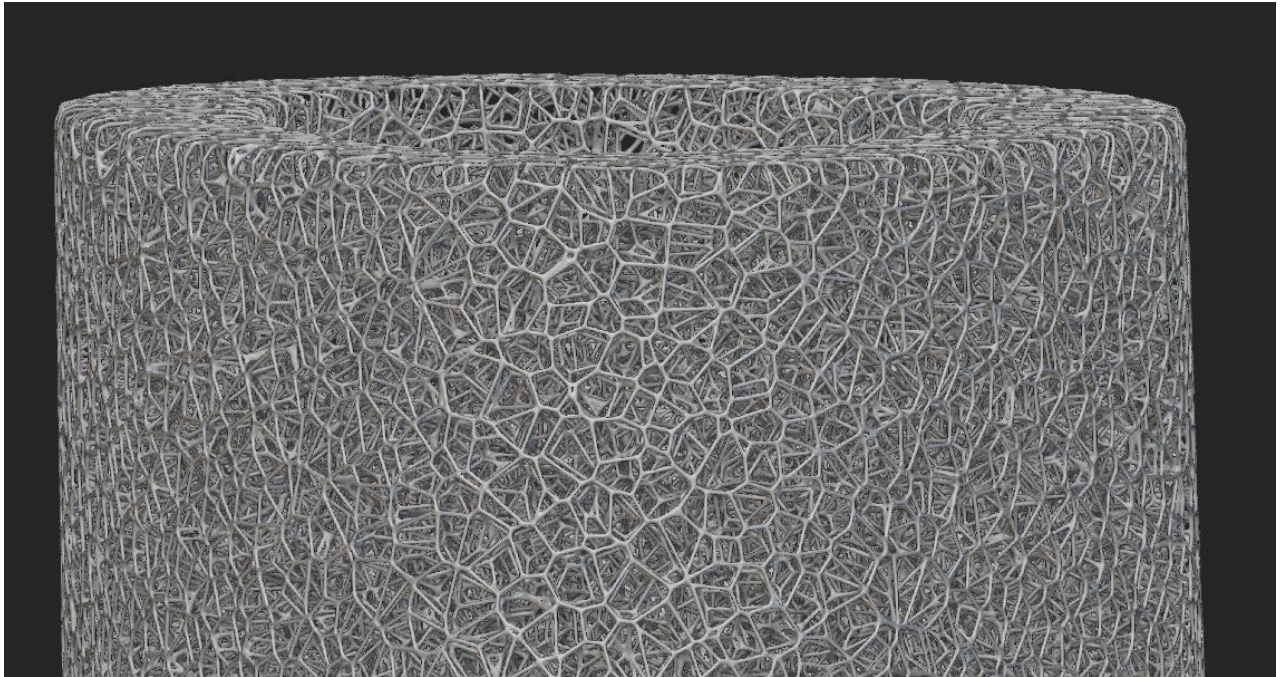


Figure 5.48 Voronoi Ideal Scaffold - Zoomed



It is important to note that the optimal scaffold designs presented in this thesis emerged from a limited pool of potential designs. Undoubtedly, there are other unit cell combinations that could yield superior results. The field of scaffold design is vast and complex, and the possibilities for innovative and effective designs are virtually limitless.

Topology optimization methods, which we will briefly explore in the next chapter, hold significant potential for advancing the design of scaffolds. These methods can optimize the design of the scaffold, tailoring it to the specific needs of each case and each patient. This personalized approach could significantly enhance the effectiveness of the scaffold and ultimately improve patient outcomes.

In the context of this thesis, the presented scaffold designs represent our best understanding and application of the current knowledge and technology. However, the field is constantly evolving, and future research and technological advancements will undoubtedly lead to the development of even more effective and efficient scaffold designs.

## 6. Exploring Topology Optimization

Topology optimization (TO) is a mathematical approach that optimizes the layout of material within a given design space, for a set of loads, boundary conditions, and constraints, with the aim of maximizing the system's performance. Unlike shape optimization and sizing optimization, topology optimization allows the design to take any shape within the design space, rather than dealing with predefined configurations.

The conventional topology optimization formulation uses a finite element method (FEM) to evaluate the design performance. The design is optimized using either gradient-based mathematical programming techniques or non-gradient-based algorithms such as genetic algorithms. Topology optimization has a wide range of applications in aerospace, mechanical, bio-chemical, and civil engineering. Currently, engineers mostly use topology optimization at the concept level of a design process [31].

In the context of scaffold design, topology optimization can be a powerful tool. It can help in creating scaffolds that are not only structurally sound but also mimic the complex structures found in natural tissues. This can lead to better integration with the host tissue and improved healing outcomes. However, the results from topology optimization are often difficult to manufacture due to their complex shapes. This is where additive manufacturing or 3D printing comes into play. With the ability to create complex shapes, 3D printing can be used to manufacture the optimized scaffold designs directly.

Despite its potential, the use of topology optimization in scaffold design is still an active field of research. Adding constraints to the formulation to increase the manufacturability and personalizing the design for each patient's needs are some of the challenges that need to be addressed. Nevertheless, with the advancements in computational power and 3D printing technology, topology optimization holds great promise in the field of scaffold design and tissue engineering.

In conclusion, topology optimization is a powerful tool that can aid in the design of more effective and efficient scaffolds for tissue engineering applications. By allowing for the creation of complex structures that mimic natural tissues, it can lead to improved healing outcomes. However, the use of this technique in scaffold design is still an active area of research, with many challenges to overcome.

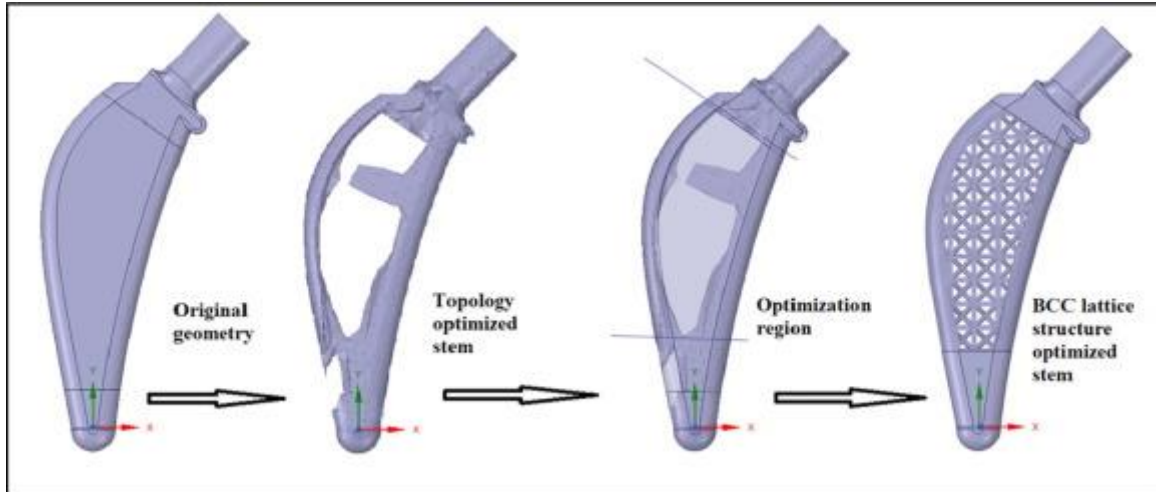


Figure 6.1 Topology Optimization of Hip Implant [32]

## 6.1 Scaffold Design Optimization

In this chapter, we delve into the application of topology optimization for scaffold design using nTop software. Specifically, we utilize the Field Optimization Block and Parametric Component Blocks, both of which are currently in BETA mode and represent recent additions to the software. It's important to note that these tools are in their early stages of development, implying that there is substantial potential for future enhancements and refinement of their functionality. Nevertheless, for the preliminary stage of our investigation, these tools provide an acceptable platform for exploring the potential of topology optimization in scaffold design.

Our primary objective in this chapter is to generate an optimal design that, under the forces exerted by the gait load on the scaffold implant, will produce the precise strain levels necessary for bone regeneration. In our case, this target strain is 5%. To set up this optimization simulation, it is necessary to determine the forces applied to the scaffold. To achieve this, we revert to ANSYS Software, where we execute the simulation and calculate the force and moment reactions exerted on the scaffold.

In pursuit of this goal, we make certain assumptions that may lead to minor inaccuracies, but these are deemed acceptable at this stage of the research. In the ANSYS simulation, we suppress the lower part of the healthy bone and fix the lower part of the scaffold. Additionally, we define the material of the scaffold as a solid part composed of Ti6Al4V, without any pores. This leads to force results that differ from the expected ones. If the focus of this thesis was solely on this task, an iterative process of modifying the scaffold and generating a new scaffold to be reinserted into the primary stage would be the ideal approach.

**J: Forces for nTop**

Fixed Support

Time: 1. s

04/07/2023 19:19

■ Fixed Support

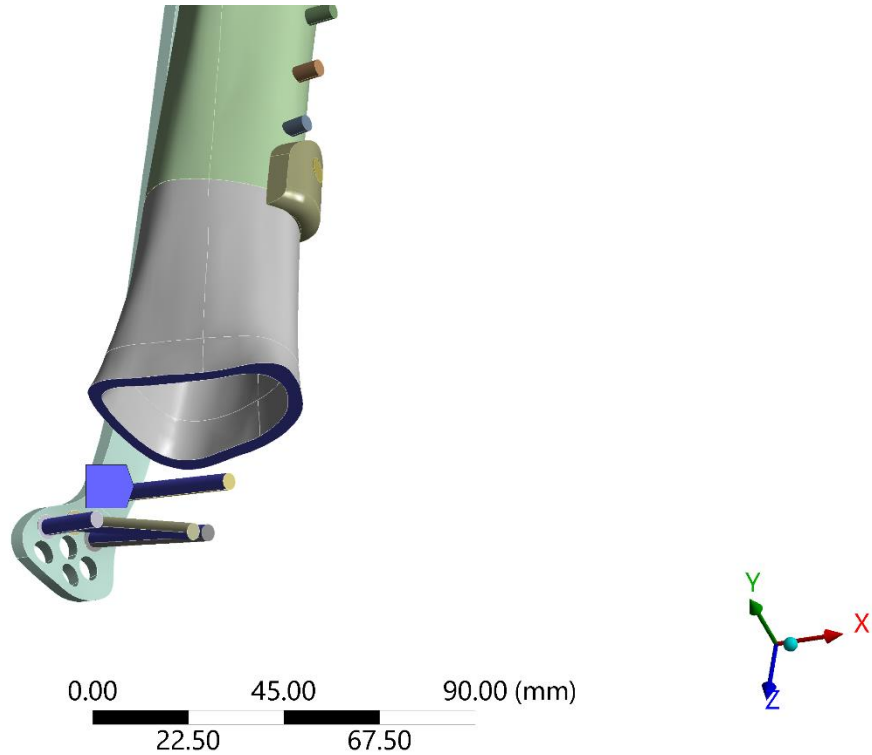


Figure 6.2 Forces Extraction Approach on Ansys

In nTop software, the first step is to define the overall geometry of the scaffold and convert it into a Finite Element Model. This is accomplished using a series of blocks, specifically: Mesh from CAD Body, Remesh Surface, and FE Volume Mesh. These blocks allow us to create a detailed model of the scaffold, which can then be converted into a Finite Element Model.

Following this, we need to establish the boundary conditions. This involves specifying the forces applied to the scaffold and its supports. We import the fixed support, along with all the forces and moments applied to the scaffold.

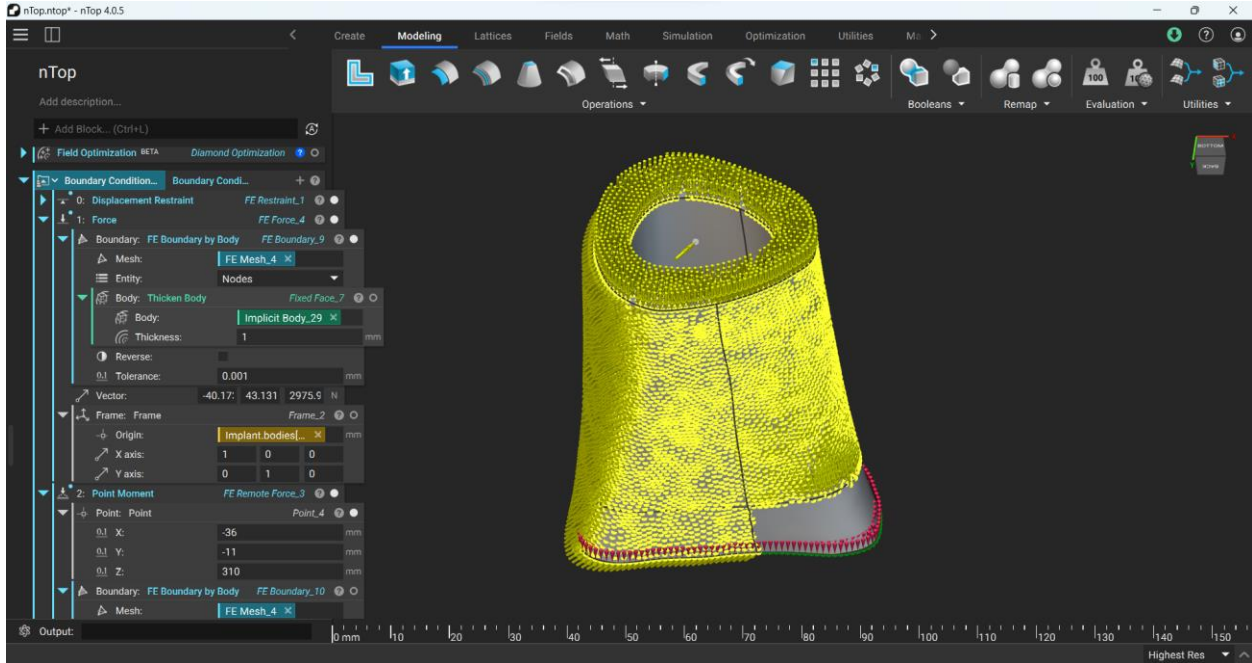


Figure 6.3 nTop: Setting Boundary Conditions

Upon establishing the boundary conditions, we can proceed to examine the deformation and strain of the solid scaffold. This step is crucial as it allows us to validate the model by comparing the results with those obtained from ANSYS Software. By doing so, we can ensure the accuracy and reliability of our model, which is paramount in the subsequent stages of scaffold design and optimization. This comparison serves as a check to confirm that our model is behaving as expected under the given conditions, and that it accurately represents the physical scenario we are trying to simulate.

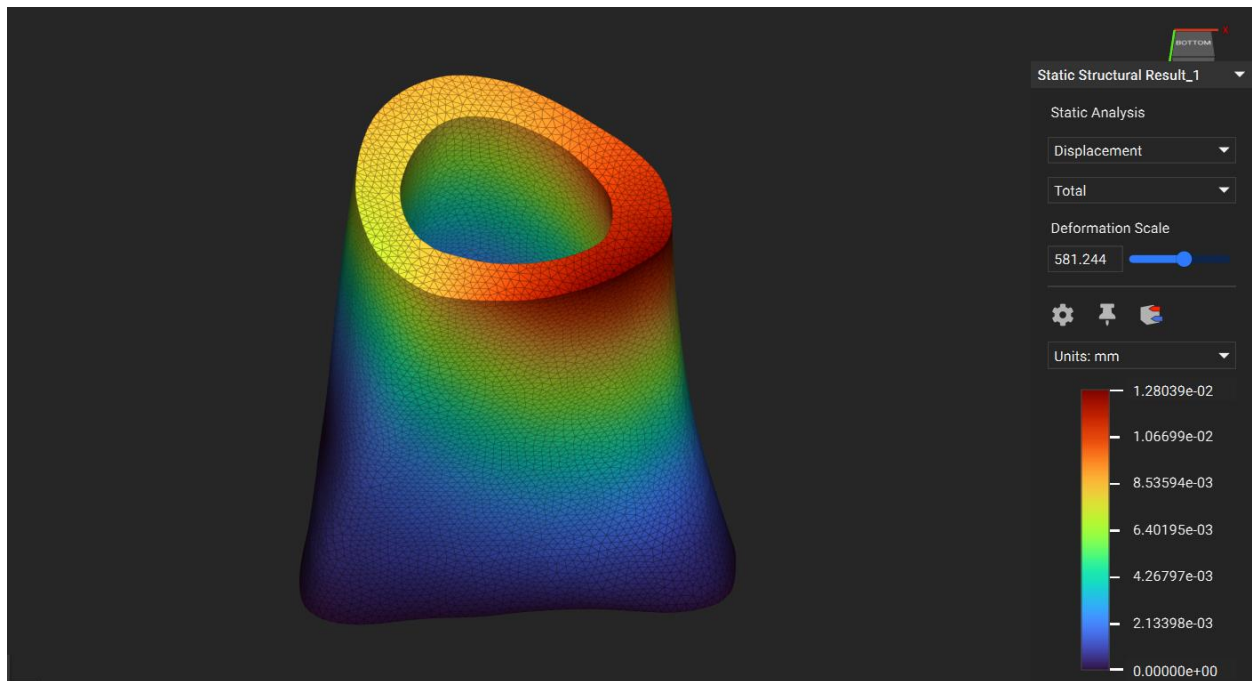


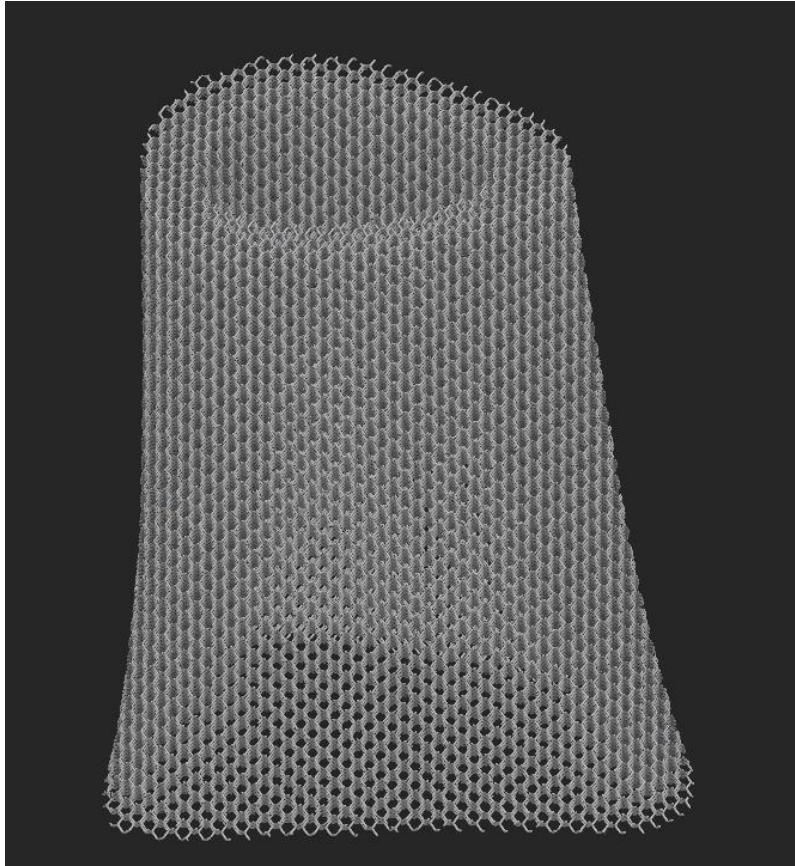
Figure 6.4 Scaffold Displacement

With the boundary conditions set, we are now ready to insert the parametric model. This model will allow us to adjust various parameters of the scaffold design, enabling us to optimize its performance under the specified loads and constraints. This process is crucial in ensuring that the scaffold design is not only feasible, but also effective in promoting bone regeneration.

In the parametric model, we incorporate two distinct types of scaffolds: a diamond and a Voronoi structure. The specific parameters for each of these scaffold types are detailed in the table below. This inclusion of different scaffold types allows us to compare and contrast their performance under the same conditions, thereby providing a comprehensive understanding of their suitability for the task at hand.

Table 20 Parametric Components Parameters

		Parametric Components	
		Diamond	Voronoi
Cell Size	Minimum	-	0.8
	Maximum	-	5
	Initial	2	2
Thickness	Minimum	0.1	0.08
	Maximum	0.6	0.6
	Initial	0.25	0.4



*Figure 6.5 Diamond Initial Component*



*Figure 6.6 Voronoi Initial Component*

Before initiating the optimization process, it is crucial to establish the objective and constraints of the problem. Given the current limitations of the Field Optimization block, which is still in its Beta stage, we are unable to define our own objective function. However, we have devised a workaround for this issue. We set the objective to maximize stress, with the constraint that the stress value does not exceed the level corresponding to a 5% strain. This value is calculated by multiplying the material's Young's modulus by 5%. With these parameters in place, we are ready to commence the optimization process.

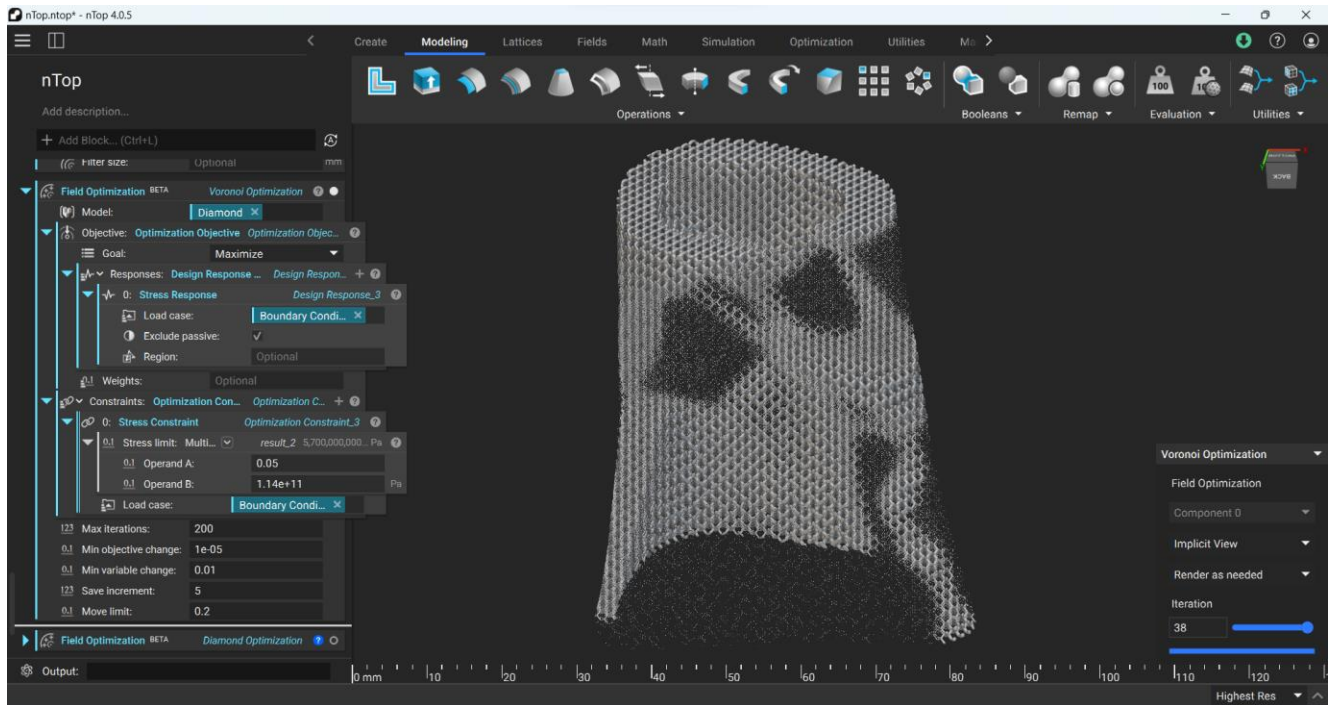


Figure 6.7 nTop Interface: Optimal Voronoi Scaffold Result



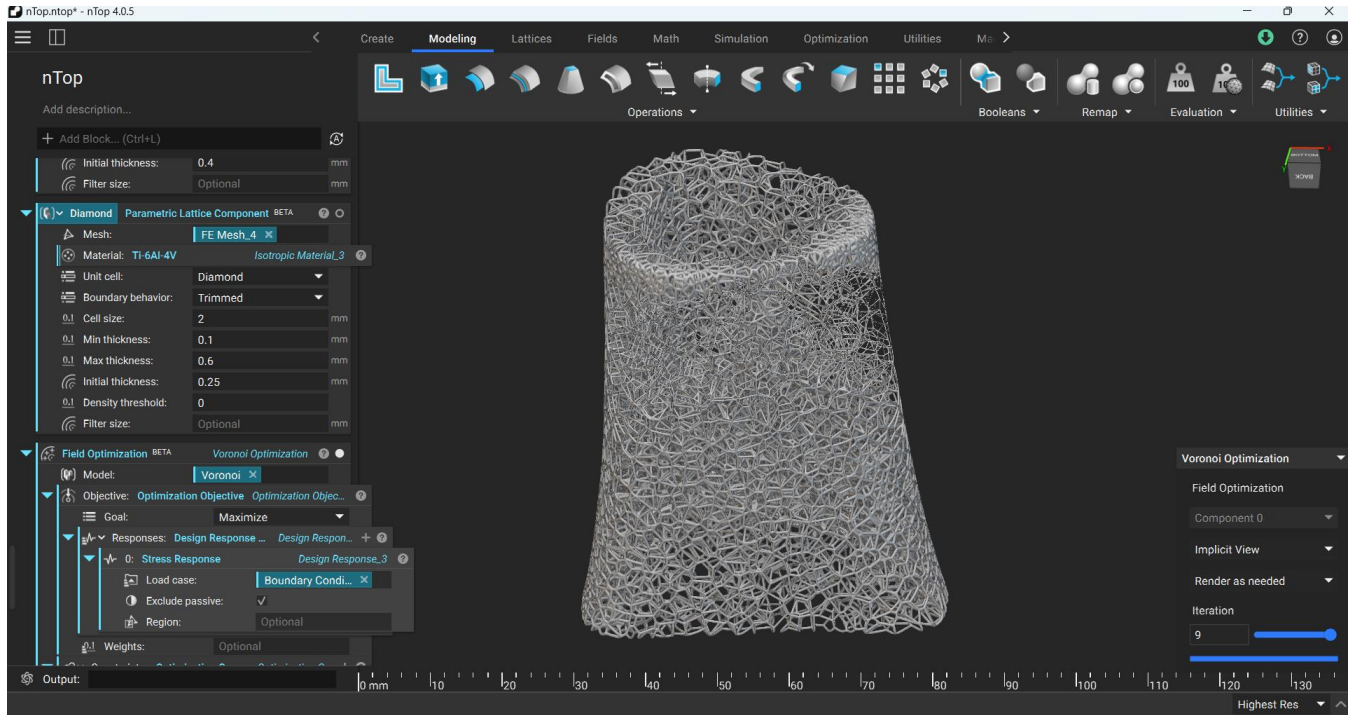
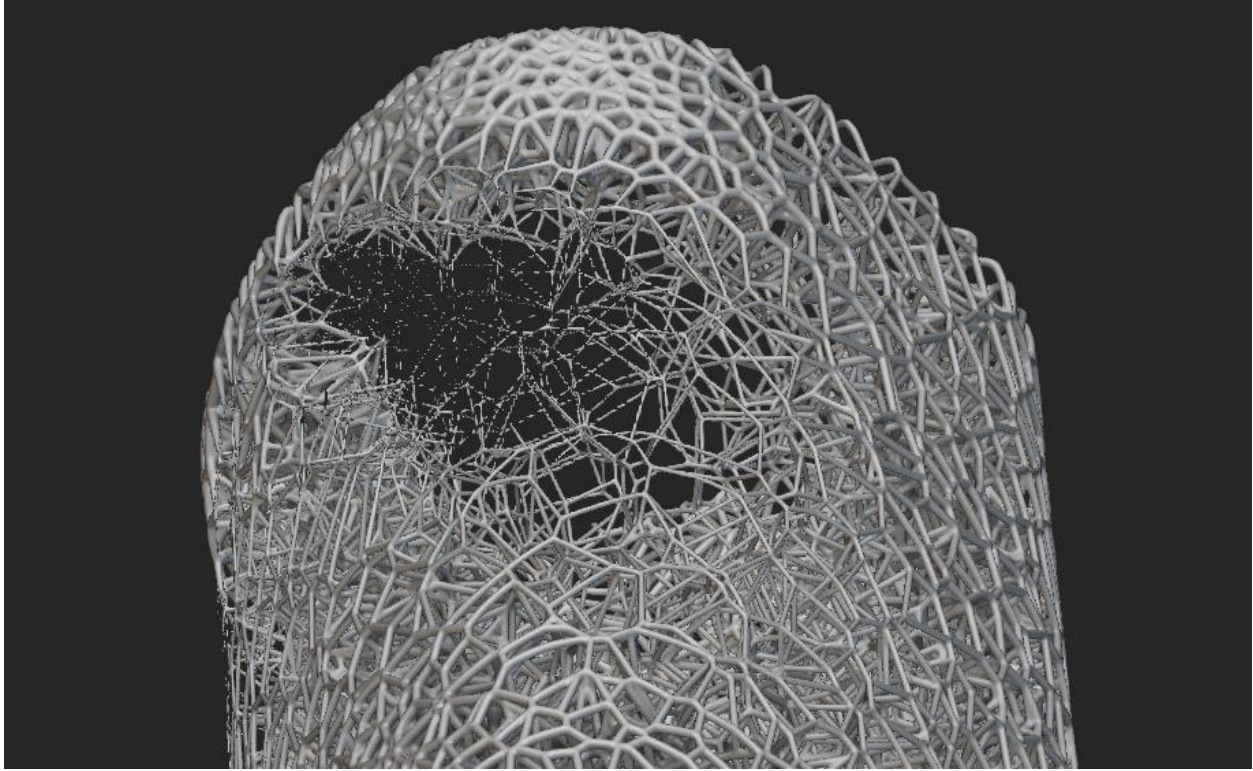


Figure 6.8 nTop Interface: Optimal Voronoi Scaffold Result

Upon reviewing the results, several observations can be made. Firstly, as indicated in Table 20, it becomes apparent that it is not feasible to create a diamond scaffold with varying cell sizes. This limitation renders the process ineffective and futile for the diamond scaffold. Consequently, the parametric Voronoi scaffold emerges as a more viable and essential approach for optimization.



*Figure 6.9 nTop Optimization Imperfections*

However, it is important to note that the optimal Voronoi scaffold generated also presents its own set of challenges and imperfections. These are largely attributable to the beta stage of the software used, which inherently limits the possibilities for optimization, such as the inability to further examine the extracted design. Despite these constraints, the process provides valuable insights and serves as a stepping stone for further development and refinement of the optimization process.

## 7. Conclusion

This chapter concludes this study by summarizing the key findings in relation to the research objectives and discussing their relevance in the context of existing literature. The limitations of the study are acknowledged, providing a clear understanding of the scope of the research. Suggestions for improvements and future research directions are also presented, offering a roadmap for further exploration in this field.

This study was primarily focused on identifying the most effective fixation method and optimal scaffold design to ensure patient mobility and promote bone regeneration. Through a series of simulations and analyses, we sought to understand the interplay between various fixation techniques and scaffold structures, and their impact on bone regeneration. The ultimate goal was to provide a robust solution that not only supports the healing process but also maintains the patient's mobility, thereby improving their overall quality of life.

The journey began with an in-depth literature review that provided a solid foundation for understanding the complexity of bone defects, the healing process of bone fractures, and the conventional methods of treating distal femur fractures. The review also shed light on the emerging field of 3D printed bone implants, the role of metallic porous scaffolds in bone repair, and the optimal mechanical environment for osteogenesis in bone loss defects.

The subsequent chapters delved into the practical aspects of bone defect repair, starting with the transformation of CT scans into CAD models of bones. This was followed by the designing of distal femur plates, retrograde intramedullary nailing system and porous scaffold, as CAD models. The gait analysis provided crucial insights into the forces and supports that would be applied in real-life scenarios, informing the boundary conditions for the finite element analysis.

In the context of non-scaffold approaches, our findings revealed that single plating or single nailing techniques were not viable without a scaffold implant. These methods did not provide the necessary conditions for optimal bone regeneration, or didn't ensure the bone stability at all. On the other hand, the double plating fixation approach emerged as a highly recommended strategy. This method demonstrated a significant potential to ensure the natural mobility of the patient, which is a crucial factor in the healing process and overall patient recovery.

In terms of scaffold design, our research identified the Voronoi scaffold design as the most effective approach. A significant advantage of the Voronoi scaffold lies in its structural resemblance to the natural bone structure. This similarity not only enhances the scaffold's compatibility with the bone but also promotes a more natural and effective healing process. The structural mimicry of the Voronoi scaffold to the bone's architecture makes it a promising solution for bone defect treatment. Concerning the optimal structure, a balance had to be maintained between ensuring the necessary stability and achieving the required compliance to develop the desired strain.

This study, while comprehensive, is not without its limitations. Given the scope of a thesis report, it was not possible to evaluate and examine all potential cases in depth. The solutions proposed herein are indicative and serve as a starting point, with the understanding that more precise and effective solutions could be designed with further research. Additionally, due to constraints in time and computational

resources, larger mesh sizes were used in some simulations. While this approach was necessary for practical reasons, it may have introduced some degree of inaccuracy in the final results. These limitations highlight areas for improvement and suggest directions for future research in this field.

In the final stages of this thesis, we ventured into the domain of topology optimization. While this aspect was not the primary focus of our research, it provided valuable insights and highlighted the immense potential of this tool for future studies. Topology optimization opens up a world of possibilities for designing the optimal scaffold implant, tailored to the specific needs of each patient, and promoting rapid and effective bone regeneration. Although our exploration of this area was somewhat limited in depth due to the broader focus of the thesis, it underscored the significant opportunities for further development and research in this field.

In conclusion, this thesis has provided a comprehensive exploration of bone defect repair, from the initial understanding of bone defects and their healing process to the practical application of CAD design, finite element analysis, and topology optimization. The findings from this research contribute to the ongoing efforts to improve bone defect management and offer promising avenues for future research.

## List of References

- [1] Ibrahim, A. M., & Siddique, M. S. (2018). Subacute bacterial endocarditis prophylaxis.
- [2] Wallace, H. A., Basehore, B. M., & Zito, P. M. (2017). Wound healing phases.
- [3] Li, Z., Wang, Q., & Liu, G. (2022). A review of 3D printed bone implants. *Micromachines*, 13(4), 528.
- [4] Reno Orthopaedic Clinic. Distal Femur Fracture. Retrieved June 21, 2023, from <https://www.renoortho.com/specialties/center-for-fracture-trauma/distal-femur-fracture/#:~:text=The%20distal%20femur%20can%20be%20fixed%20with%20metal%20plates%20and,takes%201%20to%202%20hours.>
- [5] Paley Institute. Bone Defects. Retrieved June 21, 2023, from <https://paleyinstitute.org/blog/conditions/bone-defects/#/>
- [6] Mukhi, S.R., Mukhi, P., Mukhi, L.S., & Mukhi, K. (2017). A Novel Method to Fix Type C3 Distal Femur Fractures with Bone Defect Loss Using “Harms Cage”.
- [7] Chang, M. W., Liu, H. T., Huang, C. Y., Chien, P. C., Hsieh, H. Y., & Hsieh, C. H. (2018). Location of femoral fractures in patients with different weight classes in fall and motorcycle accidents: a retrospective cross-sectional analysis. *International journal of environmental research and public health*, 15(6), 1082.
- [8] Obakponovwe, O., Kallala, R., Stavrou, P. Z., Harwood, P., & Giannoudis, P. (2012). (iv) The management of distal femoral fractures: a literature review. *Orthopaedics and Trauma*, 26(3), 176-183.
- [9] TOBIG. Fracture Healing. Retrieved June 21, 2023, from <https://www.tobig.eu/bone-101/fracture-healing/>
- [10] AO Foundation. ORIF - Compression or bridging plate for Extraarticular fracture wedge. Retrieved June 21, 2023, from <https://surgeryreference.aofoundation.org/orthopedic-trauma/adult-trauma/distal-femur/extraarticular-fracture-wedge/orif-compression-or-bridging-plate#fixation-of-plate-to-proximal-fragment>
- [11] Stryker. Home. Retrieved June 21, 2023, from <https://www.stryker.com/us/en/index.html>
- [12] Fontenot, P. B., Diaz, M., Stoops, K., Barrick, B., Santoni, B., & Mir, H. (2019). Supplementation of lateral locked plating for distal femur fractures: a biomechanical study. *Journal of Orthopaedic Trauma*, 33(12), 642-648.
- [13] Garala, K., Ramoutar, D., Li, J., Syed, F., Arastu, M., Ward, J., & Patil, S. (2022). Distal femoral fractures: A comparison between single lateral plate fixation and a combined femoral nail and plate fixation. *Injury*, 53(2), 634-639.
- [14] Steinberg, E. L., Elis, J., Steinberg, Y., Salai, M., & Ben-Tov, T. (2017). A double-plating approach to distal femur fracture: a clinical study. *Injury*, 48(10), 2260-2265.
- [15] Lv, Y., Wang, B., Liu, G., Tang, Y., Lu, E., Xie, K., ... & Wang, L. (2021). Metal material, properties and design methods of porous biomedical scaffolds for additive manufacturing: A review. *Frontiers in Bioengineering and Biotechnology*, 9, 641130.

- [16] Chen, H., Han, Q., Wang, C., Liu, Y., Chen, B., & Wang, J. (2020). Porous scaffold design for additive manufacturing in orthopedics: a review. *Frontiers in Bioengineering and Biotechnology*, 8, 609.
- [17] Feng, J., Fu, J., Lin, Z., Shang, C., & Li, B. (2018). A review of the design methods of complex topology structures for 3D printing. *Visual Computing for Industry, Biomedicine, and Art*, 1(1), 1-16.
- [18] Baumer, V., Gunn, E., Riegle, V., Bailey, C., Shonkwiler, C., & Prawel, D. (2023). Robocasting of Ceramic Fischer–Koch Scaffolds for Bone Tissue Engineering. *Journal of Functional Biomaterials*, 14(5), 251.
- [19] Perren, S. M., Fernandez, A., & Regazzoni, P. (2015). Understanding fracture healing biomechanics based on the “strain” concept and its clinical applications. *Acta Chir Orthop Traumatol Cech*, 82(4), 253-260.
- [20] Gitajn, I. L., & Rodriguez, E. K. (2011). Biomechanics of musculoskeletal injury. In *Biomechanics in Applications*. IntechOpen.
- [21] Björnsdóttir, M. (2014). Influence of Muscle Forces on Stresses in the Human Femur.
- [22] Simoes, J. A., Vaz, M. A., Blatcher, S., & Taylor, M. (2000). Influence of head constraint and muscle forces on the strain distribution within the intact femur. *Medical engineering & physics*, 22(7), 453-459.
- [23] TeachMeAnatomy. Anatomical Terminology: Planes. Retrieved July 1, 2023, from <https://teachmeanatomy.info/the-basics/anatomical-terminology/planes/>
- [24] Ghiasi, M. S., Chen, J. E., Rodriguez, E. K., Vaziri, A., & Nazarian, A. (2019). Computational modeling of human bone fracture healing affected by different conditions of initial healing stage. *BMC musculoskeletal disorders*, 20(1), 1-14.
- [25] Luthringer, B. J. C., Ali, F., Akaichi, H., Feyerabend, F., Ebel, T., & Willumeit, R. (2013). Production, characterisation, and cytocompatibility of porous titanium-based particulate scaffolds. *Journal of Materials Science: Materials in Medicine*, 24, 2337-2358.
- [26] Zhang, G., Zhao, P., Lin, L., Qin, L., Huan, Z., Leeflang, S., ... & Wu, L. (2021). Surface-treated 3D printed Ti-6Al-4V scaffolds with enhanced bone regeneration performance: An in vivo study. *Annals of Translational Medicine*, 9(1).
- [27] Özgün. (2021). Ansys Contact Types and Explanations. Mechead.com. Available at: <https://www.mechead.com/contact-types-and-behaviours-in-ansys/> [Accessed: July 2, 2023].
- [28] Rancourt, D., Shirazi-Adl, A., Drouin, G., & Paiement, G. (1990). Friction properties of the interface between porous-surfaced metals and tibial cancellous bone. *Journal of biomedical materials research*, 24(11), 1503-1519.
- [29] Shockey, J. S., Von Fraunhofer, J. A., & Seligson, D. (1985). A measurement of the coefficient of static friction of human long bones. *Surface Technology*, 25(2), 167-173.
- [30] "PADT, Inc. (2022). ANSYS Lattice Material Homogenization. Retrieved from [https://www.padtinc.com/wp-content/uploads/2022/03/PADT-ANSYS-Lattice-Material\\_Homogenization-1.pdf](https://www.padtinc.com/wp-content/uploads/2022/03/PADT-ANSYS-Lattice-Material_Homogenization-1.pdf)"

[31] "Topology optimization." Wikipedia, The Free Encyclopedia. Wikipedia, The Free Encyclopedia, 24 Apr. 2023. Web. 21 Jun. 2023.

[32] Belwanshi, M., Jayaswal, P., & Aherwar, A. (2022). A study on finite element analysis methodologies and approaches used for total hip arthroplasty. *Materials Today: Proceedings*, 56, 2596-2604.

[33] Lian, X., Zhao, K., Chen, W., Zhang, J., Li, J., Meng, H., ... & Zhang, Y. (2021). Application of a double reverse traction repositior in the retrograde intramedullary nailing of distal femur fractures. *Journal of Orthopaedic Surgery and Research*, 16, 1-9.